Application of scalable and inexpensive modification on carbon in clean technologies

by

Md Zawad Hossain

B.S., University of Dhaka, 2024

A THESIS

submitted in partial fulfillment of the requirements for the master's degree.

MASTER OF SCIENCE

Department of Chemistry
College of Arts and Sciences

KANSAS STATE UNIVERSITY
Manhattan, Kansas

2024

Approved by:

Major Professor
Professor Jun Li

Copyright

Abstract

Carbon can be a game-changing material to meet the global challenges in freshwater production and renewable conversion and storage devices due to their versatile nature. However, its hydrophobic characteristics, poor stability, low electrical conductivity, and small number of active sites limit its functions. Therefore, numerous efforts have been made to develop modified carbon materials to enhance their properties as electrocatalysts and electrode materials. This research focuses on developing modified nanocarbon materials for applications in water desalination by capacitive deionization (CDI) and electrochemical H_2O_2 synthesis via oxygen reduction reaction (ORR).

In the first application, a systematic study has been conducted for controllable and quantifiable impregnation of a cationic surfactant cetyl trimethyl ammonium bromide (CTAB) and an anionic surfactant sodium dodecyl sulfate (SDS) on activated carbon (AC) electrodes, respectively, and used to construct a asymmetric electrochemical cells. The electrochemical properties have been thoroughly characterized with cyclic voltammetry (CV) and galvanostatic charge-discharge (GCD) measurements. The electrochemical cells consisting of a pair of such electrodes are then studied for CDI by flow 1000 ppm NaCl solution between the two electrodes, i.e., in the flow-by configuration. Three different CDI modes have been investigated, including normal CDI (applying a voltage waveform with positive voltage bias at the CTAB-modified AC electrode for charge and zero voltage for discharge), inverted CDI (applying a reverse voltage waveform from the normal CDI), and bipolar CDI (applying a positive voltage bias on CTAB-modified AC electrode for a period and the reversed voltage in the following period). The electrochemical and normal CDI studies have shown that the increase of surfactant loadings reduces the electrochemical double layer capacitance and salt adsorption capacity. However, the CDI stability and charge efficiency are enhanced. The energy consumption is lower for surfactant-modified AC electrodes. The inverted CDI has demonstrated the effectiveness of surfactant modification as a charge-selective membrane. The bipolar CDI has demonstrated an enhanced salt adsorption capacity with surfactant-modified AC electrodes and the improved stability against carbon oxidation.

In the second application, a preliminary study was conducted on developing electrocatalysts for ORR via N-doped carbon. A new type of graphitic carbon with a unique structure (crumbled balls with turbostratic multi-layer graphene sheets) produced by a high-temperature gas detonation process is explored for N-doping via a post-growth thermal annealing process. From the linear sweep voltammetry in O_2-saturated 0.50 M H_2SO_4 solution

by rotating disk electrode (RDE), it has been demonstrated that, after N-doping on the carbon, the onset potential of ORR is increased by +317 mV and half-wave potential is improved by +270 mV compared to the pristine graphitic carbon. The study by rotating ring disk electrode (RRDE) further demonstrates that N-doped graphitic carbon exhibits a $2e^-$ ORR mechanism with a high H_2O_2 selectivity of ~60%. With further optimization, this could be a good candidate for selective H_2O_2 production by electrolysis

Table of Contents

List of Figures

List of Tables

Acknowledgements

First and foremost, I would like to express my sincere gratitude to my advisor and mentor, Professor Jun Li, for his continuous support and guidance, and valuable advice throughout these years. His mentorship has been instrumental in my success. I would also like to thank Marc Andelman for his guidance and insightful discussions. I am grateful to Professor Daniel Higgins and Professor Peter Sues for their time and insightful advice.

I extend a special thank you to Dr. Dan Boyle of Kansas State University and Steve Michalaski of the University of Nebraska Lincoln for their assistance with XPS analysis. I am grateful to Michael Hinton, Dr. Tingting, and Dr. Sadish for teaching me essential lab skills. I would like to extend my appreciation to Jim Hodgson, Tobe Eggers, Bart Bath, and Kimberly Ross for their help over the past years.

I am thankful to all current members of the Jun Li group, with a special mention to Sabari Rajendran for his valuable advice and discussions. I also want to thank Zahirul and Bingun for their support and help throughout these years. I acknowledge the contributions of Dr. Archana Sekar, a previous graduate student from Li group.

I am grateful for the financial support provided by NSF and Hydrograph. I would like to thank the Chemistry department for awarding me a Graduate Teaching Assistantship. Additionally, I am thankful to the K-State Chemistry Alumni for providing me with a Graduate Scholarship in Summer,2021.

I want to acknowledge the Bangladesh Student Association for their support.

Finally, I would like to express my deepest and eternal gratitude to my family. Their unwavering belief in me and their support for my educational pursuits, even halfway across the world, mean the world to me. Their endless sacrifices, motivation, and prayers have helped me overcome every obstacle and move forward in life. They are my strength, and I would not be the person I am today without them.

Dedication

To my Parents!

For their love and continuous support…

List of Abbreviations

CTAB	Cetyl trimethyl ammonium bromide
SDS	Sodium decyl sulfate.
AC	Activated carbon
Licap	Free-standing AC film.
CDI	Capacitive deionization.
SAC	Salt adsorption capacity.
SDC	Salt desorption capacity
CE	Charge efficiency.
NCDI	Normal CDI (zero voltage discharge mode). Here, the voltage profile is +1.20 V for 20 minutes and followed by 0 V for 20 minutes. For asymmetric cells, CTAB/AC is the positive electrode and SDS/AC is the negative electrode.
iCDI	Inverted CDI. Here, the voltage profile is -1.20 V for 20 minutes and followed by 0 V for 20 minutes. For asymmetric cells, SDS/AC is the positive electrode and CTAB/AC is the negative electrode.
Bipolar CDI	Conventional CDI (reverse voltage discharge). Here, the voltage profile is +1.20 V for 20 minutes and followed by -1.20 V for 20 minutes. For asymmetric cells, CTAB/AC is the positive electrode and SDS/AC is the negative electrode.
ORR	Oxygen reduction reaction.
LSV	Linear sweep voltammetry.
RDE	Rotating disk electrode.
RRDE	Rotating ring disk electrode.

Preface

The thesis focuses on the modification strategy of nanocarbon to use as an electrode or catalyst for the application in clean technologies such as water desalination and electrochemical H_2O_2 synthesis. The thesis comprises the following sections:

Chapter 1 overviews the water desalination and oxygen reduction reaction and discusses the working mechanism.

Chapter 2: This chapter gives an overview of the modification of activated carbon by cationic and anionic surfactant with a strategy for quantifying and controlling surfactant loading. The applicability of the modified activated carbon was studied in capacitive deionization in different modes such as NCDI, i-CDI, and Bipolar CDI.

Chapter 3: This chapter focuses on the modification of graphitic carbon by post-thermal annealing. An electrocatalytic performance towards oxygen reduction reaction of the synthesized material was evaluated.

Chapter 4: This chapter summarizes the main findings of two major studies presented in the thesis and the future directions of this research.

Chapter 1 - Introduction

1.1-A basic introduction of carbon-based material and its prospects in clean technologies after modification

Carbon is known as a versatile element because of its tetravalency and catenation properties. It can form a wide range of 1D, 2D, and 3D allotropes such as graphene, fullerene, carbon nanotube (CNT), etc. as well as highly porous materials such as activated carbon (AC). Because of the rigid structures, high electrical conductivity, high specific surface area, porous nature, etc., this material has wide applications in different clean technologies such as wastewater treatment plant[1], water desalination plant[2], energy storage and conversion device[3], electrochemical synthesis[4], etc. However, many researchers have demonstrated that carbon material has limitations such as poor hydrophilicity, unstable conductivity and low active sites for specific applications[5]. To eliminate these limitations, some common strategies involve physical and chemical modification of carbon, such as heteroatom doping and surfactant adsorption. In this thesis, Chapter 2 will focus on the surfactant modification strategy on AC and its application in water desalination. Chapter 3 will focus on the exploration of N-doped graphitic carbon by post-growth thermal processing and its application in electrochemical H_2O_2 synthesis.

1.2-Introduction of capacitive de-ionization

Capacitive deionization (CDI) is an electrochemical technique to remove dissolved salts in water. Due to the applied voltage bias to the carbon electrodes, an electrical double layer formed around the carbon surface and the ions from the electrolyte get adsorbed to the electrode. For ion removal from the electrode, an opposite voltage bias or a shunt is applied to the electrodes.

1.2.a- Mechanism of capacitive deionization

The ions adsorb to the electrode by developing the electrical double layer after applying a voltage bias in between the electrode. This theory of electrical double layers was first introduced by Helmholtz and states that the charge of a planar electrode is neutralized by the electrostatically attracted counter ions from the bulk electrolyte to the electrode-electrolyte interface. The co-ions in the same solution are repelled by the electrode[6, 7]. That was further modified by Gouy and Chapman, who described that the ions accumulated in the electrode/electrolyte interface tend to diffuse back to the bulk solution due to thermal motion of the ions and thus forming a diffuse

layer[6, 8, 9]. That leads to an overestimation of the capacitance in high salt concentration, and this presents the failure of this model. Later Gouy-Chapman-Stern model was developed and stated

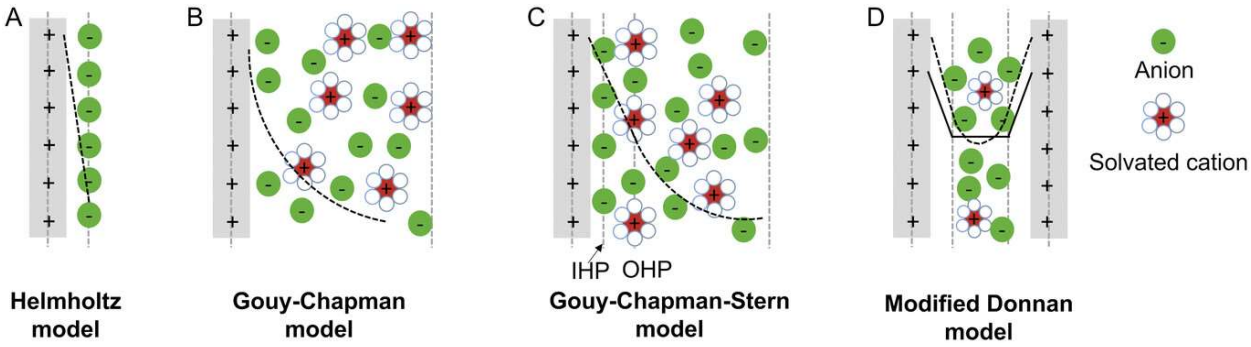

Figure 1-1: Models for describing the structure of an electrical double layer at a positively charged surface: (A) the Helmholtz model, (B) the Gouy–Chapman model, (C) the Stern model, and (D) the modified Donna model. Reprinted (adapted) with permission from K. Sun, M. Tebyetekerwa, C. Wang, X. Wang, X. Zhang, X. S. Zhao, Electrocapacitive Deionization: Mechanisms, Electrodes, and Cell Designs. Adv. Funct. Mater. 2023, 33, 2213578. Copyright © 2023, John Wiley and Sons.

that an electrical double layer in the inner micropores of CDI electrode consists of a compact layer and a diffuse layer[6, 10-12]. In the compact layer, the inner Helmholtz plane is the center of the counter ions directly in contact to the electrode[6] and the outer Helmholtz plane is the center of solvated ions nearest to the electrode[13]. But this model fails to describe the overlapping electrical double layer of micropore since the Debye length is larger than pore radius[14]. Later the modified Donnan model was able to successfully describe the overlapping of electrical double layers inside the micropores and this model has been used in theoretical prediction of salt adsorption and charge accumulation[15]. According to the modified Donnan model, the potential in the intraparticle pore is uniform and the Stern layer is located between electronic and ionic charges along with chemical attraction energy for ions transferring into intraparticle pores[15]. Based on this electrical double layer concept, an electrical charge develops in the electrode after applying a bias to the electrode. To neutralize this charge, the ions from the bulk solution are attracted towards the electrode due to electrostatic interaction and get adsorbed to the electrode. During the shunt or reversing voltage, the ions are repelled from the electrode and get desorbed into the bulk solution.

Classification of CDI

The CDI cells can be classified based on advanced cell configuration, based on electrode materials, based on cell geometry, based on composition of the anode and cathode, Based on mode of discharge method (such as zero voltage discharge and reverse voltage discharge) [16].

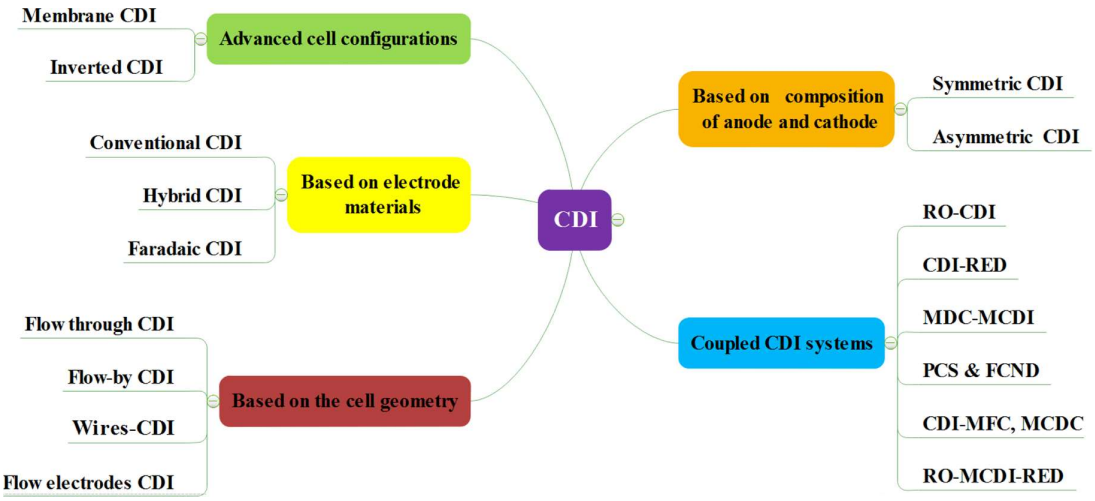

Figure 1-2:Classifications of CDI. Reprinted (adapted) with permission from Samuel Ntakirutimana et al 2020 J. Electrochem. Soc. 167 143501. Copyright © 2020, Journal of The Electrochemical Society.

This study focuses on the flow-by-cell architecture in which two carbon electrodes are oppositely placed and separated by a non-conductive spacer, and the solution flows through the cell between the two electrode plates from the periphery toward the exit opened in the top electrode [10]. The waveform applied on the two electrodes is configured in three modes, i.e., (1) normal CDI in zero voltage discharge mode (NCDI); (2) inverted CDI (ICDI) with voltage waveform reversed from the NCDI; and (3) bipolar CDI which replaces the shunt in NCDI with an opposite voltage bias.

Normal CDI in zero voltage discharge mode (NCDI)

This is an extensively used method in literature [17, 18]. In this mode, the ions from the bulk solution get absorbed into the electrode at a constant voltage[10]. The solution concentration decreases as the salt ions adsorbed on opposite electrodes. The rate of salt ion adsorption slows down until the electrode pores get saturated. In the zero-voltage discharge mode, the cell is shunted so the ions adsorbed to the electrical double layer get desorbed spontaneously. Initially, the

solution concentration increases rapidly and after sufficient desorption time, it returns to feed solution concentration[10].

Bipolar CDI (reverse voltage discharge mode)

In this mode, the Ion adsorption step is similar to CDI-ZVD mode. In the reverse discharge mode, ion desorption happened due to both reverse electric field and spontaneous desorption process. The desorption of ions from the electrode continues until counter ions deplete from the electrode which result in more space for counter-ions to adsorbed to the electrodes in next adsorption cycle[10, 19] .

Inverted CDI (i-CDI)

The inverted CDI cell configuration is opposite of conventional CDI. This involves modifying the surface of the two electrodes with positive and negative charges, respectively. The ion adsorption occurs passively during shunt and an external voltage is applied for ion desorption[20]. The reason is that, in I-CDI, a negatively charged functionalized electrode serves as a working electrode, and a relatively positive charged electrode serves as the counter electrode. During applying -1.20 V bias, the dominant mechanism is co-ion repulsion[21] and during shunt the dominant mechanism is electrostatic attraction of counter ions.

1.3-Introduction of oxygen reduction reaction

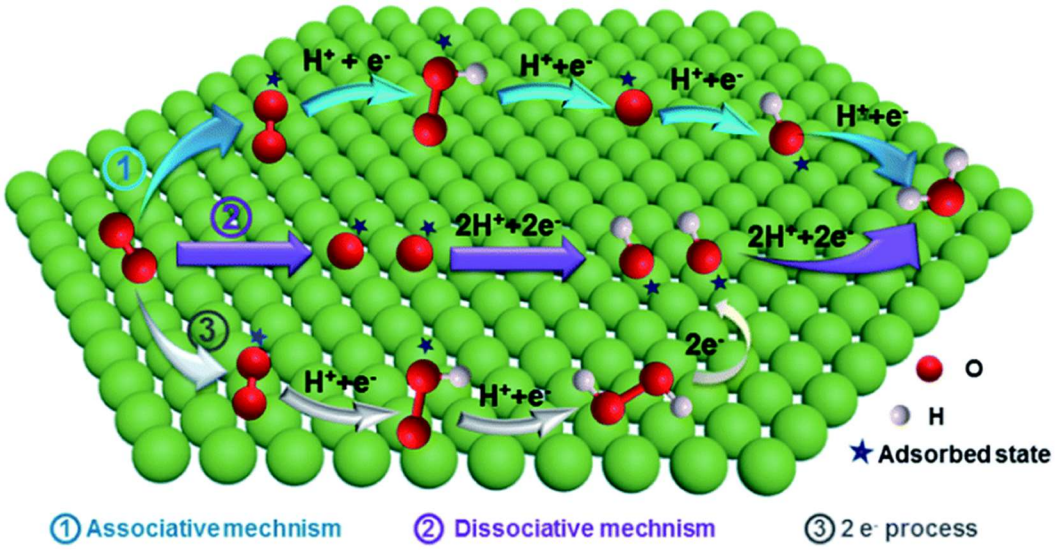

Figure 1-3: Oxygen reduction reaction mechanism. Reprinted (adapted) with permission from J. Mater. Chem. A, 2019,7, 1964-1988. Copyright © 2019, Royal Society of Chemistry.

In energy storage and conversion devices such as metal-air batteries or H_2-O_2 fuel cells, O_2 is introduced in the cathode compartment. It undergoes oxygen reduction reaction (ORR) by accepting electron from the electrode. The reduction reaction can go through $2e^-$ pathways or $4e^-$ pathways. Depending on the number of electron transfer, the final product can be H_2O or H_2O_2 (Figure 1-3)[22].

1.4-Common electrochemical characterization technique

Cyclic Voltammetry (CV)

CV is the most common electrochemical technique for obtaining qualitative and quantitative information about an electrode or a catalyst. A triangular voltage vs. time waveform is applied to the working electrode, and the corresponding current response is recorded. The responded current signs indicate the oxidation or reduction process. Apart from understanding the oxidation and reduction reaction, a CV is also useful for gaining quantitative information about a system.

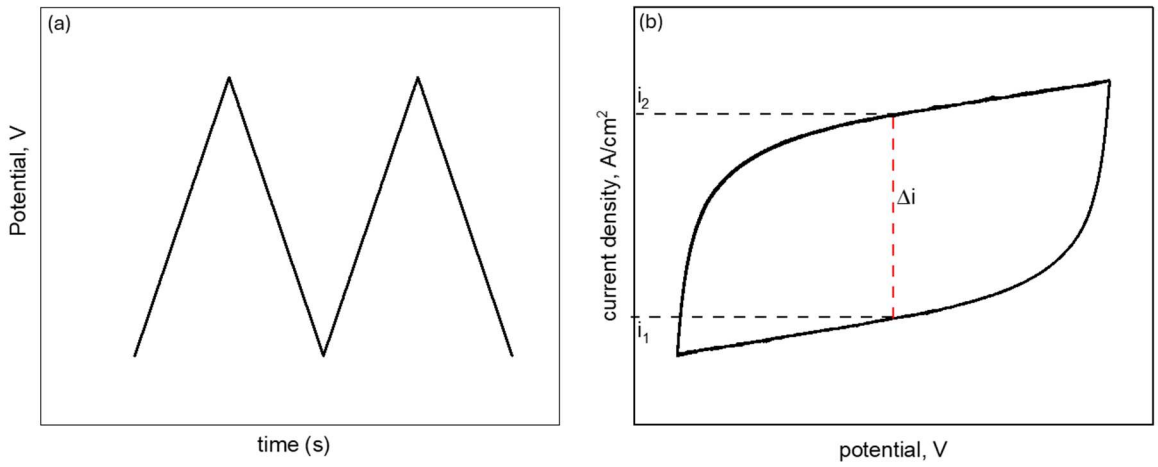

Figure 1-4: (a) waveform for a cyclic voltammetry, and (b) a representative cyclic voltammograms from an electrochemical double layer capacitor.

From a CV profile, the areal cell capacitance (C_{cell}), area-specific cell capacitance of an electrode ($C_{s\text{-electrode}}$), and mass-specific capacitance of an electrode ($C_{m\text{-electrode}}$) can be calculated using equations (1.1), (1.2) and (1.3).

$$C_{cell}\left(\frac{F}{cm^2}\right) = \frac{\frac{\Delta i}{2}}{\vartheta} \quad \text{..... (1.1)}$$

$$C_{s\text{-electrode}}\left(\frac{F}{cm^2}\right) = 2x\frac{\frac{\Delta i}{2}}{\vartheta} \quad \text{..... (1.2)}$$

$$C_{m\text{-electrode}}\left(\frac{F}{g}\right) = \frac{C_{s-electrode}}{m} \quad \text{..... (1.3)}$$

Here, Δi = the differences in current density at a potential in the capacitive region ($\frac{A}{cm^2}$)

ϑ = scan rate ($\frac{V}{s}$)

m = mass loading of an electrode ($\frac{g}{cm^2}$)

Chapter 2 - Electrochemical brackish water desalination by capacitive deionization

2.1-Introduction

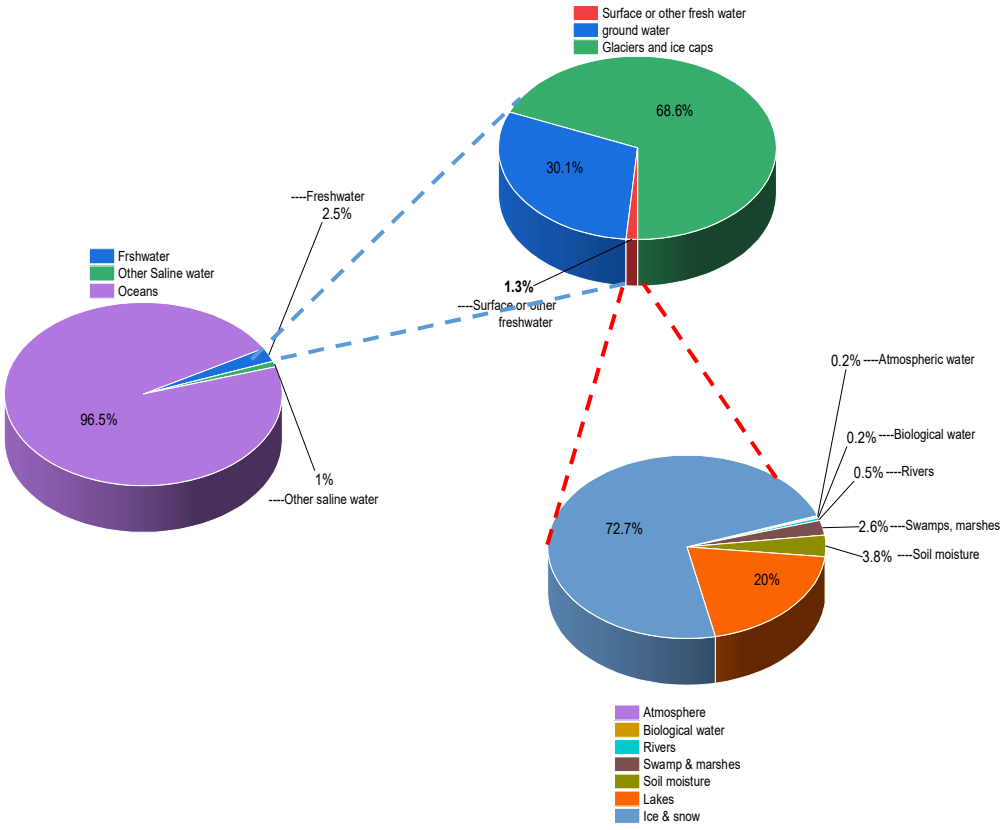

Figure 2-1: Distribution of Earth's water. source: Igor shiklomanov's chapter "world freshwater resources" in Gleick, Peter, and Gilbert F. White. 1993. Water in crisis: a guide to the world's freshwater resources. New York: Oxford University Press. (Numbers are rounded)

Of the total earth's water, only 2.5% is freshwater. In this total freshwater, 68.6% percent is from glaciers and icecaps, 30.1% is in groundwater, and the remaining 1.3% is ready-to-use fresh water (Figure-2-1)[23]. However, due to the drastic climate change, severe natural disasters, contamination from industrial waste, and other sources, the volume of available ready-to-use fresh water is depleting. That is why freshwater shortage is one of the major concerns in today's world.

So, this is the right time to develop technology to purify the freshwater from industrial waste and look for a new alternative source of fresh water. Groundwater is considered one of the alternative sources of fresh water. However, its usability for daily purposes is compromised by its high salinity levels (4000 ppm - 10,000 ppm)[24]. The primary reason is saltwater intrusion triggered by both natural geological formations and human activities[25]. Over the years, a number of technologies have been developed, such as multistage flash distillation, multi-effect distillation, electrodialysis, and reverse osmosis[26]. However, these techniques are not cost-effective and energy-inefficient due to high energy consumption, heavy equipment, and complicated membrane systems[27]. Capacitive de-ionization (CDI) is an emerging electrochemical desalination technique that is an alternative to the other technologies. This device desalinates low-concentration salt water by electrostatically adsorbing ions via electrical double layer (EDL) formation at the electrode-electrolyte interface[28].

Activated carbon is a commonly used electrode material for CDI because of its well-connected pore structure (micropore and mesopore), high specific surface area (SSA), and good electrical conductivity[28]. The micropores (pore size < 2 nm) play an essential role in charge accumulation and the mesopores help in transporting ions to micropores and partial ion adsorption [29, 30]. The large micro- and meso- pore volume contributes to a high salt adsorption capacity and fast ion adsorption kinetics[31].

In a CDI cycle, charged ions get adsorbed to the electrode during charging, and during discharging/regeneration, the adsorbed ions get desorbed from the electrode [19]. However, due to the adsorption of co-ions (i.e., the ions with the same type of charge as that on the electrode surface), the charge efficiency (ions absorbed per charge) is a limiting factor [32, 33]. A cation exchange membrane (CEM) and an anion exchange membrane (AEM) in front of the carbon electrode can effectively block co-ion adsorption. They can effectively improve the charge efficiency since CEM is only selective to cations, and AEM is only selective to anions[12, 34]. Later, many researchers have identified different CEMs such as crosslinked sulfonated polystyrene[35], sulfonated bromo methylated poly (2,6-dimethyl-1,4- phenylene oxide) coated sulfonated graphene[36] and sulfonated poly phenyl oxide[37], and AEMs such as aminated PVA[36, 38], aminated PSF[37, 39] and aminated graphene[17] for membrane-CDI (MCDI).

This study aims to find a low-cost surfactant-modified activated carbon (AC) synthesis to use as an electrode in the CDI process. For this purpose, A detailed study of quantifiable and controllable surfactant-impregnation to AC powder and pre-coated AC electrode has been studied. The influence of surfactant impregnation on AC powder and pre-coated AC was evaluated from electrochemical and electro-sorption performance.

2.2-Materials

AC and free-standing AC film (Licap) were obtained from Licap Technologies Inc. (Sacramento, CA, USA). Sodium chloride (NaCl), cetyltrimethylammonium bromide (CTAB, aMRESCO, Ohio, USA) and sodium dodecyl sulfate (SDS, JT Baker, Japan). Sodium carboxy methyl cellulose (average MW ~90,000 & 700,000), polyacrylic acid (PAA), and methyl orange were purchased from Sigma Aldrich (St. Louis, Missouri, USA). Methylene blue was obtained from Santa Cruz Biotechnology, Inc. (Dallas, Texas, U.S.A). A 250-um thick graphite foil from Mineral Seal Co. (Arizona, USA) was used as the substrate for coating AC films as the CDI electrodes, A 400 um thick graphite foil was used at the back of the electrodes as the current collector to a good electrical connection. A Millipore water system (EASYPURE II, Thermo Scientific, Waltham, MA) was used for ultrapure water (18.2 MΩ-cm at 25 °C) to prepare solutions for the experiments.

2.3-Material characterization techniques

UV-Vis's measurements were done by a Varian Cary 500 UV-Vis-NIR spectrophotometer (with a wavelength accuracy of $\pm$ 0.1 nm for UV-Vis light). Two 3cm x 1cm x 1cm quartz cuvettes was used as a liquid sample and blank control. BET surface areas, micropore volumes, and pore size distributions were derived from N_2 isotherm data collected at 77.35 K (Autosorb iQ Station 1, Quantachrome Corporation, Boynton Beach, FL, USA). Before analysis, the samples were outgassed overnight at 333 K. N_2 isotherms were obtained over a relative pressure range (P/P_0) from $1.0x10^{-6}$ to 1.00, where P_0 is the saturated vapor pressure of N_2 at liquid nitrogen temperature. The BET isotherms were used to derive the BET surface area and pore size distribution. BET data processing and calculation were carried out by Quantachrome® ASiQwin software (version 5.22), which uses the non-local density functional theory equilibrium model (NLDFT). The zeta potential measurement was done by the malvern Zetasizer Nano ZSP. The material composition was

determined using a Thermogravimetric Analyzer (TGA) Q50 system (TA Instruments, Waters LLC, New Castle, DC) from the room temperature to 900 °C in an N_2 atmosphere at a heating rate of 10 ºC/min.

2.4-Properties and characterization of activated carbon

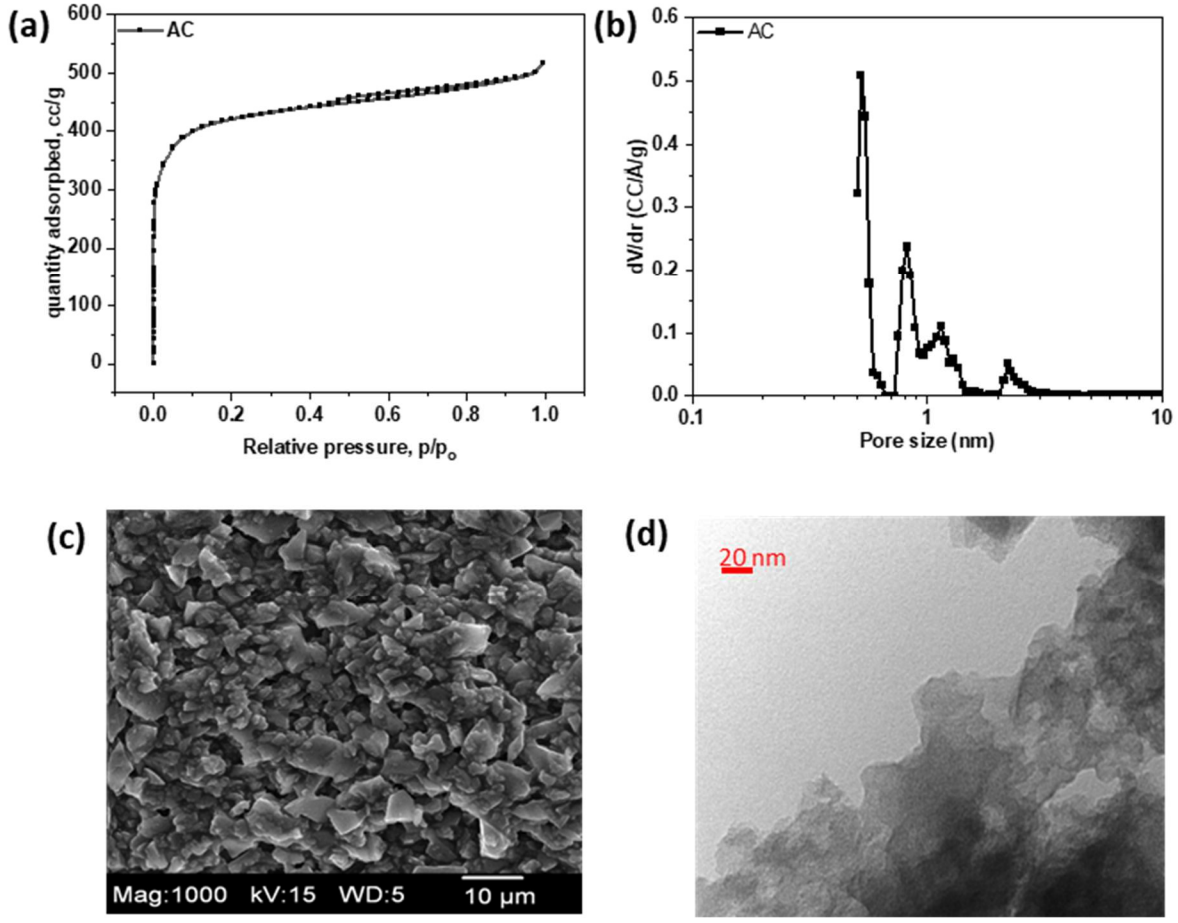

Figure 2-2:Properties of the activated carbon: (a) BET isotherm, (b) pore size distribution plot, (c) SEM image, and (d) TEM image.

The pore structure, pore size, and specific surface area (SSA) were derived from N_2 adsorption-desorption isotherm analysis. The N_2 adsorption-desorption isotherms and pore size distribution of AC are presented in Figures 2-2(a) and 2-2(b). The N_2 adsorption-desorption isotherm shows a high adsorption below 0.1 relative pressure P/P_0, which indicates the microporous structure of the material, and a hysteresis loop (due to capillary condensation) at ~0.45 to 1 relative pressure which indicates the mesoporous characteristics (type IV). Such duo

characteristics are due to the presence of both microporous and mesopores[30]. The BET SSA of AC is 1541.8 m^2/g, and the total pore volume is 0.713 cc/g, of which 69.1% of the contribution is from micropores and 30.7% is from mesopores. The average pore size is 5.24 Å. In contrast, the particle size of AC is in the range of 100 nm to 10 um (Figure 2-2(c)). So, the micropores are likely effectively connected through mesopores inside each AC particle, which are barely seen in the TEM image in Figure 2-2(d).

2.5-Adsorption kinetics of impregnating CTAB on AC powder

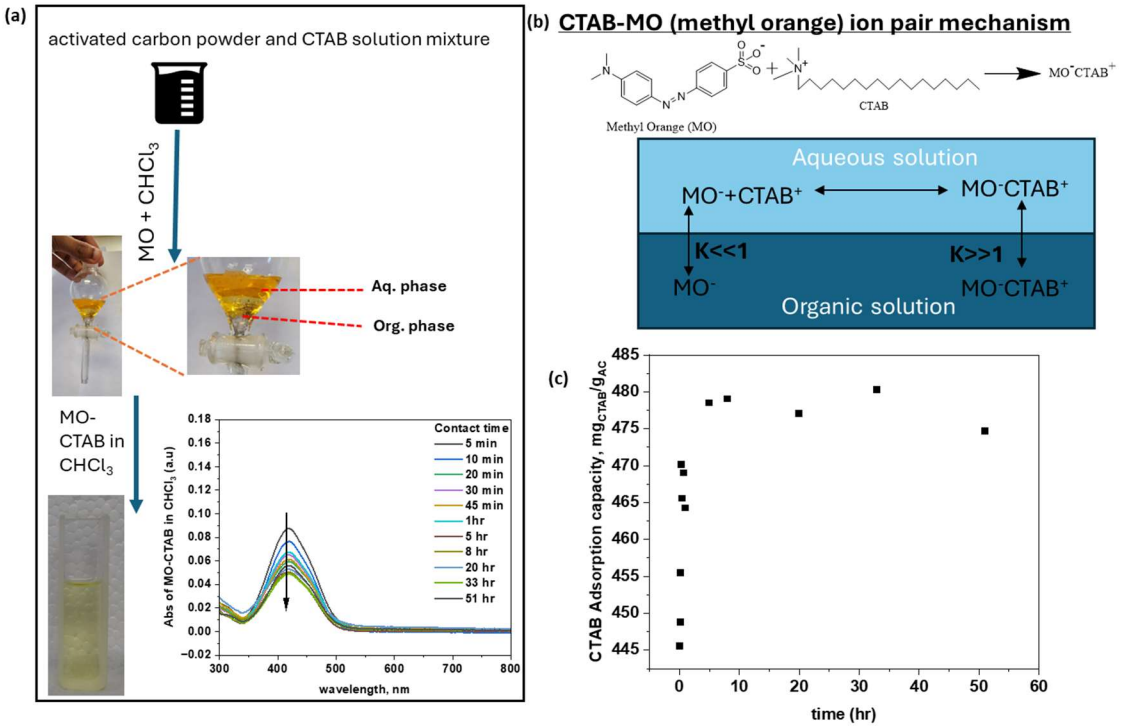

Figure 2-3:(a) Determination procedure of free CTAB in solution, (b) MO-CTAB ion pair mechanism, and (c) CTAB adsorption capacity over time (inset shows the representative UV-Vis adsorption by MO-CTAB complex in $CHCl_3$)

Cationic surfactant CTAB was used to modify the AC surface[18]. An amount of 1.41 mmol (55.5 mg) of CTAB was dissolved in 1.00 L ultrapure water and stirred in the solution for 5 minutes at 650 rpm to make a solution of0.47 mM (half critical micelle concentration (CMC) of CTAB). Then, 100 mg of AC (at the weight ratio of AC: CTAB = 1.8: 1) was added to the prepared CTAB solution, stirred at a speed of 650 rpm for 8 hr, and then the mixed solution was kept at rest for 48 hr. During this experiment, to study the adsorption kinetics of CTAB on AC, 4.0 mL supernatant was periodically collected after 5 min, 10 min, 20 min, 30 min, 45 min, 60 min, 5 hr,

8 hr, 20 hr, 33 hr and 56 hr to examine the amount of CTAB left in the solution. This quantity is then converted into the capacity of CTAB adsorption on the AC (in mg_{CTAB}/g_{AC}) as shown in Figure 2-3(c).

The CTAB concentration in the aqueous solution was derived by an assay based on UV-Vis absorbance of an organic dye after it formed a complex with CTAB, which was then effectively extracted into an organic solvent ($CHCl_3$), as illustrated in Figures 2-3(a)&(b). Before the sample analysis, a calibration curve (Appendix Figures A2(a) & A2(b)) for CTAB was prepared using the procedure adopted from the literature [40, 41]. To prepare the calibration standard sample for UV-Vis analysis, 2.0 mL of the CTAB solution at a series of varied concentrations was mixed with 4.0 mL phosphate buffer (pH = 7.2), 2.0 mL of 0.15 mM methyl orange (MO), and 2.0 mL DI water in a separatory funnel and was then vigorously shaken for a few minutes. The positively charged CTAB and negatively charged MO form ion pairs (MO^--$CTAB^+$) (Figure 2-3(b)), which are highly soluble in $CHCl_3$ [40]. 10.0 mL $CHCl_3$ was added to the mixture and was vigorously shaken for 5 minutes. After being kept in the stand for 5 minutes, the solution separated into two phases. The organic phase at the lower portion was collected from which 3.0 mL solution was taken in a cuvette for the UV-Vis absorbance analysis. Then, the absorbance of the $MO^{--}CTAB^+$ complex at 419 nm was plotted against the CTAB concentration (in ppm) as shown in Appendix B-1(a)[41].

The free CTAB concentration left in the water, $[CTAB]_{aq}$, during the adsorption process can be derived by taking the 4.0 mL sampling solution through the same procedure as the calibration process. From the UV-Vis analysis, the mass of free CTAB in the sample, $M_{CTAB,\,aq}$, was quantified using Equation (2.1) to derive the mass of CTAB adsorption on AC, $M_{CTAB,\,AC}$ (in mg_{CTAB}/g_{AC}), using Equation (2.2)

$$M_{CTAB,aq}(\mathrm{mg_{CTAB}}) = [CTAB]_{aq} \times V_{aq} \quad \text{..... (2.1)}$$

$$M_{CTAB,AC}\left(\frac{\mathrm{mg_{CTAB}}}{\mathrm{g_{AC}}}\right) = \frac{(M_{CTAB,0} - M_{CTAB,aq})}{M_{AC}} \quad \text{..... (2.2)}$$

where V_{aq} is the remaining water volume after sampling in L, $M_{CTAB,0}$ is the mg mass of CTAB (55.5 mg) initially added to the 1.0 L water, and M_{AC} (0.1 g) is the g amount of AC used for CTAB adsorption. Figure 2-3 (a) presents the adsorption capacity of CTAB on AC over time. It shows that, within 8 hr, CTAB adsorption on AC reaches its maximum adsorption capacity, 479.02 mg_{CTAB}/g_{AC}. The equilibrium CTAB adsorption capacity is 477.89 $\pm$ 2.98 (95%CI) mg_{CTAB}/g_{AC}.

2.6-Adsorption kinetics of SDS on AC powder

Anionic surfactant SDS was used to modify AC surface[18]. An amount of 2.05 mmol (590.7 mg) of SDS was dissolved in 500.0 mL ultrapure water and stirred the solution for 5 minutes

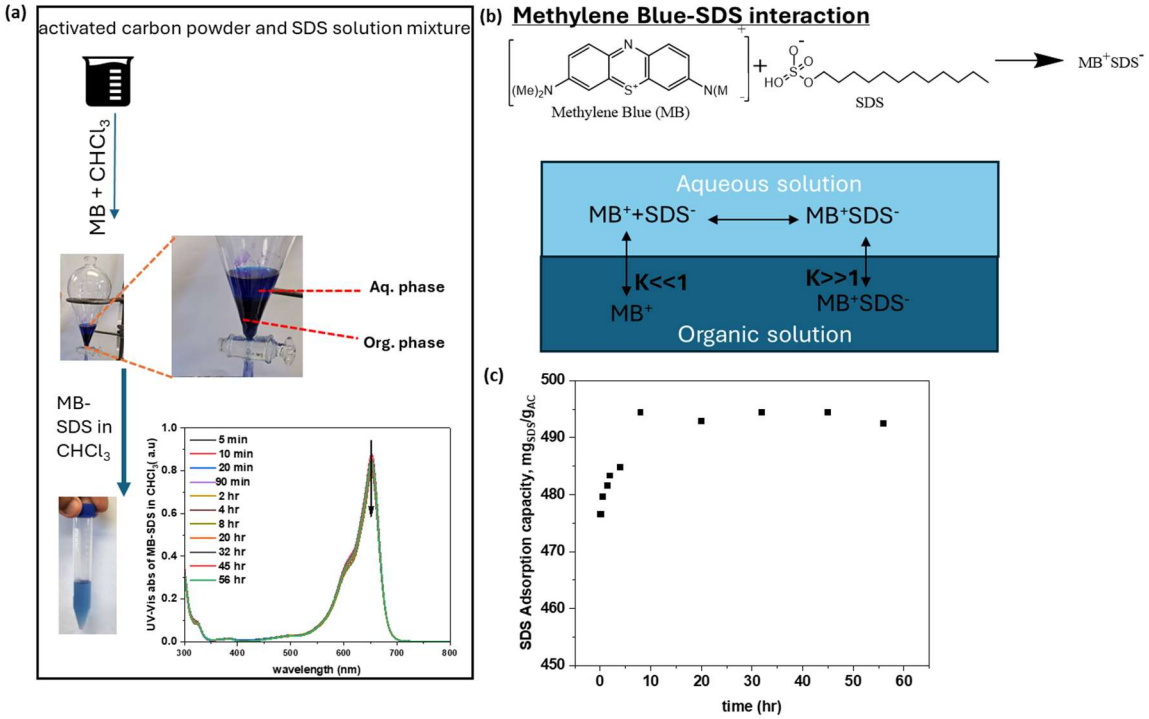

Figure 2-4: (a) quantification procedure of free SDS remained in solution, (b) SDS-MB interaction, and (c) SDS adsorption capacity over time (inset UV-Vis adsorption by MB-SDS complex in $CHCl_3$)

at 650 rpm to make a homogeneous solution of 4.1 mM (half of CMC). Then, 991 mg of AC (the wt. ratio of AC: SDS = 1.7: 1) was added to the prepared SDS solution, stirred at a speed of 650 rpm for 8 hr, and then kept at rest for 48 hours. During this experiment to study the adsorption kinetics of CTAB on AC, 4.0 mL supernatant was periodically collected after 5 min, 10 min, 20 min, 30 min, 45 min, 60 min, 5 hr, 8 hr, 20 hr, 32 hr, 45 hr and 56 hr to examine the amount of SDS left in the solution. This quantity is then converted into the capacity of SDS adsorption on the AC (in mg_{SDS}/g_{AC}) as shown in Figure 2-4(c).

The SDS concentration in the aqueous solution was derived by an assay based on UV-Vis absorbance of an organic dye after it formed a complex with SDS, which was then effectively extracted into an organic solvent ($CHCl_3$), as illustrated in Figures 2-4(a)&(b). Before the sample analysis, a calibration curve (Figures A4(a) & A4(b)) for the SDS quantification was prepared using the procedure adopted from the literature[42]. To prepare the calibration standard sample for UV-Vis's analysis, 10 mL of the SDS solution at a series of concentrations was mixed with 2.5

mL 300 ppm methylene blue (7.5 mg MB dissolved in 25 mL pH 7.2 phosphate buffer). The negatively charged SDS and positively charged MB form an organic salt (MB^+-SDS^-), which gets dissolved in $CHCl_3$ (Figure 2-4(b)). Then, 10 mL $CHCl_3$ was added, vigorously shaken for 5 minutes, and kept in the stand for another 5 minutes. Then, the organic phase was collected, and 3 mL of sample was taken in a cuvette for the UV-Vis analysis. Then, the absorbance of the MB-SDS complex at 652 nm was plotted against the SDS concentration in ppm(Appendix A4(b)) [41].

The free SDS concentration left in the water, $[SDS]_{aq}$, during the adsorption process can be derived by taking the 0.5 mL sampling solution and diluted to 10 mL (dilution factor, DF =20), then following the same procedure as the calibration process. From the UV-Vis analysis, the mass of free SDS in the sample, $M_{SDS,\,aq}$, was quantified using Equation (2.3 and 2.4) to derive the mass of SDS adsorption on AC, $M_{SDS,AC}$ (in mg_{CTAB}/g_{AC}), using Equation (2.5)

$$[SDS]'_{aq} = [SDS]_{aq} \times DF \quad \text{..... (2.3)}$$

$$M_{SDS,aq}(\mathrm{mg_{SDS}}) = [SDS]'_{aq} \times V_{aq} \quad \text{..... (2.4)}$$

$$M_{SDS,AC}\left(\frac{\mathrm{mg_{SDS}}}{\mathrm{g_{AC}}}\right) = \frac{(M_{SDS,0} - M_{SDS,aq})}{M_{AC}} \quad \text{..... (2.5)}$$

where V_{aq} is the remaining water volume after sampling, $M_{SDS,0}$ is the mass of SDS (590.7 mg) initially added to the 500.0 mL water, and M_{AC} (991 mg) is the amount of AC used for SDS derivation.

Figure 2-4 (a) presents the adsorption capacity of SDS on AC over time; it shows that within 8 hrs, SDS adsorption on AC reached its maximum adsorption capacity, 492.39 mg_{SDS}/g_{AC}. The equilibrium SDS adsorption capacity is 493.65 $\pm$ 1.34 (95% CI) $mg_{SDS}/g_{AC.}$

2.7-Material synthesis

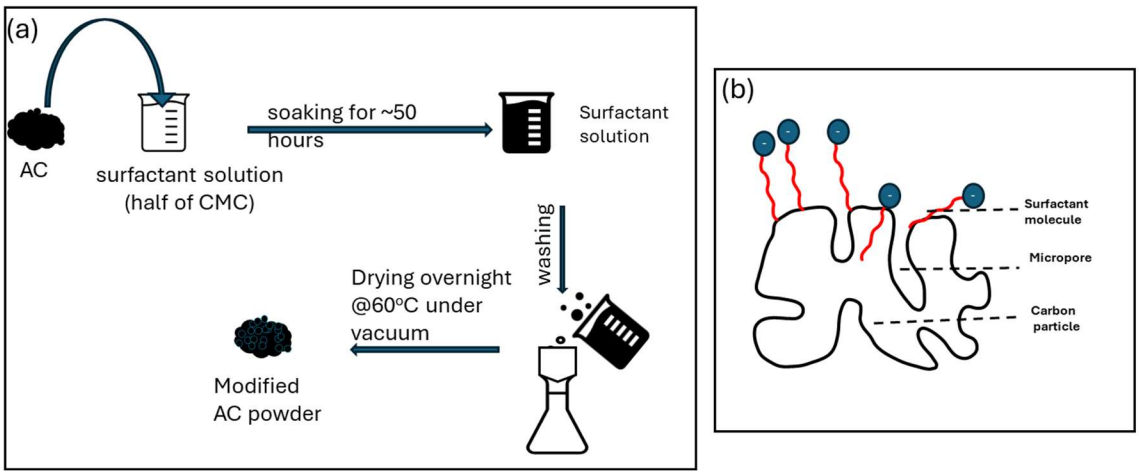

Figure 2-5:(a) Modification strategy of activated carbon powder by SDS and CTAB, and (b) Surfactant adsorption mechanism.

2.7.a. CTAB impregnation on AC

After knowing the saturation surfactant loading on AC powder based on 100 mg AC experiments, the AC quantity of AC is scaled up to 10 g to prepare sufficient materials for CDI experiments. The modification of AC powder was done in 0.47 mM CTAB solution. [18, 43]. The CMC of CTAB is 0.92 mM. 10.0 g AC well mixed in 1.0 L DI water. To keep the solution concentration below the CMC concentration of CTAB, each time 0.47 mmol CTAB was added to the 1.0 L solution mixture and stirred for 1hr. In total, 13.16 mmol CTAB was added in 28 segments. UV-Vis's analysis was done after 20th, 26th, 27th, and 28th CTAB addition. From the UV-Vis analysis, the UV-Vis absorbance did not show significant change in 1 hr after the 28^{th} addition of CTAB comparing to that after keeping the solution overnight, indicating that the surface of AC got saturated by CTAB. From the UV-Vis analysis, the CTAB adsorption capacity on AC is 481.3 mg_{CTAB}/g_{AC} (101.5% of the maximum CTAB adsorption capacity obtained in section-2.5). Thus this sample was labeled as 101.5% CTAB/AC. Then, the solution mixture was filtered out using a Buchner funnel, and the sample was washed several times with ultrapure water. The 101.5% CTAB/AC sample was then dried in a vacuum oven at 60°C overnight.

2.7.b. SDS impregnation on AC

The SDS modification of the large amount of AC was done in a similar way in 4.1mM SDS [18, 43]. The CMC of SDS is 8.2 mM. First, 10.3 g AC was well mixed in 1.0 L DI water. To keep the solution concentration below the CMC of SDS, 4.09 mmol SDS was added to the 1.0 L solution mixture and stirred for 1hr. In total, 16.36 mmol SDS was added in 4 segments. UV-Vis's analysis was done after the 3rd, and 4th SDS addition. After the 4^{th} SDS addition, the UV-Vis absorbance was the same in 1 hr after mixing compared to that after keeping the solution for overnight the absorbance, indicating that SDS saturated the AC surface. From the UV-Vis analysis, the SDS adsorption capacity on AC is 433.9 mg_{SDS}/g_{AC} (88.1% of the maximum SDS adsorption capacity obtained in section 2.6). Thus, this sample was labeled as 88.1% SDS/AC. Then, the solution mixture was filtered using a Buchner funnel, and the sample was washed several times with DI water. The 88.1% SDS/AC sample was then dried in a vacuum oven at 60^{o}C overnight.

2.8-Material characterization of SDS and CTAB -Impregnated AC powder

The TGA curves for AC, 101.5% CTAB/AC, 88.1% SDS/AC, and the control sample CTAB and SDS were presented in Figures 2-6(a) and 2-6(b). The initial weight percentage loss in < 200 ^{o}C is due to moisture removal from a sample[44].

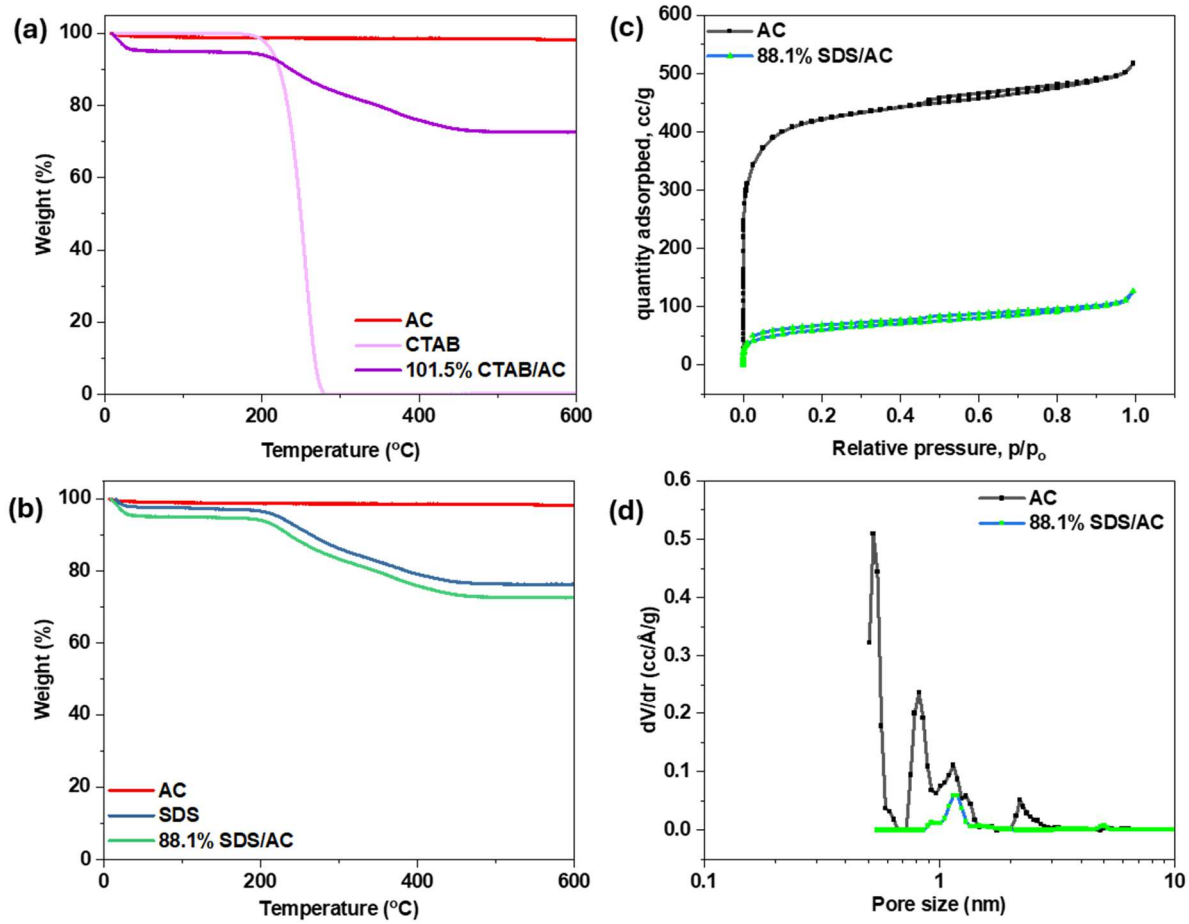

Figure 2-6:(a) TGA plot of AC, CTAB, 101.5% CTAB/AC (b) TGA plot of AC, SDS, 88.1% SDS/AC (c) BET isotherm of AC and 88.1% SDS/AC (d) pore size distribution plot of AC and 88.1% SDS/AC

Table 2-1:Weight % calculated from TGA.

• Weight % of AC = 66.8% • Weight% of CTAB = 30.3% • Weight % adsorbed moisture =2.9%	• Weight % of AC = 65.5% • Weight% of SDS = 29.4% • Weight % adsorbed moisture =5.1%

The weight loss from 200 -600 C is due to the decomposition of SDS and CTAB since the weight percentage of AC control samples stays nearly constant up to 600°C temperature. Based on these observations and reaction stoichiometry, the weight % of each component can be derived. From the TGA analysis, the composition of 88.1% SDS/AC and 101.5% CTAB/AC is presented in Table 2-1. The detailed explanations and calculations of TGA are given in the SI file: the weight percentage of CTAB and AC in 101.5% CTAB/AC is 66.8% and 33.3%, respectively, and that

corresponds to 498.0.5 mg_{CTAB}/g_{AC} of CTAB adsorption capacity on AC (i.e., ~105% relative to the saturated CTAB loading determined in the previous section). The weight % of SDS and AC in 88.1% SDS/AC is 29.93% SDS and 65.53% AC, and that corresponds to 456.7 mg_{SDS}/g_{AC} SDS adsorption capacity on AC (i.e., 92.8% relative to the saturated SDS loading determined in the previous section). The relative surfactant loadings on the AC powder derived by TGA are within 3.5% and 4.7% from those derived by the UV-Vis measurements, respectively, which validates that these quantities are reliable despite the system is very complicated.

Table 2-2: BET measurements

Materials	Specific surface area (m^2/g)	Total pore volume (cc/g)	% Micropore = ($V_{micropore}/V_{total}$) x100	% Mesopore = ($V_{mesopore}/V_{total}$) x100	Averge pore size (Å)
AC	1541.8	0.713	69.14	30.72	5.24
88.1% SDS/AC	189.4	0.16	51.25	48.75	11.93

The N_2 adsorption-desorption isotherm of AC and SDS/AC and pore size distribution are presented in Figure 2-6(c) and Figure 2-6 (d). The N_2 adsorption-desorption isotherm of SDS/AC exhibits type I and type IV characteristics, indicating the presence of micropores and mesopores[30]. After SDS modification of the AC, the SAA is reduced by 87.7%. The total pore volume is reduced by 77.6% compared to the pristine AC, which can be attributed to the presence of SDS molecules inside the AC pore or at the pore's entrance, which can effectively block the pore during the measurements[16]. Also, the average pore size shifted from 5.24 Å to 11.93 Å.

The zeta potential of AC, 88.1% SDS/AC and 101.5% CTAB/AC is presented in Table 2-3. The zeta potential of the pristine AC was -33.4 mV. After impregnating CTAB molecules on the AC, due to the presence of the positively charged $-N^+R_3$ group, the surface charge of AC became more positive, and the zeta potential changed to +32.4 mV. The same phenomenon was observed after SDS modification of the AC. The zeta potential became -36.5 mV due to the presence of the negatively charged $-SO_3^-$ head group on the surface. These results indicate that CTAB and SDS molecules are successfully adsorbed onto the AC, which modulated the surface charge density.

Table 2-3:Zeta-potential measurements.

Sample	Zetapotential @ pH ~7
AC	-33.4 ± 6.5
88.1% SDS/AC	-36.5 ± 4.7
101.5% CTAB/AC	+32.4 ± 8.9

2.9-Preparation of AC electrodes

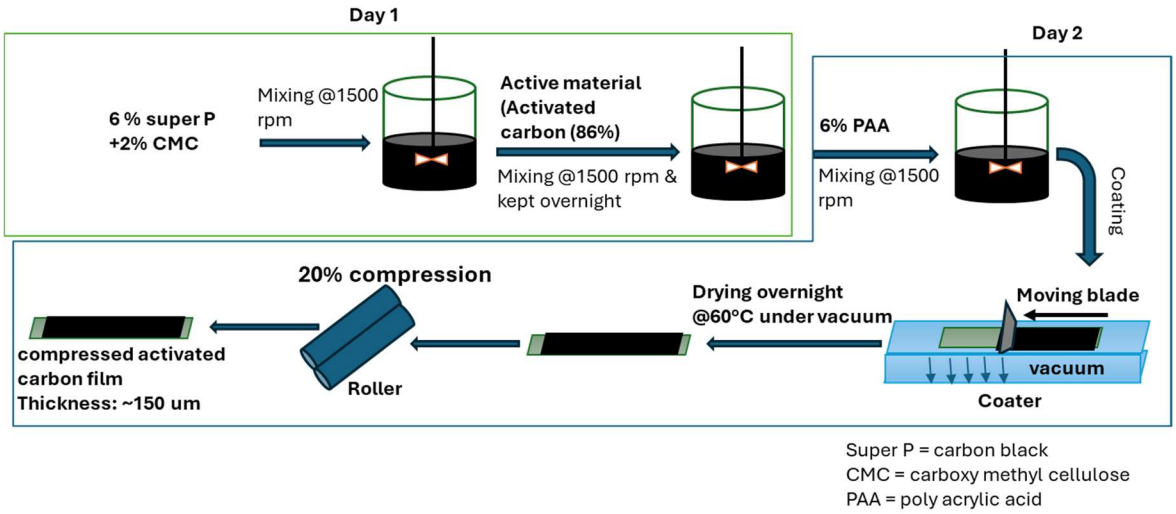

Figure 2-7:Preparation of electrode.

Super P (carbon black) was mixed with 2% carboxy methyl cellulose solution and stirred for 5 minutes at 1500 rpm. Then, the AC and water were added to the homogenous solution and stirred for 5 minutes at 1500 rpm. The homogeneous solution was kept overnight. The next day, 6% Poly acrylic acid (PAA) was added and stirred at 1000 ppm. The ratio of each component are AC : cellulose: CB : PAA = 86: 2 : 6: 6. Then the slurry was coated at room temperature on 250 mm thick graphite foil using a spreader with a fixed height of 800 mm at a speed of 20 mm/sec. The coated film was dried in a vacuum oven overnight at 60oC. After drying, the thickness of the coating was measured to be 170-190 um. The dried film was then compressed 20% by a roller. The final thickness was 140 um-150 mm. The areal AC mass loading of the electrode was found to be 6 to 9 mg/cm2. A pair of coated electrodes was directly used to assemble symmetric cells,

while other coated electrode was further modified by surfactant and used to prepare asymmetric cells. The surfactant modification on this precoated electrode is described in section-2.10.

2.10-Surfactant impregnation on pre-coated-AC electrodes

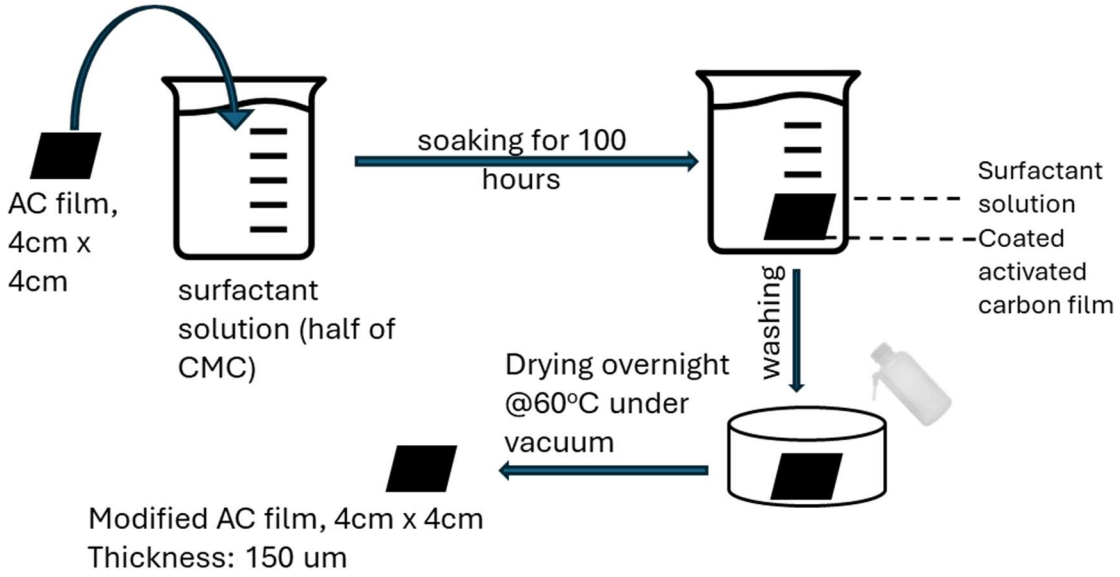

Figure 2-8: Surfactant modification of pre-coated AC electrodes.

2.10.a-CTAB modification on pre-coated AC electrodes:

440.0 mL 0.47 mM CTAB solution was prepared by adding CTAB in di-water and the solution mixture was stirred at a rate of 650 rpm for 5 minutes. Then a 4.0 cm x 4.0 cm 0.147 g of AC film was submerged in the solution mixture for 100 hr. During this experiment, the adsorption

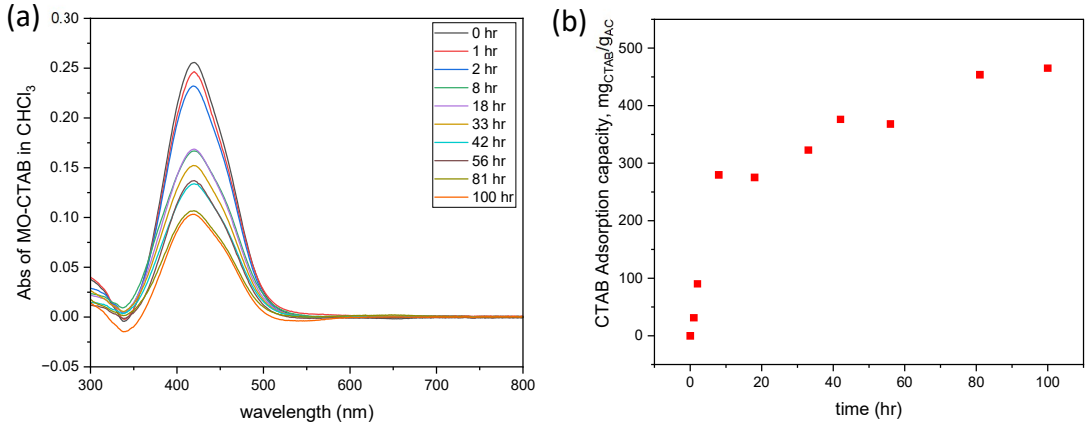

Figure 2-9: (a) UV-Vis absorbance of CTAB, and (b)Adsorption kinetics of CTAB on precoated AC.

kinetics of CTAB on AC was monitored by collecting 4.0 mL solution after 0 h., 1 hr, 2 hr, 8 hr, 18 hr, 33 hr, 42 hr, 56 hr, 81 hr and 100 hr, and analyzed by UV-Vis spectrophotometer following the same CTAB-MO extraction protocol mentioned in section-2.5. The CTAB adsorption kinetics on precoated AC is presented in Figure 2-9. The CTAB adsorption on precoated AC is slow, which could be due to the longer diffusion length due to the internal tortuous structure in the precoated AC electrode.

The CTAB adsorption capacity obtained after 100 hr is 465.26 mg_{CTAB}/g_{AC} (98.0% of the saturated CTAB adsorption capacity obtained in section 2.5). Thus, this sample was labeled as 98.0% CTAB/AC. Then, the electrode was washed several times with ultrapure water. The 98.0% CTAB/AC sample was then dried in a vacuum oven at 60 ^oC overnight.

Another sample was prepared by following the same procedure, but the electrode was immersed for 51 hr. After 51 hr of incubation, the UV-Vis analysis was done from which the obtained CTAB adsorption capacity is 257.8 mg_{CTAB}/g_{AC}, which is 54.3% of the saturated CTAB adsorption capacity obtained in section-2.5). The sample was labeled as 54.3% CTAB/AC.

2.10.b-SDS modification on the pre-coated AC electrodes:

75 mL 4.1 mM SDS solution was prepared by adding SDS on di-water and the solution mixture was stirred at 650 rpm for 5 minutes. Then a 4.0 cm x 4.0 cm 0.1491 g of AC film was submerged in the solution mixture for 100 hr. During this experiment, the adsorption kinetics of CTAB on AC was monitored by collecting a 4 mL solution after 0 hr, 1 hr, 8 hr, 18 hr, 33 hr, 42 hr, 56 hr, 81 hr and 100 hr, and analyzed by UV-Vis spectrophotometer following the same MB-

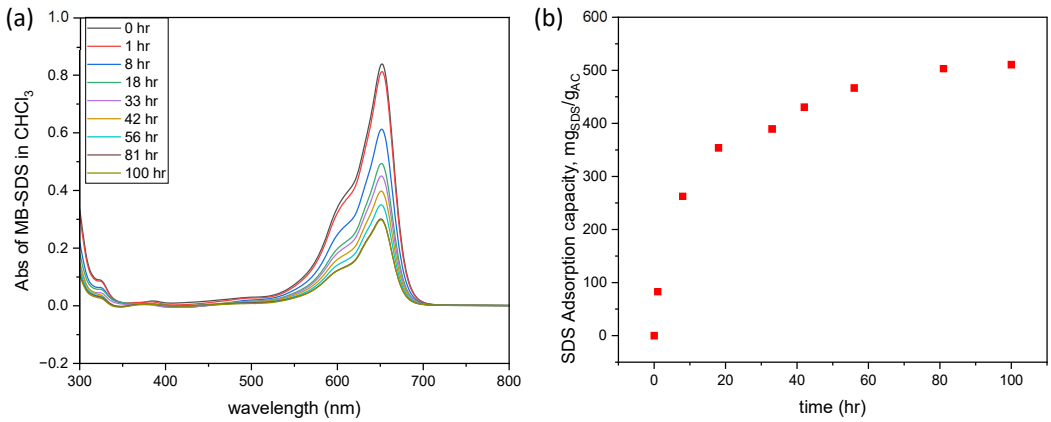

Figure 2-10: (a) UV-Vis absorption of CTAB, and (b) the adsorption kinetics of SDS on AC.

SDS complex extraction protocol mentioned in section-2.6. The SDS adsorption kinetics is presented in figure 2-10. The SDS adsorption is slow because of the long diffusion length due to the tortuosity in pre-coated AC electrode. The SDS adsorption capacity obtained after 100 hr was 511.01 mg_{SDS}/g_{AC} (i.e., 103.8% of the saturated SDS adsorption capacity obtained in section-2.6). Thus, this sample was labeled as 103.8% SDS/AC. Then, the electrode was washed several times with ultrapure water. The 103.8% SDS/AC sample was then dried in a vacuum oven at 60 ^{o}C overnight.

Another sample was prepared following the same procedure but immersing the electrode for 7.5 hr. After 7.5 hr incubation, the UV-Vis analysis was done from which the obtained SDS adsorption capacity was determined to be 232.56 mg_{SDS}/g_{AC} (that is 47.3% of the saturated SDS adsorption capacity obtained in section-2.6). The sample was labeled as 47.3% SDS/AC.

2.11-Electrochemical Characterization

The cyclic voltammetry (CV) and galvanostatic charge-discharge (GCD) were conducted on the CHI 760D electrochemical workstation (CH Instruments, Austin, TX) at room temperature. All the electrochemical characterization (CV and GCD) was done in 1.0 M NaCl and 17.11 mM NaCl (1000 ppm NaCl) in a two-electrode setup (Figure-9(d)). In the asymmetric cell setup, CTAB/AC was used as the working electrode and SDS/AC was used as counter electrode.

The CV in 1.0 M NaCl was carried out at 10 mV/s in a potential window between 0.0 V to +0.50 V and 0.0 V to +1.20 V and CV in 1000 ppm NaCl was carried out in 0.0 V to +1.20 V. The specific capacitance was calculated from the CV of short potential window (0.0 V to +0.50 V) by using equations (2.6), (2.7) & (2.8).

The capacitance of an electrode (mF/cm^2) = $2x\frac{\frac{\Delta i}{2}}{\vartheta}$……. (2.6)

Δi = the differences in current density at a potential in the capacitive region ($\frac{A}{cm^2}$)

ϑ = scan rate ($\frac{V}{s}$)

Capacitance of an electrode (F/g) = $\frac{\text{Capacitance of an electrode } (\frac{mF}{cm^2})}{Electrode\ mass\ loading\ (\frac{mg}{cm^2})}$…… (2.7)

The galvanostatic charge-discharge (GCD) was carried out at 0.40 A/g in the potential window of 0.0 V to +1.20 V. The specific capacitance was calculated from the discharge curve using the following equation.

Capacitance of an electrode (F/g) = $2x\frac{I}{m}\ x\frac{\Delta V}{\Delta t}$…… (2.8)

$$m = mass\ of\ the\ active\ electrode, g$$

$$I = current\ applied, A$$

$$\Delta V = potential\ difference\ in\ the\ discharge\ curve, V$$

$$\Delta t = time\ required\ for\ the\ discharge, sec$$

Table 2-4: Capacitance of the electrodes in 1.0 M NaCl

Cell	Area-specific capacitance of an electrode, $mF/cm^2_{AC\ film}$	Mass-specific capacitance of an electrode, $F/g_{AC\ film}$
Licap-Licap	207.09	38.15
Pristine AC-Pristine AC (140 um)	718.06	123.01
54.3% CTAB/AC-47.3% SDS/AC -precoated	682.06	81.19
98.0% CTAB/AC-103.8% SDS/AC -precoated	390.88	42.54
101.5% CTAB/AC-88.1% SDS/AC -powder	281.19	36.90

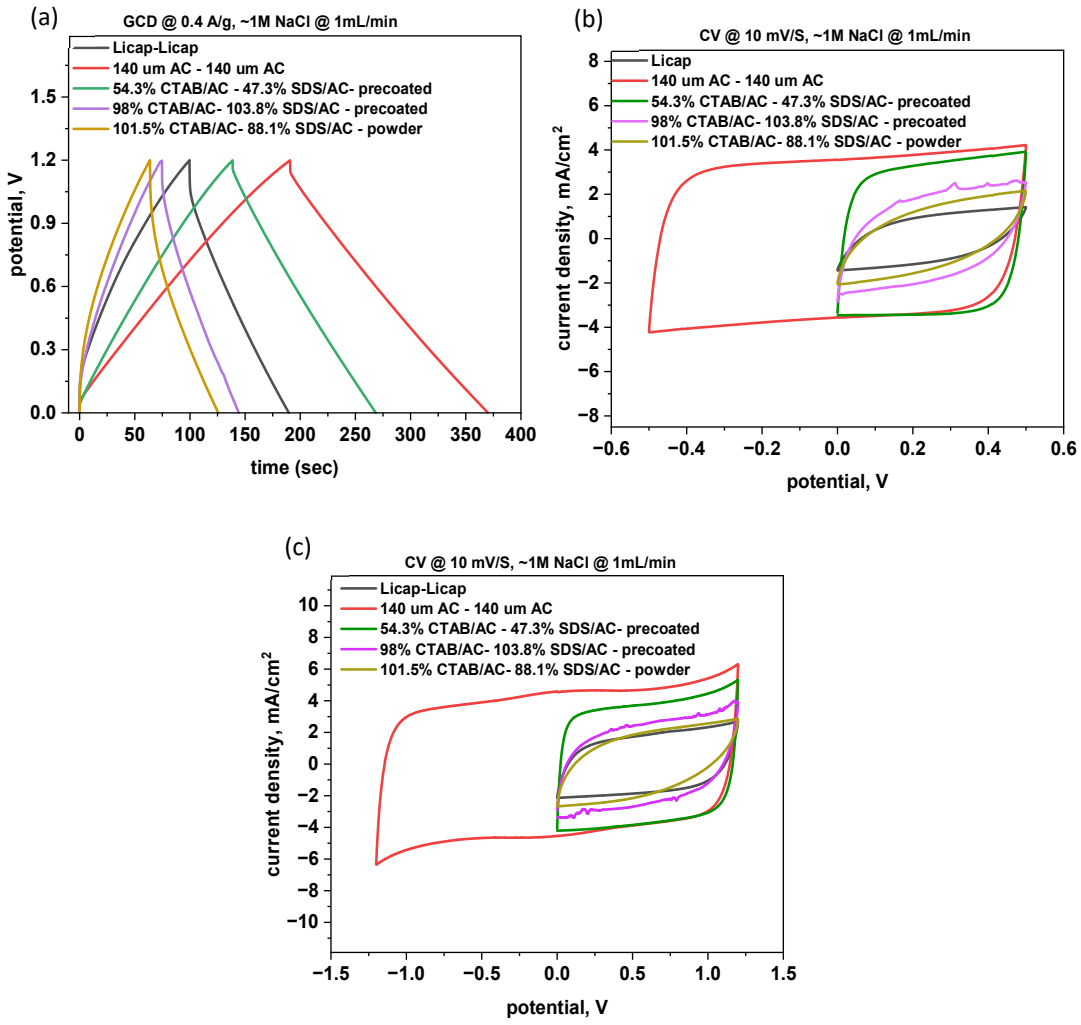

Figure 2-11: Electrochemical characterization of AC/AC, 54.3% CTAB/AC – 47.3% SDS/AC -precoated, 98% CTAB/AC – 103.8% SDS/AC - precoated, 101.5% CTAB/AC – 88.1% SDS/AC -powder in 1.0 M NaCl in constant flow condition (flow rate 1.00 mL/min) by (a) Galvanostatic Charge-Discharge at 0.40 A/g, (b) Cyclic Voltammetry in the potential window of +0.00 V to +0.50 V (-0.50 V to +0.50 V for AC) at 10 mV/S, and (c) Cyclic Voltammetry in the potential window of +0.00 V to +1.20 V (-1.20 V to +1.20 V for AC) at 10 mV/s.

The CV in 1.0 M NaCl in the potential window of 0.0 V to +0.50 V and 0.0 V to +1.20 V, Figure 2-11(b) and Figure 2-11(c), shows a capacitive CV profile with no presence of redox peak. That indicates the capacitance of the AC, surfactant modified AC is dominated by the capacitive double layer formed inside the charged pores[45].

The CV and GCD curves for different electrode pairs are presented in Figures 2-11(a) and 2-11(b). From the CV, capacitance of the electrode was calculated and the result are tabulated in Table 2-4. It is observed that the areal and mass-specific capacitance follow the descending order: AC-AC > 54.3% CTAB/AC-47.3% SDS/AC-precoated > 98.0% CTAB/AC-103.8% SDS/AC-precoated > 101.5% CTAB/AC-88.1% SDS/AC-powder. This trend correlates with the results for BET-specific surface area results of the materials. Surfactant impregnation induces pore blocking in AC and, as a consequence, reduces the surface area of the materials and thereby reduces the electrochemical capacitance.

At the start of the discharge cycle in GCD, Figure 2-11(a), a voltage drop, V_{drop} (=iR), was observed due to ion diffusion, electrode, and internal solution resistance [46]. The voltage drop observed for Licap-Licap, AC-AC, 54.3% CTAB/AC – 47.3% SDS/AC-precoated, 98.0% CTAB/AC – 103.8% SDS/AC-precoated and 101.5% CTAB/AC – 88.1% SDS/AC-powder is 106 mV, 57 mV, 44 mV, 98.0 mV and 120 mV, respectively. The reduction of the pore volume due to surfactant impregnation on AC could cause an increase of ion diffusion resistance.

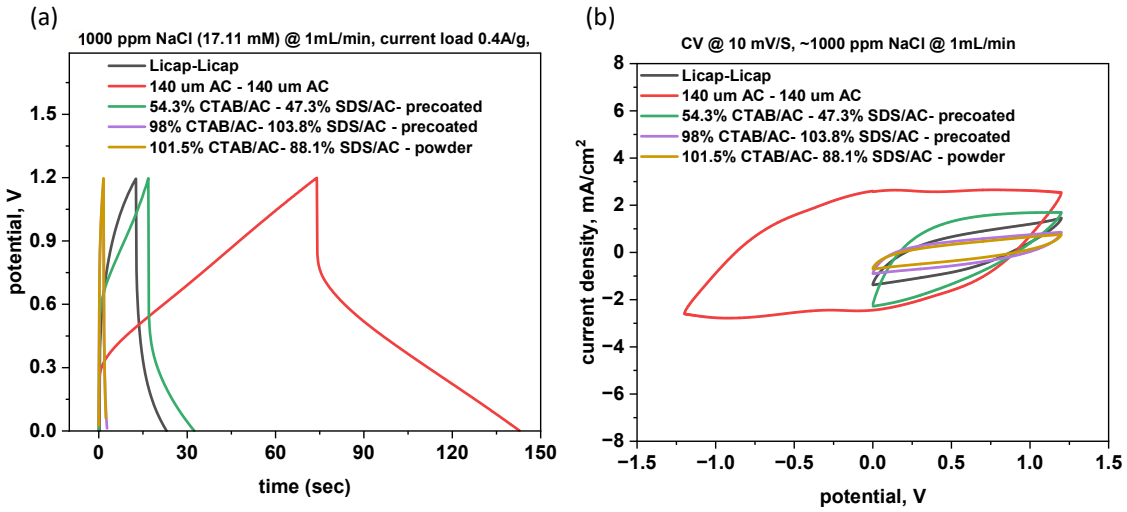

Figure 2-12: Electrochemical characterization in of Licap-Licap, AC-AC, 54.3% CTAB/AC-47.3% SDS/AC-precoated electrode, 98% CTAB/AC-103.8% SDS/AC-precoated electrode and 101.5% CTAB/AC-88.1% SDS/AC-powder in 1000 ppm NaCl in constant flow condition (flow rate 1 mL/min) by (a) Galvanostatic Charge-Discharge at 0.4 A/g, and (b) Cyclic Voltammetry in the potential window of +0.00 V to +1.20 V (-1.20 V to +1.20 V for AC) at 10 mV/s.

Table 2-5: Capacitance of the electrodes calculated from GCD in 1000 ppm NaCl.

Cell	Mass specific capacitance of an electrode, $F/g_{AC\ film}$
Licap- Licap	10.7
Pristine AC-Pristine AC (140 um)	70.4
54.3% CTAB/AC-47.3% SDS/AC -precoated	22.1
98.0% CTAB/AC-103.8% SDS/AC -precoated	1.8
101.5% CTAB/AC-88.1% SDS/AC -powder	1.1

Since the CDI experiments was done on 17.11 mM (1000 ppm) NaCl, so the same solution has been used to do electrochemical characterization to investigate the electrode response in the potential window from 0.0 V to +1.20 V and electrode capacitance in the low salt concentration. The mass-specific capacitance of the electrode was calculated from GCD in 1000 ppm, presented in Figure 2-12(a) and Table 2-5. The order of mass specific capacitance in 1000 ppm NaCl is: AC-AC > 54.3% CTAB/AC – 47.3% SDS/AC -precoated> 98.0% CTAB/AC – 103.8% SDS/AC -precoated > 101.5% CTAB/AC – 88.1% SDS/AC -powdered. For all electrodes, the capacitance in low salt concentration is lower compared to the capacitance in 1.0 M NaCl. This is well understood from the relationship of concentration dependent electrical double layer formation[47]. The Debye length is inversely proportional to the square root of the ionic strength. The Debye length for 1.0 M NaCl solution is 0.3 nm and Debye length for 1000 ppm (17.11 mM) NaCl solution is 2.3 nm. That suggest a loosely packed electrical double layer in the low ion concentration, leading to lower specific capacitance[48].

The voltage drop observed in GCD in 1000 ppm for Licap-Licap, AC-AC, 54.3% CTAB/AC – 47.3% SDS/AC-precoated, 98.0% CTAB/AC – 103.8% SDS/AC-precoated, 101.5% CTAB/AC – 88.1% SDS/AC-powder is 434.2 mV, 361.1 mV, 639.2 mV, 736.4 mV and 721.8 mV, respectively. The voltage drop in 1000 ppm NaCl is higher than that in 1.0 M NaCl. The reason could be due to increased resistance as the ionic strength is decreased[47]. For the same reason, a distortion in CV profile is observed, presented in Figure 2-12(b).

2.12-CDI experiment

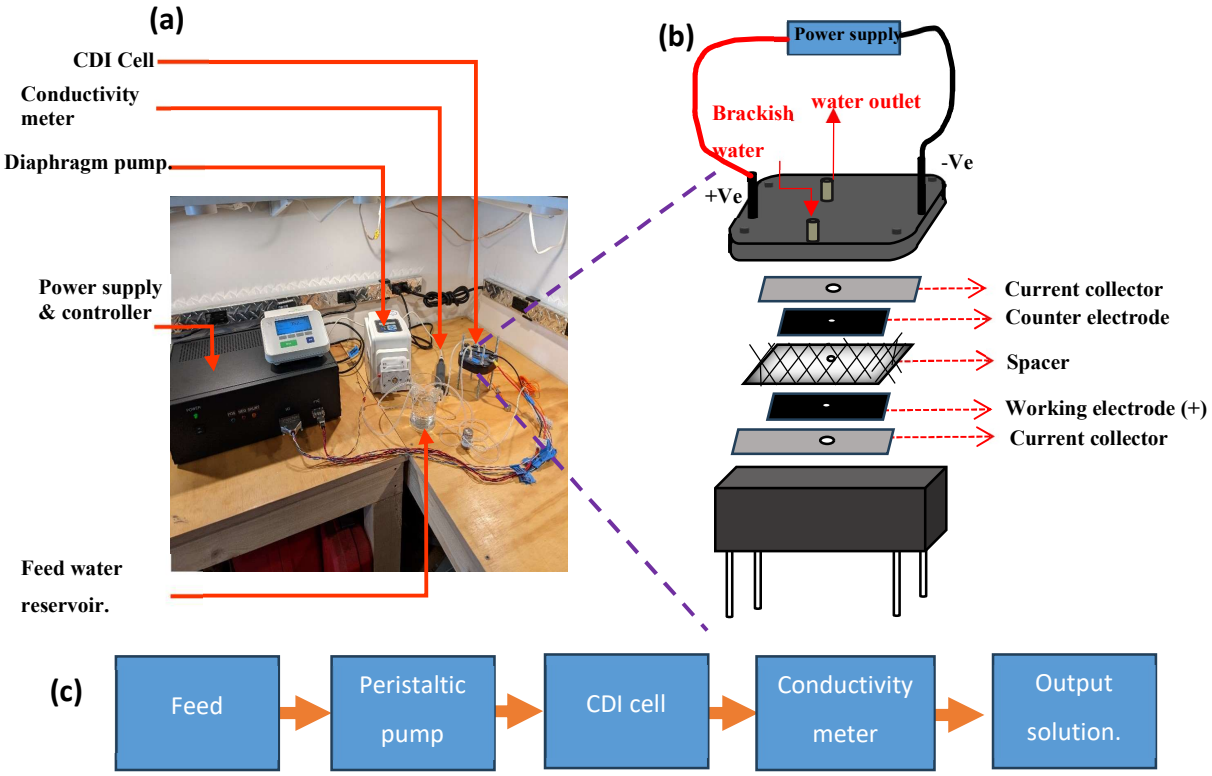

Figure 2-13: CDI (a) experimental setup, (b) cell setup, and (c) Flow diagram of CDI testing system.

The CDI system consisted of a home-built CDI cell, a peristaltic pump to continuously pump the solution at a constant flow rate and a DC power supply (Figure 2-13(a)). During assembly of the CDI cell, the CTAB/AC was used as working electrode and SDS/AC was used as counter electrode (Figure 2-13(b)). The conductivity of NaCl solution was continuously measured by a conductivity probe (Mettler Toledo Inlab 751). Before running CDI tests, the conductivity meter was calibrated by 1413 uS/cm conductivity standard solution. A single-pass mode CDI was conducted to measure the CDI performance in different CDI modes. Starting with the 50 cycles NCDI, followed by 50 cycles iCDI, and 50 cycles Bipolar CDI, and finally 50 cycles Bipolar+Shunt CDI. For each of the individual experiment 3000 mL NaCl solution with initial concentration of 1000 ppm was cycled in a single pass mode at a constant flow rate of ~1.00 mL/min^{-1} unless specified

The performance of the CDI is measured by the following metrics derived from the experimental results:

Salt adsorption capacity (SAC), $\Gamma(mg_{NaCl}/g_{AC\text{-}film}) = \frac{Mw\ X \int (Ci-Co)\ X\ \emptyset\ X\ dt}{Me}$…… (2.9)

Charge efficiency, CE (%) = $\frac{\frac{\Gamma\ X\ Me}{M_w}}{\frac{q}{96485}}$…… (2.10)

Energy consumption per ion, $E_{con} = \frac{V\ X\ q}{\frac{\Gamma\ X\ m}{M_w}}$…… (2.11)

Stability = $\frac{\Gamma nth}{\Gamma max}\ X\ 100$……. (2.12)

q = total charge transferred during charging excluding the leak charge (C)

V = Applied potential (V)

M_w = Molecular weight of NaCl = 58.44 g/mol

m = AC film mass before surfactant modification (g)

M_e = total mass of AC films before surfactant modification (g)

C_i = initial concentration of NaCl was determined by averaging concentration for initial 10 sec and final 10 sec (ppm).

C_o= Output concentration of NaCl over time (ppm)

dt= Duration of charging (min)

ø = flow rate (mL/min)

2.12.a- NCDI-normal CDI

A constant flow rate of ~1.00 mL/min was maintained during the CDI cycles. To adsorb ions, a voltage bias of +1.20 V was applied for 20 minutes, and then a 0.00 V (shunt) was applied for 20 minutes to desorb ions. During the CDI, the concentration of 1000 ppm salt solution was reduced due to ion adsorption in the charging process. The adsorbed ions got desorbed during the shunt, causing an increase of salt concentration in the solution. The charging step followed by the discharging step completes a full CDI cycle, as shown in Figure 2-14(a)

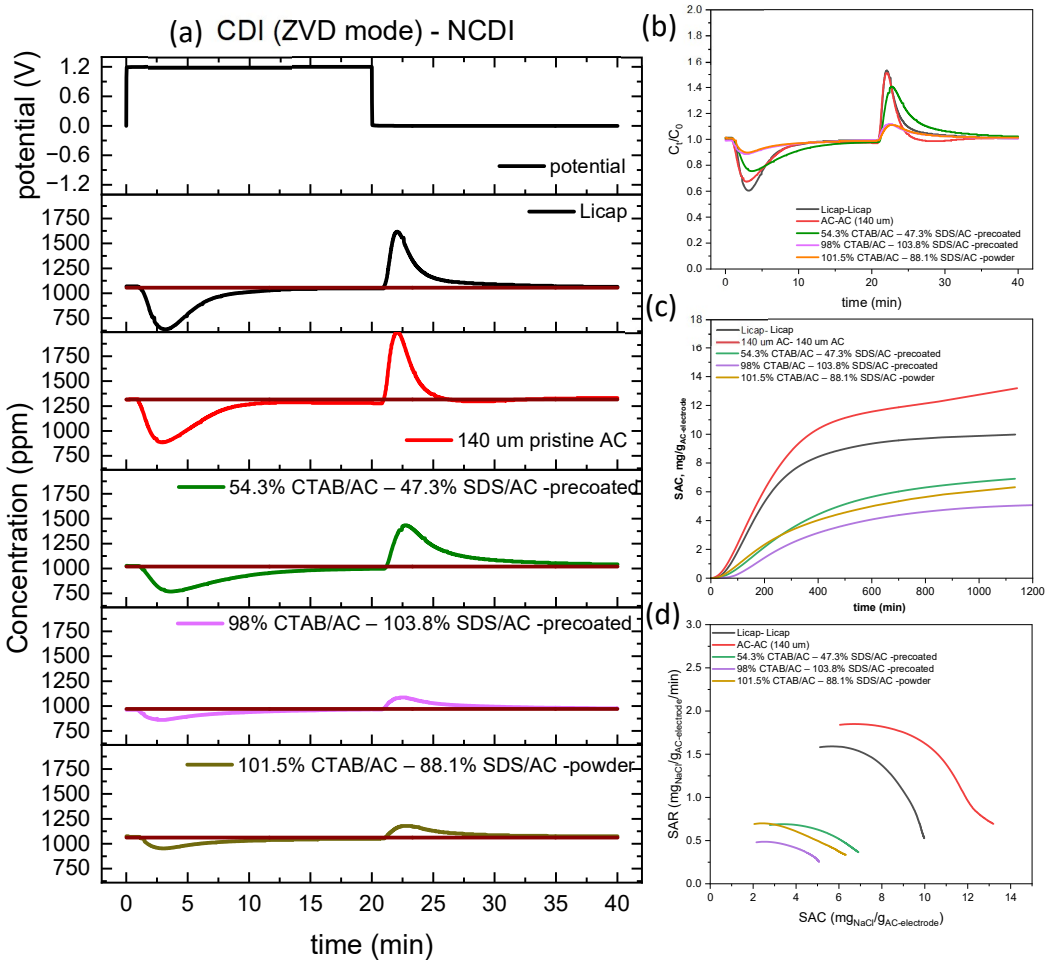

Figure 2-14: The electro-sorption performance analysis based on the 5th CDI cycle for the CDI cell consisting of free-standing Licap- Licap, pristine AC-AC, 54.3% CTAB/AC – 47.3% SDS/AC-precoated, 98% CTAB/AC – 103.8% SDS/AC-precoated, 101.5% CTAB/AC – 88.1% SDS/AC-powder: (a) CDI concentration profile vs time for asymmetric and symmetric cell setup, (b) peak desalination (%), (c) salt absorption capacity (SAC) during the 5th cycle, and (d) salt adsorption rate (SAR) vs SAC (Kim-yoon plot) for the 5th cycle.

Due to the high surface area and high active meso- and micro-pores of AC, the ion adsorption kinetics is faster, and the ion adsorption capacity is also high. However, as surfactant loading onto the AC increases, some of these active pores become blocked, reducing the material's active pore volume and specific surface area (SSA). Consequently, this leads to a decrease in both the salt adsorption kinetics and salt adsorption capacity. The order of salt adsorption rate (SAR) is. AC-AC > 54.3% CTAB/AC – 47.3% SDS/AC-precoated > 98.0% CTAB/AC – 103.8% SDS/AC -precoated > 101.5% CTAB/AC – 88.1% SDS/AC -powder.

Table 2-6:Peak desalination (%) at 1.0 mL/min for different electrode

Electrode	Peak desalination (%) at 5th CDI cycle
Licap-Licap	39.5
Pristine AC-Pristine AC (140 um)	32.7
54.3% CTAB/AC-47.3% SDS/AC -precoated	25.5
98.0% CTAB/AC-103.8% SDS/AC -precoated	10.7
101.5% CTAB/AC-88.1% SDS/AC -powder	10.2

The electrosorption performance of the initial 50 cycles CDI in NCDI mode are presented in Figures 2-15(a), and the average results charge efficiency, salt adsorption capacity, and energy consumptions are presented in Table 2-7. The salt adsorption capacity of AC-AC is ~2.6X higher

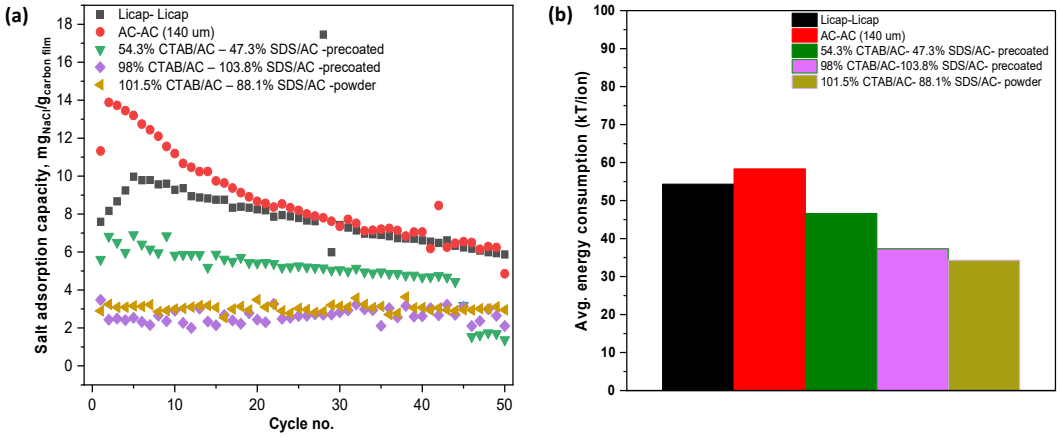

Figure 2-15: (a) Charge efficiency (%), and (b) average energy consumption (kT/ion) of free-standing Licap- Licap, AC-AC, 54.3% CTAB/AC- 47.3% SDS/AC-precoated electrodes, 98% CTAB/AC-103.8% SDS/AC-precoated electrodes, and 101.5% CTAB/AC – 88.1% SDS/AC electrodes.

than 101.5% CTAB/AC – 88.1% SDS/AC-powder and ~1.7X higher than 54.3% CTAB/AC – 47.3% SDS/AC-precoated. These results are similar to that observed from the specific capacity. It indicates that the pore volume of the active material plays a crucial role in salt adsorption.

The average charge efficiency of AC-AC electrode is 39.5%, whereas the charge efficiency for 54.3% CTAB/AC- 47.3% SDS-AC –precoated, 98.0% CTAB/AC- 103.8% SDS-AC – precoated, 101.5% CTAB/AC- 88.1% SDS-AC –powder is 49.3%, 62.8%, 68.2% (Table 2-7). This trend suggests that the charge efficiency increases with increased surfactant loading on AC, as it facilitates efficient repulsion of the co-ions without requiring additional charge from the

system. For this same reason, the energy consumption for 98.0% CTAB/AC- 103.8% SDS-AC – precoated and 101.5% CTAB/AC- 88.1% SDS-AC–powder is also low (Figure 2-15(b)).

Table 2-7: Electro-sorption performance- NCDI

Electrode	Avg. CE (%)	Avg. Energy consumption pre ion (kT/ion) @296 K	Avg. SAC ($mg_{NaCl}/g_{AC\ film}$)	SAC retention (%) after 40^{th} cycle
Licap-Licap	42.8	54.3	7.71	66.3
Pristine AC-Pristine AC (140 um thick)	39.5	58.4	8.78	50.8
54.3% CTAB/AC-47.3% SDS/AC - precoated	49.3	46.6	5.00	67.7
98.0% CTAB/AC-103.8% SDS/AC - precoated	62.8	37.3	2.63	75.3
101.5% CTAB/AC-88.1% SDS/AC - powder	68.2	34.3	3.05	84.6

The differences in SAC and CE for 98.0% CTAB/AC- 103.8% SDS-AC–precoated and 101.5% CTAB/AC- 88.1% SDS-AC–powder could be due to the difference in ion diffusion pathways for the tortuosity in electrode. Since the surfactant modifications on 98.0% CTAB/AC-103.8% SDS-AC–precoated was done on the pre-coated AC electrodes, that makes the ion diffusion pathways more tortuous than the complete surfactant-impregnated powder material (101.5% CTAB/AC- 88.1% SDS-AC –powder).

The 98.0% CTAB/AC-103.8% SDS-AC–precoated and 101.5% CTAB/AC- 88.1% SDS-AC–powder electrode showed the highest stability. It retains ~80% salt adsorption capacity up to the 40^{th} cycle. In contrast, the AC-AC electrodes only retained 50.8% of their salt adsorption capacity after 40 cycles, while the 54.4% CTAB/AC-42.9% SDS-AC–precoated electrodes retained 67.7%. The decline in stability in pristine AC film (AC-AC) and incomplete surfactant-modified film (54.4% CTAB/AC- 42.9% SDS-AC–precoated) is primarily attributed to carbon oxidation in the anode during the charging steps [49] .

Effect of Flow rate on peak desalination:

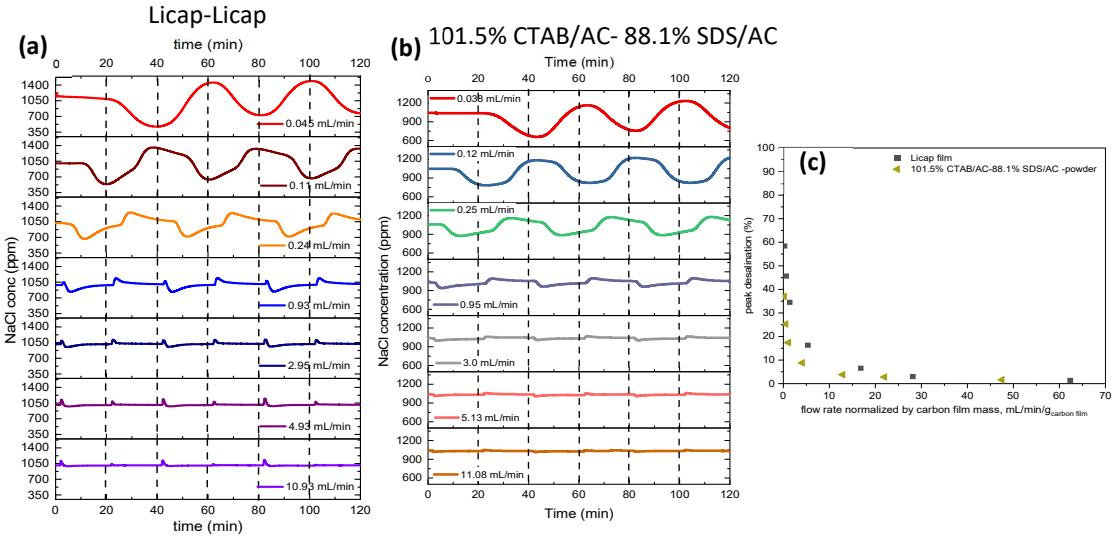

Figure 2-16: CDI dependence on the solution flow rates: (a) concentration profile for Licap-Licap, (b) concentration profile for 101.5% CTAB/AC- 88.1% SDS/AC, and (c) the peak desalination comparison between the electrodes.

The peak desalination decreases with the increase of the flow rate. In Figure 2-16(c), the flow rate is normalized by the carbon film mass (mL/min/$g_{AC\ film}$). At the high flow rate, the contact time between the electrodes and the low concentration solution was short. As a result, the ions did not get into the AC pores, leading to the low adsorption and low peak desalination. At the low flow rate, the peak desalination was >20%, but it took longer time to reach the equilibrium, as shown in Figures 2-16(a) and 2-16(b). Overall, 1.0 mL/min was the optimum flow rate in which the concentration reached equilibrium during each charging and discharging steps and the peak desalination was >10%. The Licap-Licap cell showed a higher peak desalination compared to 101.8% CTAB/AC-88.1% SDS/AC, likely because of the presence of a larger pore volume in the AC than the surfactant-modified samples.

2.12.b- iCDI- Inverted CDI

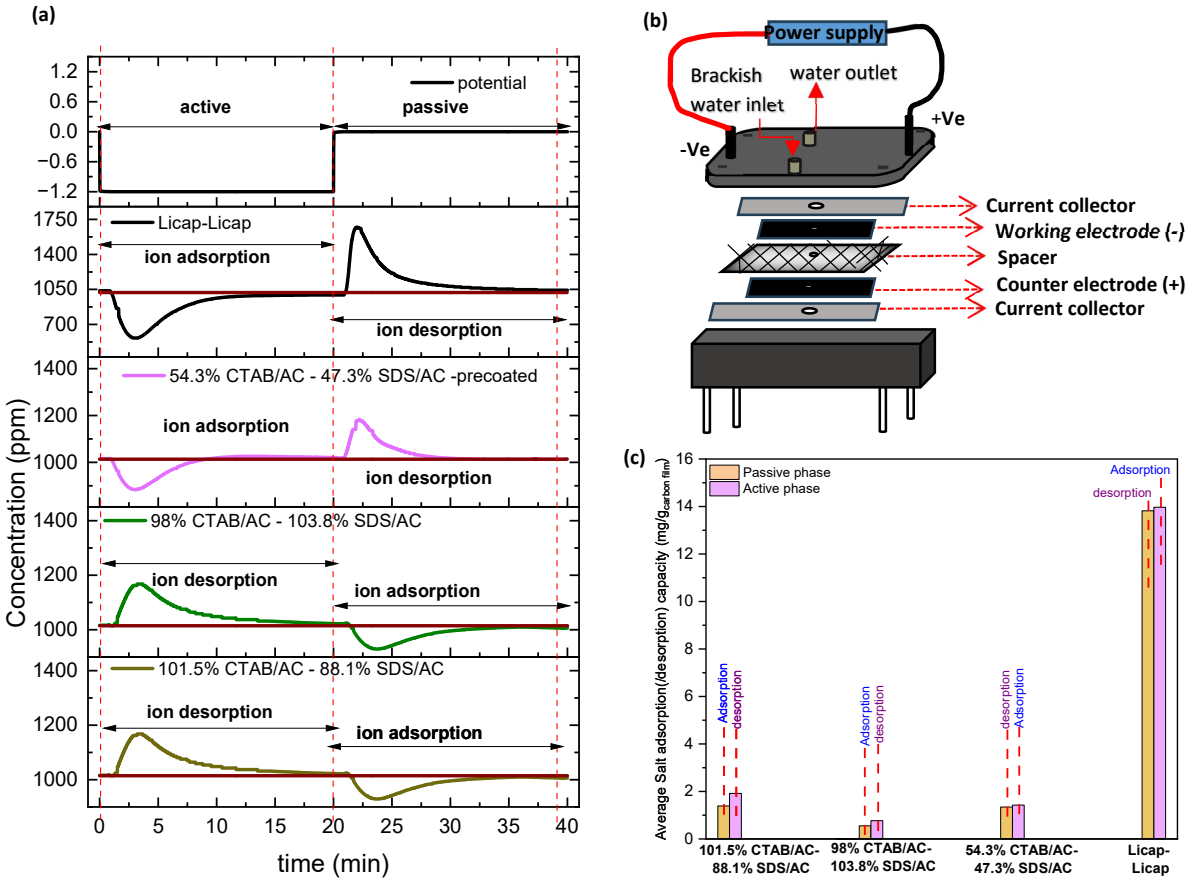

Figure 2-17: (a) The 5th cycle of inverted CDI concentration profile vs time of Licap-Licap, 54.3% CTAB/AC–47.3% SDS/AC-precoated, 98% CTAB/AC–103.8% SDS/AC-precoated, 101.5% CTAB/AC–88.1% SDS/AC-powder in 1000 ppm NaCl at a constant flowing rate of 1.0 mL/min), (b) the cell setup for inverted CDI, and (c) the average salt adsorption (/desorption) capacity during the active (-1.20 V) and passive (0.00 V) phase.

A cell is assembled as shown in Figure 2-17(b), where the working electrode is SDS/AC and counter electrode is CTAB/AC. A constant flow rate of ~1.00 mL/min was maintained during the i-CDI cycles. In an inverted CDI cycle, -1.20 V is applied for 20 minutes to desorb ions by electrostatic repulsion, and this phase is called the active phase. In the passive phase, the cell is shunted for 20 minutes, and due to the electrostatic attraction between the surfactant functional groups and ions from the bulk solution, the ions get adsorbed to the electrode [50]. By an active phase followed by a passive phase completes an i-CDI cycle, as shown in the Figure 2-17(a). The concentration vs. time profile for 98.0% CTAB/AC-103.8% SDS/AC-precoated and 101.5%

CTAB/AC-88.1% SDS/AC-powder cell in i-CDI mode presented in Figure 2-17(a) is similar to the profile presented in literature for i-CDI[43, 51]. In the pristine free-standing Licap-Licap and 54.3% CTAB/AC-47.3% SDS/AC, the concentration profile in i-CDI mode is similar to the normal CDI in Figure 2-14(a) due to the lack of charged groups at the surface. During the active phase (-1.20V) , the ions get adsorbed onto the electrode, and during the passive phase, the ions get desorbed[51].

Table 2-8: i-CDI performance

Cell	Avg. SAC (mg_{NaCl}/g_{ACfilm})	Avg. SDC (mg_{NaCl}/g_{ACfilm})
Licap-Licap	13.97	13.82
54.3% CTAB/AC-47.3% SDS/AC-precoated	1.42	1.34
98.0% CTAB/AC-103.8% SDS/AC-precoated	0.55	0.76
101.5% CTAB/AC-88.1% SDS/AC-powder	1.39	1.91

In Licap-Licap and 54.3% CTAB/AC-47.3% SDS/AC during the active phase, the salt adsorption capacity (SAC) was 13.97 mg_{NaCl}/g_{ACfilm} and 1.42 mg_{NaCl}/g_{Acfilm}, respectively and the salt desorption capacity (SDC) was 13.82 mg_{NaCl}/g_{ACfilm} and 1.34 mg_{NaCl}/g_{Acfilm}, respectively. On the contrary, the 98.0% CTAB/AC-103.8% SDS/AC-precoated and 101.5% CTAB/AC-88.1% SDS/AC-powder showed the SAC of 0.55 mg_{NaCl}/g_{ACfilm} and 1.39 mg_{NaCl}/g_{Acfilm}, respectively during the passive phase and the SDC of 0.76 mg_{NaCl}/g_{ACfilm} and 1.91 mg_{NaCl}/g_{Acfilm}, respectively, during the active phase.

Comparison of i-CDI and NCDI

A significant difference in the CDI cycle was observed in the NCDI and iCDI (Figure 2-18). In the Licap-Licap symmetric cell, the electrodes adsorbed ions regardless of positive or negative voltage bias but the type of ion (cation or anion) adsorbed on a specific electrode depended on the polarity of the voltage bias. However, the ionic surfactant-modified AC

electrodes showed very different behavior. The modified electrode became charge-selective and efficiently repeled the adsorption of co-ions. For that reason, the electrode pair consisting of

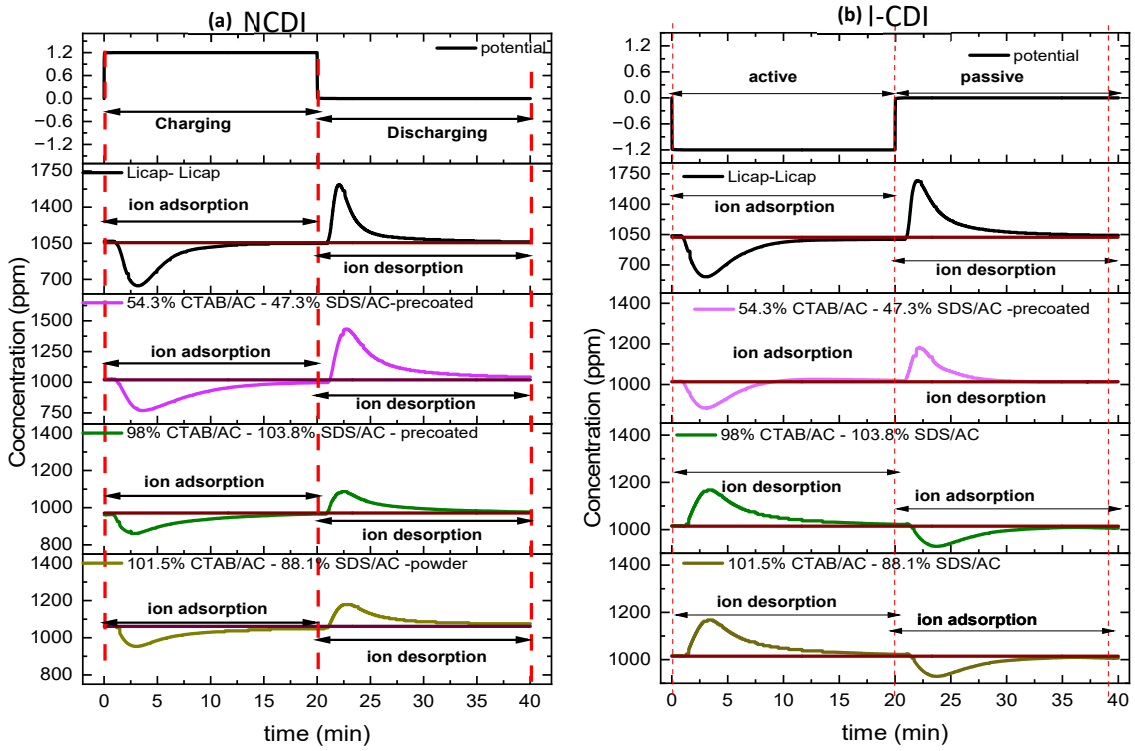

Figure 2-18: The comparison of the profiles of slat concentration vs. time of Licap-Licap, 54.3% CTAB/AC–47.3%SDS/AC, 98% CTAB/AC- 103.8% SDS/AC-precoated, 101.5% CTAB/AC-88.1% SDS/AC-powder in (a) N-CDI mode, and (b) i-CDI mode.

saturated surfactant impregnation (i.e., 98.0% CTAB/AC-103.8% SDS/AC and 101.5% CTAB-88.1% SDS/AC) showed the inverted ion concentration vs. time profile in i-CDI compared to NCDI. This behavior is explained in detail with the mechanism of ion adsorption.

Mechanism of ion adsorption in i-CDI

The surfactant impregnation on AC can function as a charge-selective membrane. The counter ions from the electrolyte can selectively bind with surfactant molecules adsorbed to the electrode due to electrostatic attraction between the surface-charged group and the ions in the solution (Figure 2-19(a)). These ions adsorbed onto the electrode during shunt (or without applying any bias), as seen for the surfactant-saturated electrodes (98.0% CTAB/AC- 103.8% SDS/AC and 101.5% CTAB-88.1% SDS/AC) in Figure 2-19(a). During discharge, an external bias was applied

to the electrodes, which was opposite to the polarity of the electrode surface charge. This created an electrostatic repulsion between the electrode and adsorbed ions and caused ion desorption from

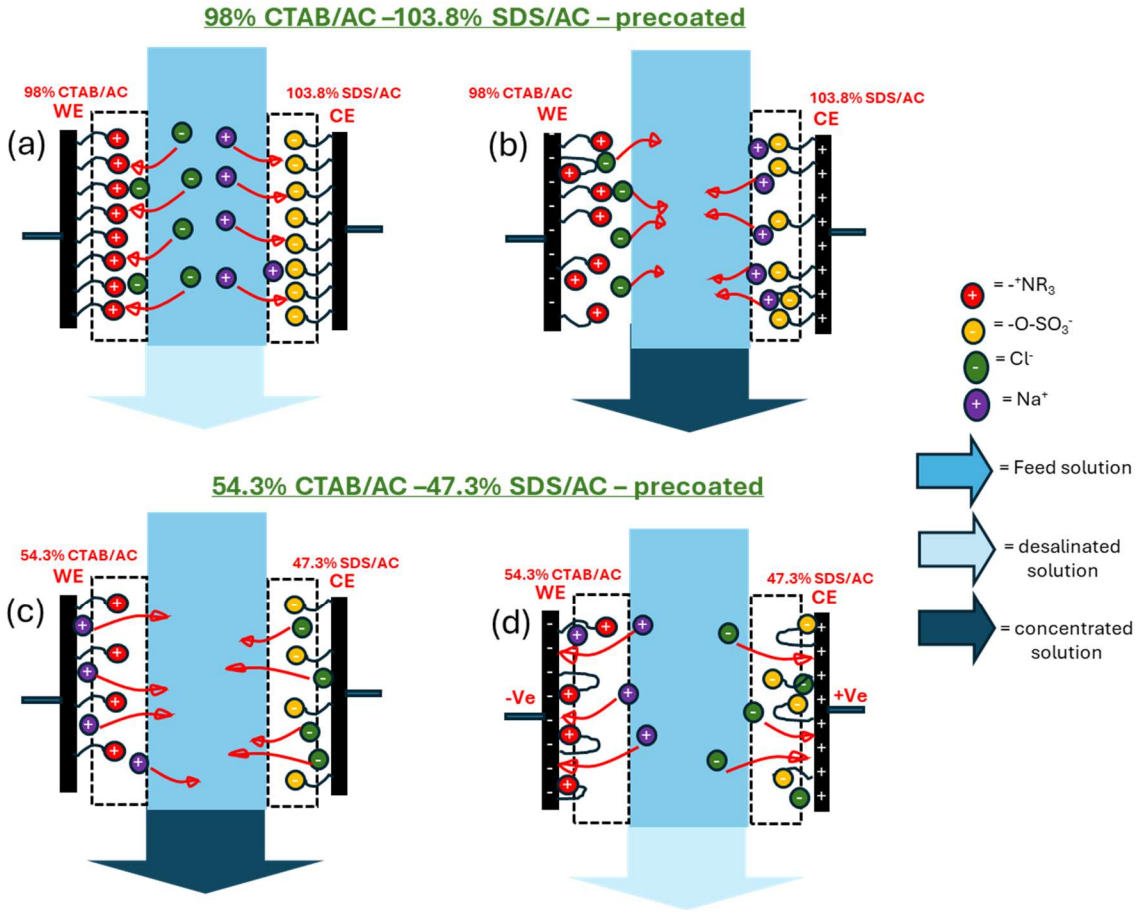

Figure 2-19: The mechanism of ion-adsorption-desorption to 98% CTAB/AC-103.8% SDS/AC (a) during shunt, and (b) during -1.20 V, and to 54.3% CTAB/AC-47.3% SDS/AC (c) during shunt, and (d) during -1.20 V in i-CDI cycle.

the electrodes, as depicted in Figure 2-19(b). As the hydrophobic tail of the SDS is ~1.9 nm and CTAB is ~2.4 nm, the electric field to the surfactant is weaker compared to the interaction between surfactant molecules and the electrode surface. In 54.3% CTAB/AC-47.3% SDS/AC, the ion adsorption to the electrode is dominated by the electrostatic attraction due to applied bias over electrostatic repulsion by the charge of surface functionalized surfactants since a substantial portion of the surface was exposed. Thus the profile of concentration vs. time is altered during the i-CDI process with the incomplete surface impregnation.

2.12.c- Bipolar CDI (Reverse voltage Discharge mode)

The cell configuration was similar to Figure 2-13(b), where the positive electrode was CTAB/AC and the negative electrode was SDS/AC. The 1000 ppm NaCl solution was passed through the cell at a constant flow rate of 1.00 mL/min during the Bipolar-CDI cycles. During each cycle, a +1.20 V bias was applied for 20 minutes to adsorb counter ions electrostatically, and then a -1.20 V bias was applied for 20 minutes to desorb ions by electrostatic repulsion to complete a full bipolar-CDI cycle. The concentration vs time profiles of the cells consisting of 98.0% CTAB/AC-103.8% SDS/AC-precoated, 101.5% CTAB/AC-88.1% SDS/AC-powder, and 54.3% CTAB/AC-47.3% SDS/AC-precoated electrodes in Bipolar-CDI are presented in Figure 2-20. In the 54.3% CTAB/AC-47.3% SDS/AC cell, there was a co-ion expulsion during the charging steps before new ion adsorption (Figure 2-20(a)). This ion expulsion suggests co-ion adsorption during the previous discharge cycle. The reason for this behavior is that the incomplete impregnation of surfactant on AC left some area of unmodified AC exposed to the electrolyte, which can interact with the opposite ions during discharging.In the cells of 98.0% CTAB/AC-103.8% SDS/AC-precoated electrodes and 101.5% CTAB/AC-88.1% SDS/AC-powder electrodes, there was no co-

ion expulsion since the AC surface was fully covered by the surfactants which electrostatically repelled the co-ions (Figure 2-20).

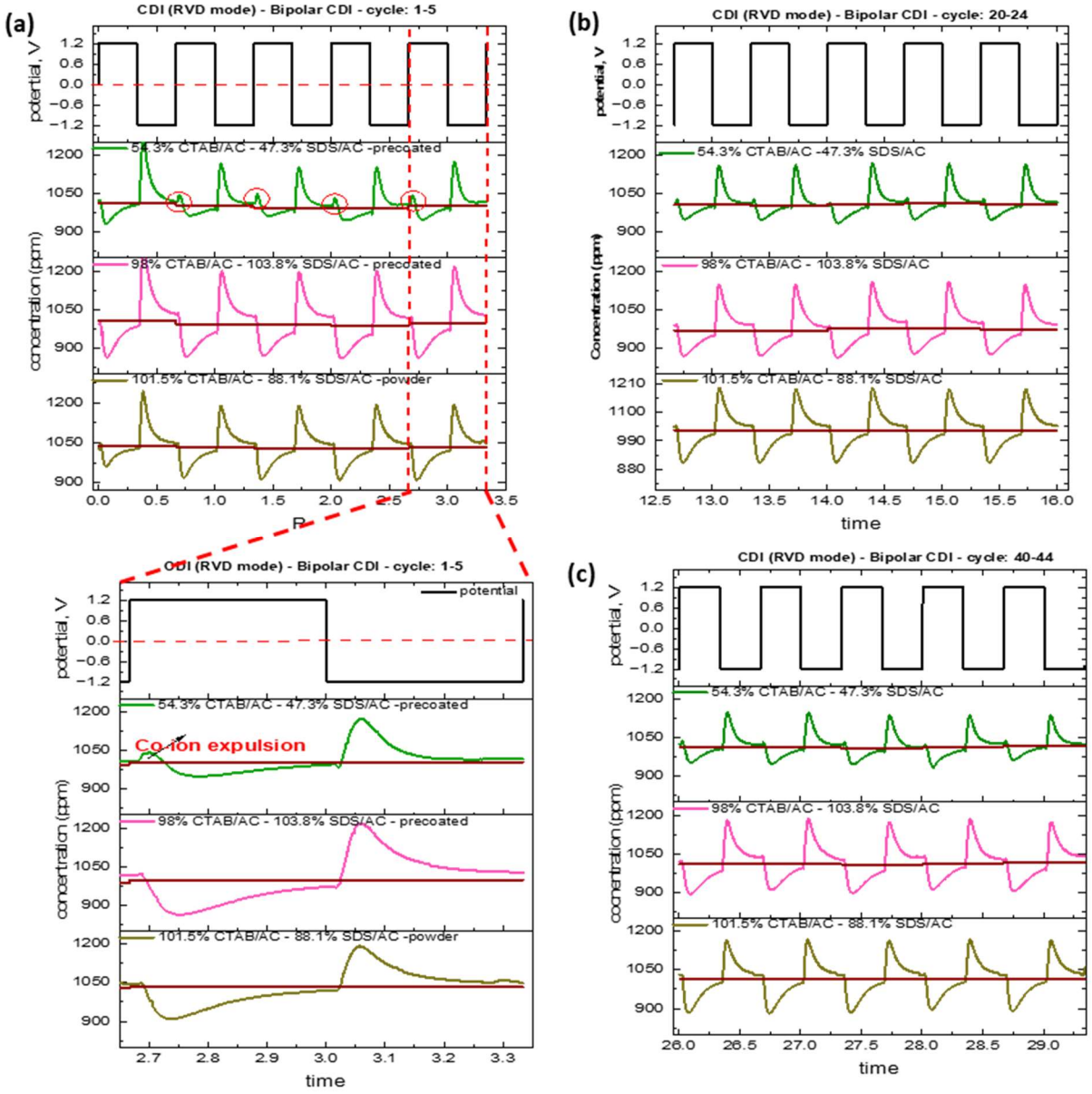

Figure 2-20: The concentration vs time profile during the Bipolar CDI in (a) 1st to 5th cycles (inset enlarged view of the 5th CDI cycle), (b) 20th to 24th cycles, and (c) 40th to 44th cycles.

Due to this co-ion effect, the salt adsorption capacity of electrodes with incomplete surfactant modification (i.e., 54.3% CTAB/AC-47.3% SDS/AC-precoated) was lower compared to those with complete surfactant modification (98.0% CTAB/AC-103.8% SDS/AC-precoated and 101.5% CTAB/AC-88.1% SDS/AC-powder) (Figure 2-21).

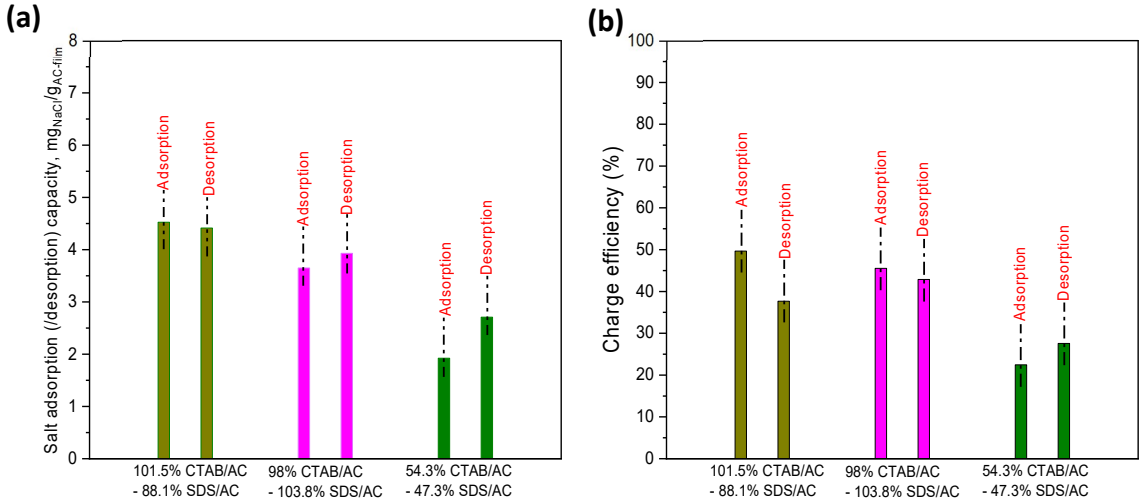

Figure 2-21: Electro sorption performance of 101.5% CTAB/AC-88.1% SDS/AC, 98% CTAB/AC-103.8% SDS/AC and 54.3% CTAB/AC-47.3% SDS/AC: (a) salt adsorption (/desorption) capacity and (b) charge efficiency.

Comparison of NCDI and Bipolar CDI:

An enhancement of performance in terms of salt adsorption capacity for cells with the complete surfactant modified electrodes (98.0% CTAB/AC- 103.8% SDS/AC and 101.5%

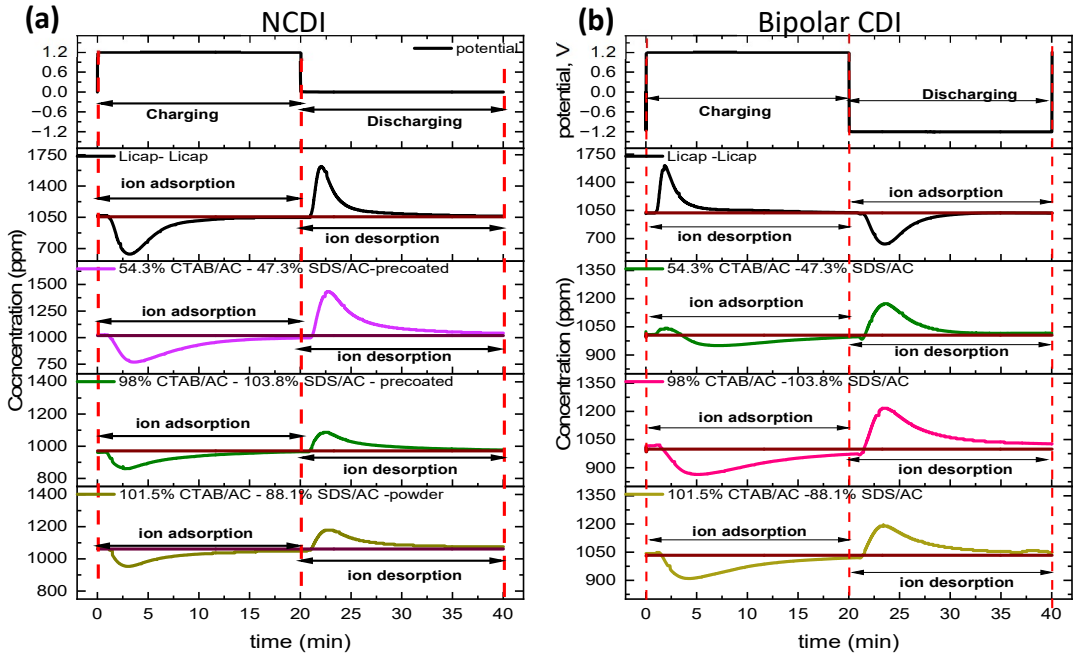

Figure 2-22: A comparison of the concentration vs time profiles of Licap-Licap, 54.3% CTAB/AC–47.3%SDS/AC, 98% CTAB/AC-103.8% SDS/AC and 101.5% CTAB/AC-88.1% SDS/AC in (a) N-CDI mode, and (b) Bipolar-CDI mode.

CTAB/AC-88.1% SDS/AC) was observed for bipolar mode CDI compared to NCDI, as shown in Table 2-9. The possible reason is the efficient removal of ions from the electrode by strong electrostatic repulsion generated from the -1.20 V during the bipolar CDI cycle. That caused a more active pore in complete surfactant-modified activated carbon to store ions and boost the salt adsorption capacity. However, due to the enhanced co-ion expulsion in incomplete modified electrodes (54.3% CTAB/AC -47.3% SDS/AC), the salt adsorption capacity in bipolar mode is reduced (Figure 2-22). For non-surfactant modified Licap-Licap cells, a flipping concentration behavior in bipolar CDI compared to NCDI in Figure 2-22 demonstrates the failure of the CDI cycle for this electrode.

Table 2-9: Comparison of salt adsorption capacity

Cell	NCDI	Bipolar CDI
54.3% CTAB/AC – 47.3% SDS/AC	5.00 $mg_{NaCl}/g_{AC\ film}$	1.92 $mg_{NaCl}/g_{AC\ film}$
98.0% CTAB/AC – 103.8% SDS/AC	2.63 $mg_{NaCl}/g_{AC\ film}$	3.64 $mg_{NaCl}/g_{AC\ film}$
101.5% CTAB/AC – 88.1% SDS/AC	3.05 $mg_{NaCl}/g_{AC\ film}$	4.52 $mg_{NaCl}/g_{AC\ film}$

Bipolar CDI profile for pristine AC (AC-AC & Licap-Licap)

In Figure 2-22(b), it was noted that the conductivity profile of a cell composed of Licap-Licap electrodes demonstrated an abnormal behavior in the concentration vs. time profiles in the biopolar CDI mode, which showed that the electrodes desorbed ions during charging and absorbed ions during discharging. The symmetric cell consisting of pristine AC-AC electrode pairs (Figure 2-23) showed the similar behavior. To understand this abnormality, a further troubleshooting analysis was done by adding a reference electrode to make it a three-electrode setup.

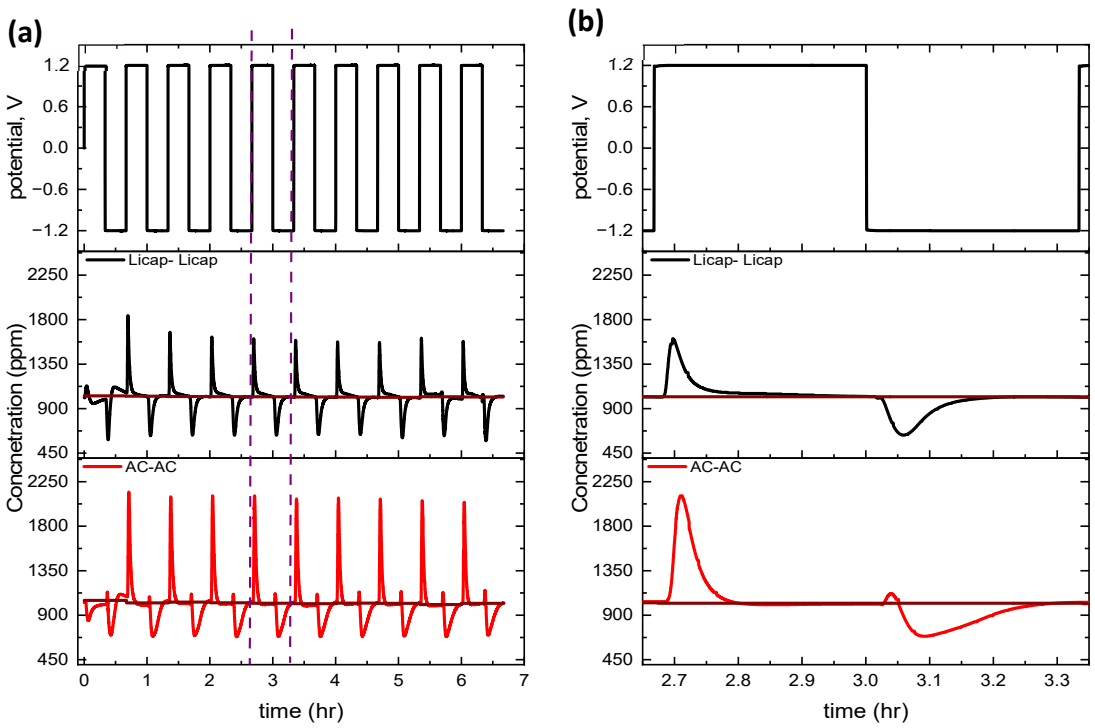

Figure 2-23 The voltage waveform and concentration-time profiles in Bipolar mode CDI for AC-AC and Licap-Licap in (a) 1st-10th CDI cycles, and (b) the 5th CDI cycle.

Troubleshooting:

To find out the reason for the abnormal CDI behavior in non-surfactant modified cells (Licap-Licap and AC-AC), a reference electrode was added before the CDI cell to measure the true electrode potential of the two electrodes in the CDI cell when the bipolar CDI voltage waveform was applied, as depicted in Figure 2-24(a). A T-connector was connected at the inlet of the CDI cell to establish the electrolytic connection between the CDI electrodes and the reference electrode. An Ag/AgCl (1M KCl) was used as a reference electrode, which provided a constant electrode potential. Then, the CDI controller was connected to the cell. A Bipolar CDI cycle was applied (Figure 2-24(b)). The potential applied to the cell was measured using a digital multimeter (Amprobe AM-240) by connecting one probe to the CDI electrode and another probe to the reference electrode (Ag/AgCl (1.0 M KCl)). Then the observed potential value was converted to SHE by using the equation,

$$V_{SHE} = V + V_{Ag/AgCl\ (1M\ KCl)\ vs\ SHE} = V + 0.222 \quad V\ldots\ldots\ldots (2.13)$$

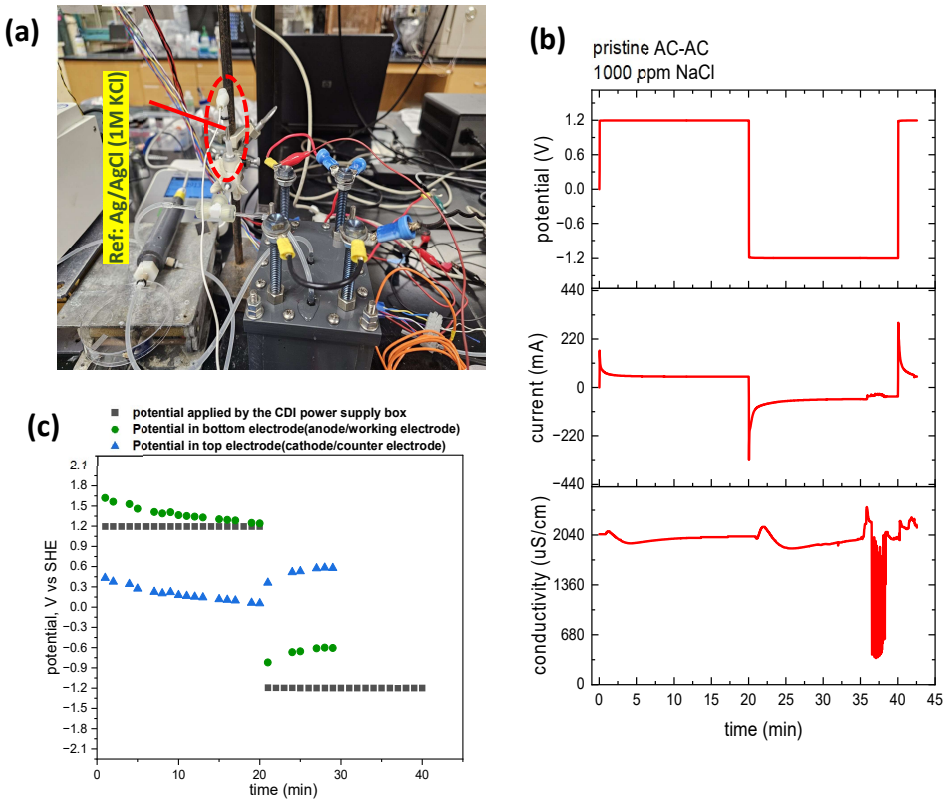

Figure 2-24: (a) The three-electrode cell setup for measuring the electrode potential of individual CDI electrodes, (b) the profiles of voltage, current and solution conductivity vs. time in a CDI cycle, and (c) the measured potential of the two CDI electrodes during the CDI cycle (the difference matches the applied voltage waveform).

Figure 2-24(c) presents the potential versus time curve of both CDI electrodes. From this, it can be seen that the CDI electrodes had floating electrode potentials though the difference between them was controlled to match the voltage waveform. Due to the floating potential, one of the CDI electrodes exhibited an initial potential higher than 1.6 V vs. SHE (green dots) when a +1.2 V voltage bias was applied. This high electrode potential can oxidize the AC surface to form oxygenated groups with abundant carboxylic acid groups (i.e. -COOH). At neutral pH values, -COOH deionized and present as $-COO^-$ groups. This led to a more negatively charged surface. As a result, after long CDI cycles with repeated application of +1.2 V, the CDI cells consisting of pristine AC-AC and Licap-Licap electrodes were no longer symmetric cells. They behaved similar to the asymmetric cell with surfactant-modified electrodes in bipolar CDI modes.

The above results raised a question whether the CDI abnormalty was an intrinsic property of the bipolar voltage waveform? It is noted that, throughout all the assembled cells, the CDI experiments were run in the following order: 50 cycles of NCDI (+1.20 V for 20 min followed by 0.0 V (shunt) for 20 min in each cycle), 50 cycles of I-CDI (-1.20 V for 20 min followed by 0.0 V (shunt) for 20 min in each cycle), and then 50 cycles of bipolar CDI (+1.20 V for 20 min followed by -1.20 V for 20 min in each cycle). As shown in Figure 2-18, the pristine Licap-Licap cell behaved the same in NCDI and I-CDI. Since it was essentially a symmetric cell, flipping the polarity of the cell voltage bias was not supposed to make any difference. The abnormality only occurred during the bioplar CDI sequences when the cell has already gone through 50 cycles of NCDI and 50 cycles of I-CDI. There was a possibility that the irreversible changes to the electrodes could have accumulated during those long cycles. To investigate the potential damage caused by the initial 50 cycles of NCDI, a new cell was assembled with two fresh Licap-Licap electrodes. The order of CDI cycling was 5 cycle bipolar CDI followed by 50-cycle NCDI, and then another 5 cycles bipolar CDI. A comparison between 5th bipolar CDI cycle before NCDI cycling and 5th bipolar CDI cycle after NCDI is presented in Figure 2-25.

The salt concentration-time profile during the initial bipolar CDI cycle showed a mixed co-ion desorption and counter-ion adsorption during the charging step at +1.2 V (Figure 2-25(a)). Similar phenomena were observed during the discharging step (at -1.2 V voltage bias) in the same bipolar CDI cycle. However, the conductivity profile in bipolar CDI cycle after 50 cycles of NCDI clearly different, as shown in Figure 2-25(b). This profile is consistent with previous results of Licap-Licap in Figure 2-22(b). Clearly, the 50 NCDI cycles convincingly caused the irreversible changes to the surface functional groups of the AC, likely through repeated oxidation to one of the electrodes that was subjected to upto +1.60 V vs SHE (as shown in Figure 2-24(c). This explains all the CDI results that were present earlier in this chapter. In the future, a better electronic controller that can control the electrode potentials accurately vs. a stable reference electrode may be able to avoid the electrode oxidation due to overshot potential while utilizing the maximal voltage window.

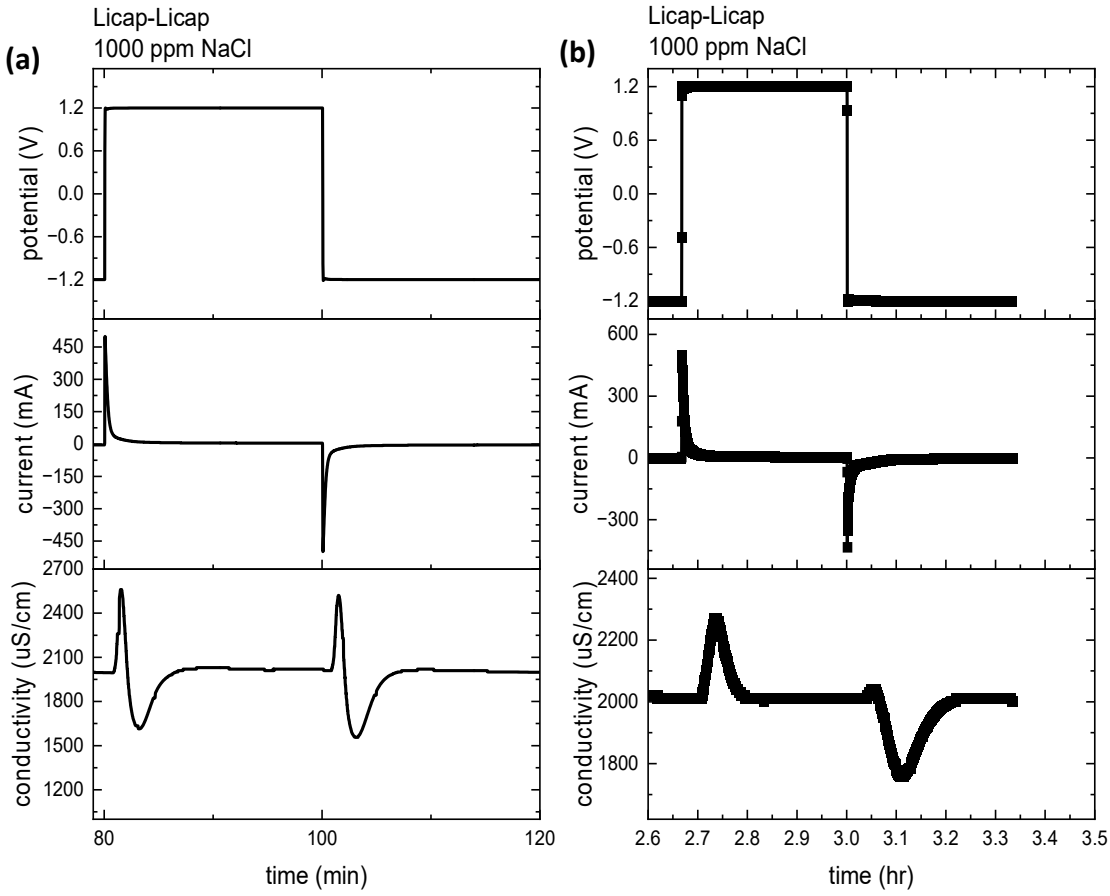

Figure 2-25: Bipolar mode CDI for Licap-Licap with (a) a pair of fresh electrodes, and (b) those after running 50 cycles of NCDI.

2.13 Conclusions

In summary, we have demonstrated an effective method to derivatize the AC surface with SDS and CTAB surfactnats, respectively, and developed the methods to control the surfactant loading and quantify their amount. The maximum CTAB adsorption capacity of AC was found 474.25 mg_{CTAB}/g_{AC} and SDS adsorption capacity on AC was found 492.35 mg_{SDS}/g_{AC}. The surfactants substantially block the micropores in the AC as reflected by the N_2 adsorption measurements while the major portion of the micropores is still accessible by the electrolyte as reflected by a smaller drop in the specific capacitance in electrochemical measurements. A complete surfactant covered saturated AC surface can function as a charge-selective ion exchange

membrane. That can selectively bind with counter-ions and repel the co-ions. Due to this effect, the CDI cells consisting of 101.5% CTAB/AC-88.1% SDS/AC on AC powders and 98.0% CTAB/AC-103.8 SDS/AC on precoated AC films showed a better stability, a higher charge efficiency and a lower energy consumption compared to the non-modified and incomplete modified electrodes in NCDI. However, the salt adsorption capacity is lower in the cell with completely surfactant-saturated electrodes because the partial blocking of available pores by the surfactants.

In I-CDI mode CDI cycle, the 54.3% CTAB/AC-47.3% SDS/AC, and Licap-Licap electrode shows the normal CDI behavior (adsorption during voltage application and desorption during shunt) instead of I-CDI behavior (adsorption during shunt and desorption during voltage application). This is due to the incomplete surface coverage With the complete surfactant coverage on the AC surface, such as 101.5% CTAB/AC-88.1% SDS/AC-powder & 98.0% CTAB/AC – 103.8 SDS/AC-precoated, the I-CDI profile consistent with the literature was observed.

In the Bipolar mode CDI cycle, the salt adsorption capacity and charge efficiency were higher that NCDI mode for 101.5% CTAB/AC-88.1% SDS/AC-powder & 98.0% CTAB/AC-103.8 SDS/AC-precoated. But for 54.3% CTAB/AC-47.3% SDS/AC, both the salt adsorption capacity and charge efficiency became lower than the NCDI mode,mainly due to the co-ion effect.

With a three-electrode setup, it was observed that the voltage applied to the working electrode overshoot above +1.60 V vs. SHE during charging step (with a +1.20 V voltage bias) in the conventional CDI cycle and Bipolar CDI. This oxidized the AC and changed the surface chemistry (likely forming more -COOH groups). For this reason, the cells with AC-AC and Licap-Licap electrode pairs showed the flipped conductivity profile in NCDI and Bipolar CDI after they were subject to long cycles.

Chapter 3 - Electrochemical oxygen reduction reaction by metal free carbon

3.1 Introduction

H_2O_2 is a versatile chemical for its wide applications, such as bleaching agents [52], oxidizing agents[53], water treatment [54], etc. Recently, H_2O_2 has been explored as fuel for energy conversion and storage, and it was found H_2O_2 offers a higher volumetric density, simplifying storage, handling, and transportation [55] compared to H_2. This versatile application of H_2O_2 makes it a potential game-changing chemical. The recent dominating technique for H_2O_2 production is anthraquinone oxidation (AO), invented by the BASF method, which indirectly combines H_2 and O_2 in the presence of an organic quinone molecule to produce H_2O_2[55]. However, the centralized nature of this process, requiring a large industrial setup, and the requirement of a large volume of organic solvent limits its environmental friendliness[55]. The major drawback of a centralized chemical synthesis plant is in high transportation and storage cost, and risk of potential explosions. One common method to decentralize the synthesis of H_2O_2 is electrochemical H_2O_2 synthesis from the oxidation of water (WOR) and the reduction of O_2 (ORR). In both processes, the H_2O_2 is synthesized by a 2e- transfer reaction.

ORR: $O_2 + 2H^+ + 2e^- \rightarrow H_2O_2$ $E^o = +0.70$ V vs RHE…….. (3.1)

WOR: $2H_2O \rightarrow H_2O_2 + 2H^+ + 2e^-$ $E^o = +1.76$ V vs RHE……. (3.2)

This chapter will discuss the H_2O_2 synthesis from ORR with an aim to understand the electrocatalytic performance of a new type of graphitic carbon on H_2O_2 synthesis before and after nitrogen doping.

3.2 Materials

Melamine ($C_3H_6N_6$,99%, Sigma Aldrich, St. Louis, Missouri, USA)) was used as a nitrogen precursor in nitrogen-doped graphitic carbon synthesis. Perchloric acid ($HClO_4$, 70%) was used in preparing electrolytes to study the electrochemical properties of the catalyst. A Millipore water system (EASYPURE II, Thermo Scientific, Waltham, MA) was used for ultrapure water (18.2 MΩ cm at 25 °C) to prepare solutions for the experiments.

3.3 Materials characterization techniques

A transmission electron microscope (TEM) (Philips CM 100 TEM at a 100 kV acceleration voltage) was used for catalyst structure characterization. The Raman spectra for samples were recorded using a DXR Raman microscope with a 532 nm (2.33 eV) laser, (spot size 2.1 um, 50 um aperture). The Bruker AXS D8 Advance Discover Diffractometer (Bruker Corporation, Karlsruhe, Germany) with a Cu Kα radiation of wavelength 0.15418 nm and a detector slit width of 1 mm was used to analyze the crystal structure of the catalysts. The PHI 5000 Versa XPS system (Chanhassen, MN) with a monochromatized Al Kα source (1486.7 eV) was used to characterize the surface chemical composition of the catalysts. All the XPS spectra were obtained using a 400 μm spot size. The binding energy (B.E.) of all XPS data was calibrated vs the standard sp^2 C 1s peak at 284.60 eV. Shirley background of Origin software (version 2024b) was used in the curve fitting.

3.4 Synthesis, properties, and characterization of the graphitic carbon ($DG_{0.3}$)

Graphitic carbons ($DG_{0.3}$) were synthesized from the mixture of acetylene and oxygen at a mole ratio of 1: 0.3 by a detonation process. A detailed experimental procedure was provided in the literature[56].

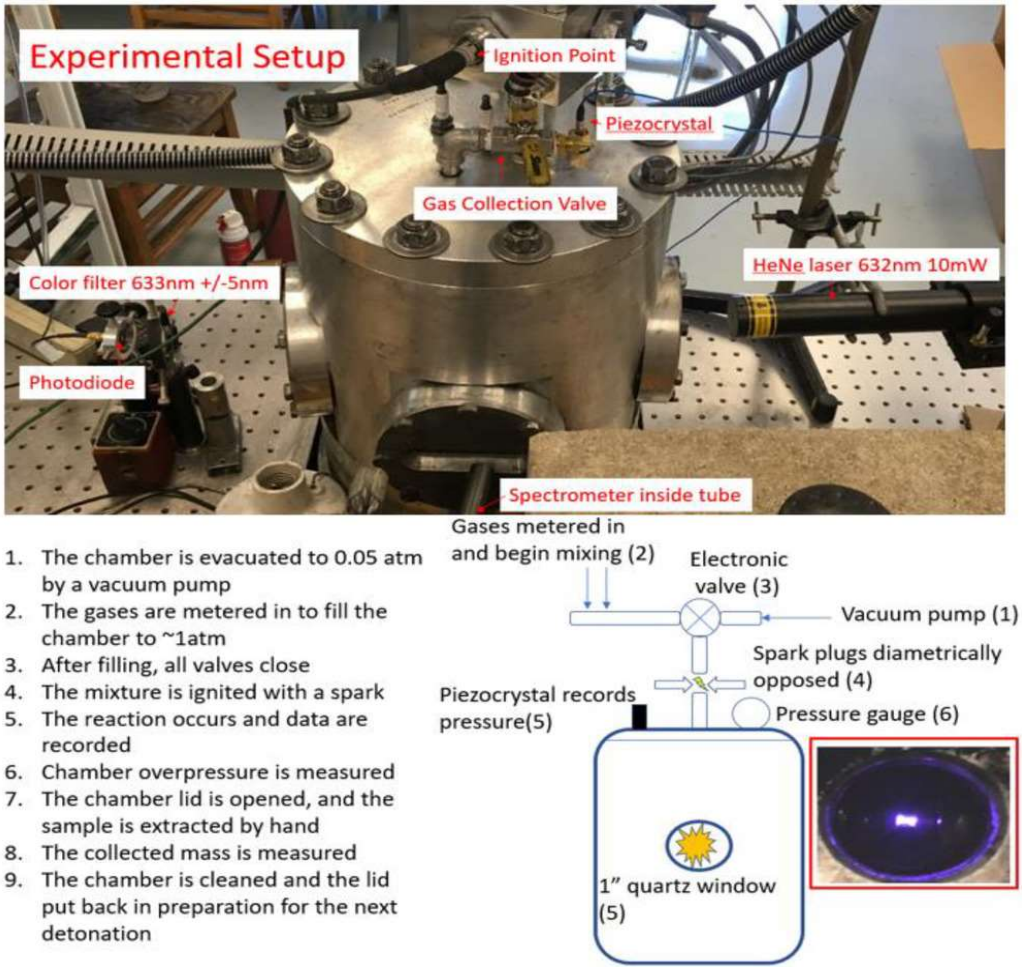

Figure 3-1: $DG_{0.3}$ synthesis setup and the synthesis procedure. Reprinted (adapted) with permission from J. P. Wright, S. Sigdel, S. Corkill, J. Covarrubias, L. LeBan, A. Nepal, J. Li, R. Divigalpitiya, S. H. Bossmann, C. M. Sorensen, Nano Select. 2022, 3, 1054. Copyright © 2021, John Wiley and Sons.

The Raman spectrum of DG0.3 shows the D, G, and 2D peaks respectively at 1330.6 cm^{-1}, 1558.2 cm^{-1}, and 2664.1 cm^{-1}, respectively. The I_D/I_G >1 indicates a high degree of disorder in the sample and I_{2D}/I_G <1 indicates the presence of a multilayer of the graphene sheet. The presence of multilayer in graphene sheet was confirmed by both XRD and TEM (Figure 3-2(b), (c)). The TEM images indicate a closed-cage structure with a nanoscale particle morphology with a size ranging from 50 to 100 nm (Figure 3-2(d)). The (002) graphene planes are located at 25.55° derived

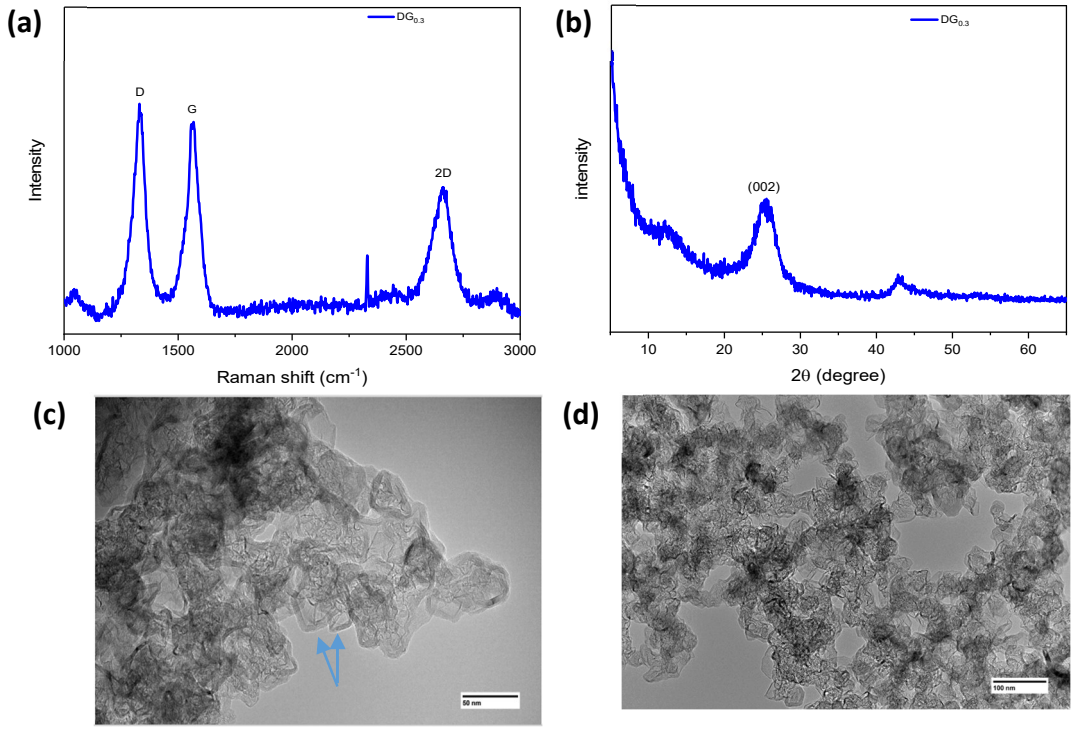

Figure 3-2: Characterization of $DG_{0.3}$: (a) Raman spectrum, (b) XRD, and (c) and (d) TEM images.

from XRD (Figure 3-2(b)), representing an interlayer spacing of 0.349 nm and number of graphene layers of ~7.

A detailed analysis of the Raman spectrum is given in the literature [56], shown in Figure 3-3. Two small peaks at 1897 cm^{-1} and 2052 cm^{-1} represents turbo-static nature of the graphene

which means random relative rotation between the adjacent layers[56]. The elemental composition of $DG_{0.3}$ is 99.8% C, 0.15% H and 0.05% O[56].

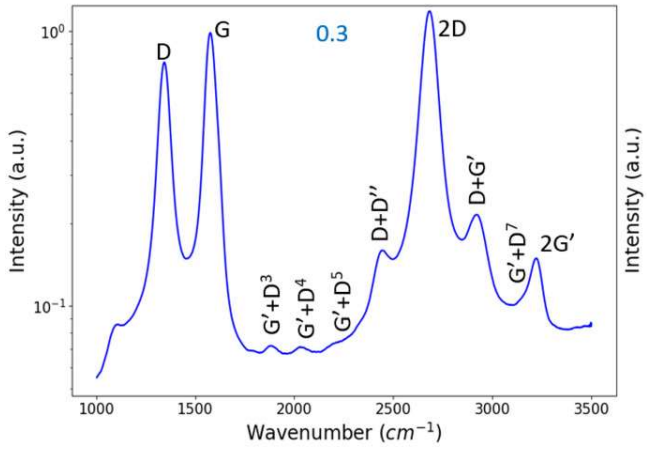

Figure 3-3: Raman spectrum of $DG_{0.3}$ presented in form of log of the intensity vs Raman shift (in wavenumber). Reprinted (adapted) with permission from J. P. Wright, S. Sigdel, S. Corkill, J. Covarrubias, L. LeBan, A. Nepal, J. Li, R. Divigalpitiya, S. H. Bossmann, C. M. Sorensen, Nano Select. 2022, 3, 1054. Copyright © 2021, John Wiley and Sons.

3.5 Nitrogen doped $DG_{0.3}$ synthesis:

The DG was first oxygenated by H_2SO_4-HNO_3 acid treatment, following the procedure from the literature[57]. 500 mg of $DG_{0.3}$ was treated in an aqueous mixture of 2.0 M H_2SO_4 and 4.0 M HNO_3 at 120 °C for 12 h under constant stirring. The obtained oxygenated $DG_{0.3}$ ($ODG_{0.3}$)

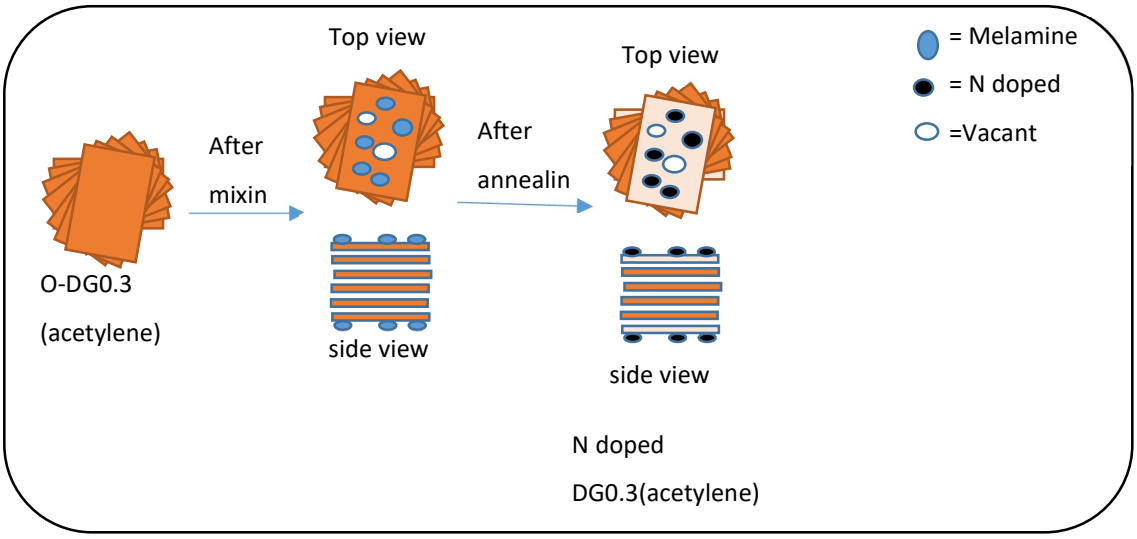

Figure 3-4: Synthesis of N doped $DG_{0.3}$.

was washed with ultrapure water until the pH reached ~7.0, collected by centrifugation at 3000 rpm for 10 min, and dried at 80 °C in a vacuum oven.

The N doping on $ODG_{0.3}$ was achieved by mixing the carbon sample with melamine, followed by thermal heating[58]. To begin with, 50 mg of ODG was dispersed in 30 mL methanol and sonicated for 1 hr. Then 125 mg of melamine was added to the mixture and sonicated for 1 hr. The obtained mixture was then stirred overnight at 500 rpm. Subsequently, the methanol was evaporated by heating the mixture at 35 ^oC until completely dried. The mixture sample was then ground for 5 minutes. Finally, the mixture was annealed in a tube furnace at 800 °C for 1 hr in an N_2 atmosphere with a 10 °C/min ramping to create N doping on $DG_{0.3}$.

3.6 Synthesized material characterization

The Raman spectrum (Figure 3-5(a)) showed 4 cm^{-1} blue shift in D-band and ~9 cm^{-1} blue shift in G-band after nitrogen doping on $DG_{0.3}$, indicating the presence of C-N in the structure. XRD analysis (Figure 3-5(b)) revealed a negative shift of 0.65^o in 2θ value after N doping which suggests an increase of interlayer spacing between the graphene layers. During the oxygen functionalization and thermal heating, the structural morphology of the graphene sample remained the same, which was confirmed by TEM (Figure 3-5(c)) and (d)). That demonstrates the stability of the sample.

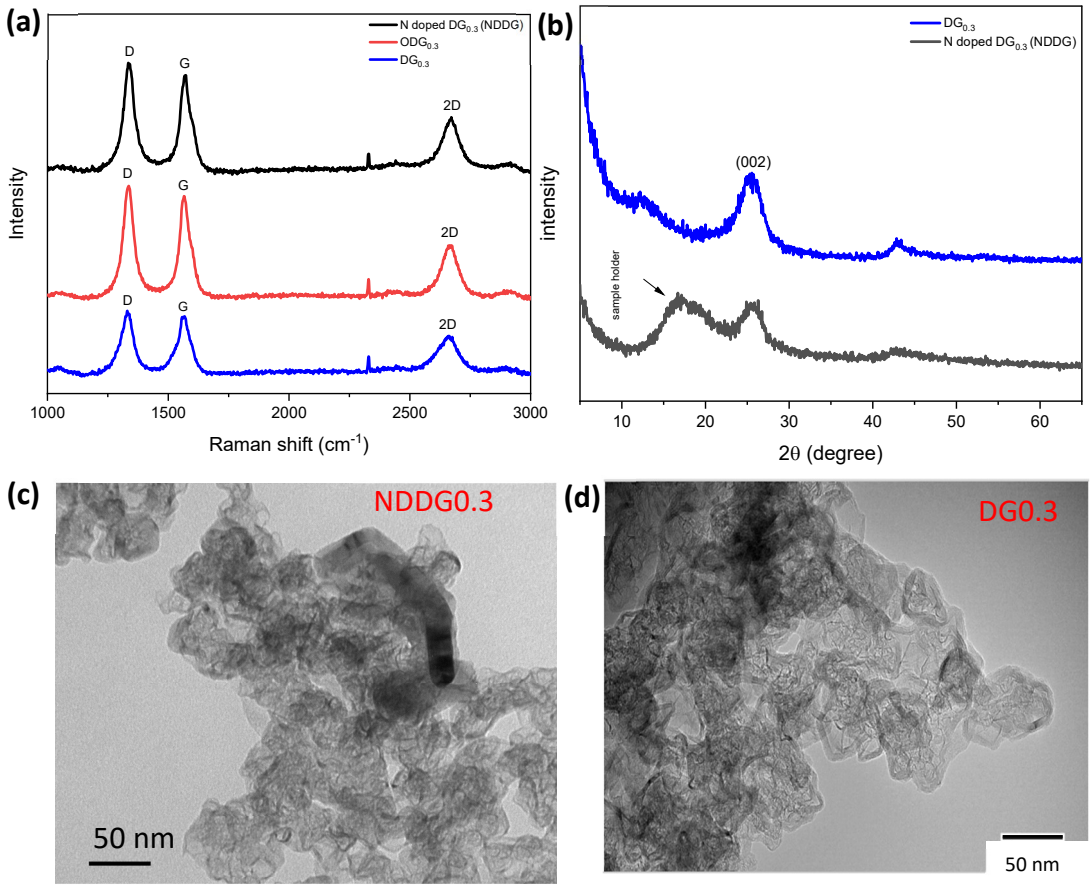

Figure 3-5: (a) Raman spectrum, (b) X-ray diffraction pattern, (c) TEM image of $NDDG_{0.3}$, and (d) TEM image of $DG_{0.3}$.

The XPS result further confirmed the doping of nitrogen in $DG_{0.3}$. The atomic percentage of nitrogen present in the sample was 1.25%. The deconvoluted N1s (Figure 3-6(a)) demonstrates the presence of 13.7% pyridinic N, 46.5% pyrrolic N, 20.9% graphitic N and 18.9% pyridinic N-oxide.

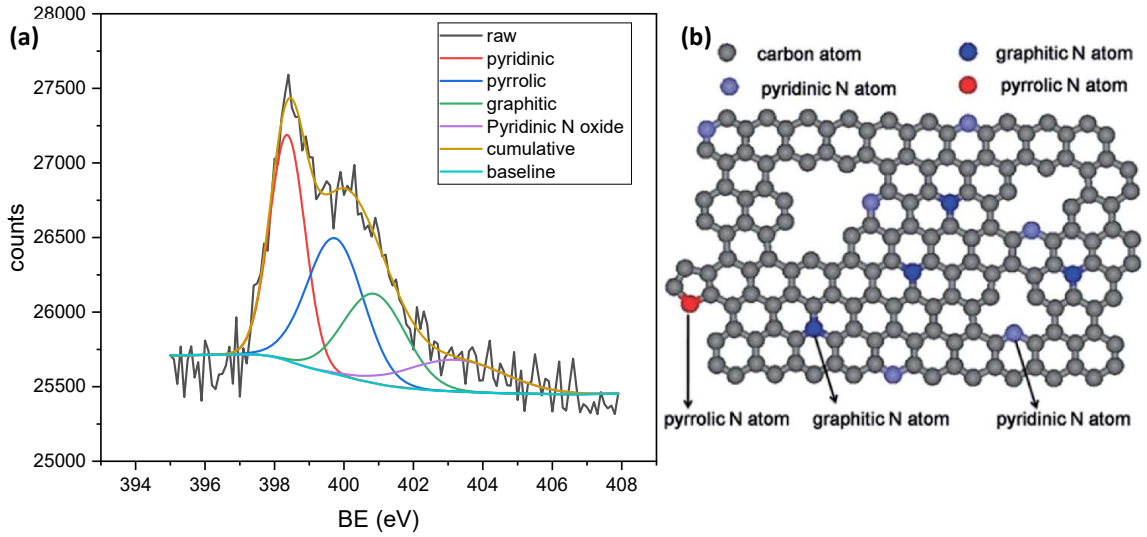

Figure 3-6: (a) Deconvoluted N 1s XPS spectrum, and (b) schematic of N doping on a graphene sheet. Panel (b) is reprinted (adapted) with permission from ACS Nano 2011, 5, 6, 4350–4358. Copyright © 2011, American Chemical Society.

3.7 Electrochemical characterization

All the electrochemical characterizations were performed in a standard three-electrode electrochemical cell using a rotating disk electrode (RDE) with a glassy carbon (GC) disk of 0.071 cm^2 embedded in PEEK surface or a rotating ring disk electrode (RRDE) with a GC disk of 0.125 cm^2 and a Pt ring (O.D. 7.0 mm and I.D. 5.0 mm) in PEEK surface controlled by a CHI 760D electrochemical workstation (CH Instruments, Austin, TX). The RDE or RRDE were controlled by the RRDE-3A Rotating Ring Disk Electrode Apparatus Ver.2.0 (ALS Co., Ltd, Japan). when using in the hydrodynamic conditions.

The catalyst ink was prepared by dispersing the required amount of active material (graphitic carbon or nitrogen-doped graphitic carbon) in 1.0 mL of a mixture of ethanol and ultrapure water (at a 3:1 volume ratio) with the addition of the required amount of Nafion solution

(5 wt % in lower aliphatic alcohols) so that the ionomer to carbon ratio was 0.4 . The working electrode was prepared by drop-casting the catalyst ink onto the GC RDE or RRDE. The loading of the active material was maintained at 250 μg/cm^2 for the half-cell studies. Before drop-casting the catalyst ink, the electrode was polished using 0.05 μm diameter alumina slurry to get a mirror finish. A graphite rod electrode (6.0 mm diameter) was employed as the counter electrode. A mercuric-mercurous sulfate (Hg/Hg_2SO_4) in saturated K_2SO_4 and silver-silver chloride (Ag/AgCl) in 1.0 M KCl were used as the reference electrodes. The electrolyte of 0.10 M $HClO_4$ (pH = 1.0) was used to study the activity of the catalysts.

The electrode potential values versus the Hg/Hg_2SO_4 reference electrode (in experiments carried out in 0.1 M $HClO_4$ solution, pH = 1.0) are converted to the values versus the RHE using the following equation:

E (vs. RHE) = E (vs Hg/Hg_2SO_4) + $E_{Hg/Hg2SO4}$ vs. NHE + 0.059 pH

= E (vs Hg/Hg_2SO_4) + 0.64 + 0.059 x 1

= E (vs Hg/Hg_2SO_4) + 0.699…… (3.3)

where E (vs Hg/Hg_2SO_4) is the experimentally measured potential versus the Hg/Hg_2SO_4 reference electrode (with saturated K_2SO_4 filling solution) and $E_{Hg/Hg2SO4}$ vs. NHE = 0.64 V.

Cyclic voltammetry (CV) and linear sweep voltammetry (LSV) were done for electrochemical characterizations. Before studying the ORR catalytic activity, the solution was bottom purged by an ultrapure Ar gas for 10 minutes and then switched to top purge. The CV was done in the stationary condition in the potential range +1.194 V vs RHE to -0.406V vs RHE at a scan rate of 50 mV/s for 25 cycles and the LSV was done in hydrodynamic conditions at 400 rpm, 800 rpm, 900 rpm, 1200 rpm and 1600 rpm from +0.899 V vs RHE to -0.501 V vs RHE at a scan rate of 10 mV/s for activation and collecting the background. Then the purging gas was switched to O_2 and run 5 cycles CV followed by LSV at different rotation rate in the same potential window as mentioned before.

The LSV measurement with RRDE was the same as with RDE, except the Pt ring is set at a potential of 1.20 V vs RHE. The collection efficiency (n) is 43%. The collection efficiency was determined from the ring and disk current ratios in 10 mM $K_3[Fe(CN)_6]$ solution.

3.8- Results and discussion of electrochemical characterization

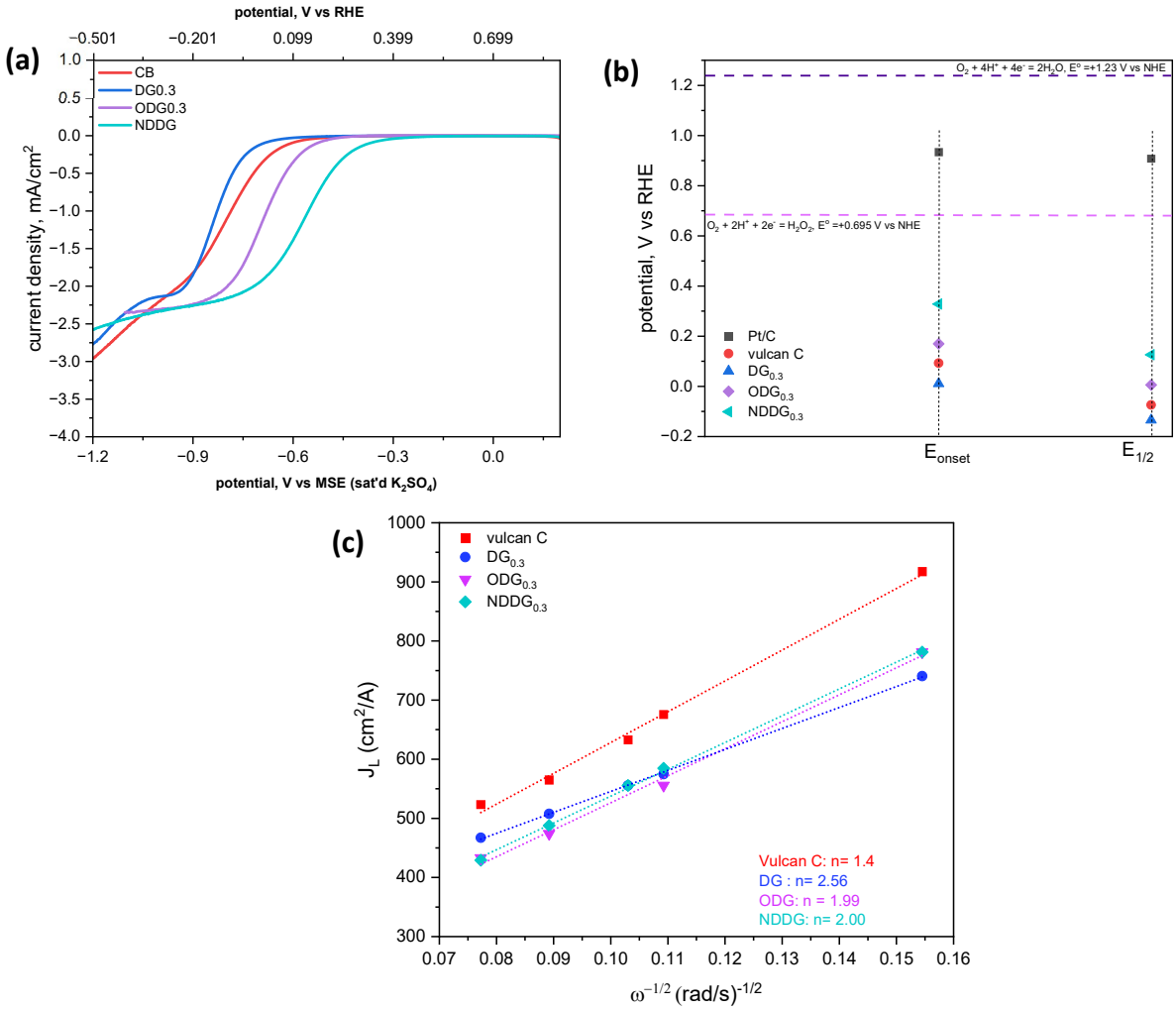

Figure 3-7: (a) LSV at 1600 rpm of different catalysts (background subtracted) in 0.10 M $HClO_4$, (b) the half-wave potential and onset potential of different catalysts in ORR, and (c) K-L plot analysis of different catalyst.

The CV for $DG_{0.3}$, $ODG_{0.3}$, $NDDG_{0.3}$ in Ar and O_2 purged 0.10 M $HClO_4$ are present in Appendix Figures B.1(a), B.2(a), and B.3(a), respectively. The prominent ORR peak in O_2 purged solution indicates the catalysts' activity towards ORR. The background subtracted LSV at 1600 rpm with RDE for different catalysts presented in Figure 3-7(a). It has been seen that, the N-doped DG0.3 has an earlier onset potential (+0.328 V vs. RHE) and half wave potential (+0.126 V vs RHE) compared to $ODG_{0.3}$ (onset potential: +0.170 V vs. RHE and half-wave potential: +0.006 V vs. RHE) and $DG_{0.3}$ (onset potential: +0.011 V vs. RHE and half-wave potential: -0.134V vs. RHE). This suggests an enhanced catalytic activity due to nitrogen doping. Upon incorporation of nitrogen atoms into the graphene sheet, the charge density was rearranged because of the

electronegativity differences between carbon and nitrogen. This alteration allowed O_2 molecules to be readily attracted to the catalysts and led to the higher catalytic activity[59, 60]. However, despite the significant improvement (+317 mV shift) in the onset potential compared to pristine $DG_{0.3}$, the onset potential for $NDDG_{0.3}$ still far away from the theoretical value for $2e^-$ reduction reaction of O_2 (E^o = +0.695 V vs RHE). The reason could be due to the relatively low amount of nitrogen doping in $DG_{0.3}$ and the limited percentages of pyridinic and graphitic N sites, which are considered to be the active sites for ORR[61, 62]. Further work needs to be done to enhance the nitrogen at% present in the sample and more pyridinic and graphic active sites.

The number of electron transport can be calculated from Koutecky-Levice (K-L) analysis[60] by plotting the inverse of the limiting current density J_L (mA/cm^2) vs. the square root of inversed ration rate $\omega^{-1/2}$ (rad/s)$^{-1/2}$ from LSV at different rotation rates.

$$\frac{1}{j} = \frac{1}{B\omega^{1/2}} + \frac{1}{j_k} \quad \text{..... (3.4)}$$

$$B = 0.20nF[O_2]{D_{O2}}^{3/2}\vartheta^{-1/6} \quad \text{..... (3.5)}$$

where ω = electrode rotating speed in rpm,

j = current density in A/cm^2,

B = reciprocal of the slope,

$[O_2]$ = concentration of O_2, mol/cm^3

D_{O_2} = O_2 diffusion coefficient (cm^2/s), and

ϑ = electrolyte kinematic viscosity (cm^2/s).

From Figure 3-7(c), the number of electron transport is ~2 for all the catalysts. That indicates that the ORR by the N doped $DG_{0.3}$, $ODG_{0.3}$, $DG_{0.3}$, and Vulcan C all followed a 2e- transfer ORR pathway.

The results of RRDE experiments for N-doped $DG_{0.3}$ is presented in Figure 3-8 and the electron transfer number n and percentage selectivity of H_2O_2 yield can be derived by equations (3.6) and (3.7)[60]. In the potential range from +0.099 V vs. RHE to -0.101 V vs. RHE, the H_2O_2 yield has reached a maximum of 60%, and the number of electron transfer is 2.8. This supports the previous finding that indicates the majority of the ORR followed the $2e^-$ pathway and produced H_2O_2. Only a small portion of ORR followed the $4e^-$ pathway and produced H_2O with some of the H_2O_2 being further reduced to H_2O.

$$n = 4\,x\,\frac{I_D}{I_D + I_R/N} \quad \text{..... (3.6)}$$

$$\% H_2O_2 \; yield \; = \; 200 \; x \; \frac{I_D}{I_D + I_R/N} \ldots\ldots\ldots (3.7)$$

$I_D \; = \; Disc \; current, mA$

I_R = Ring current, mA.

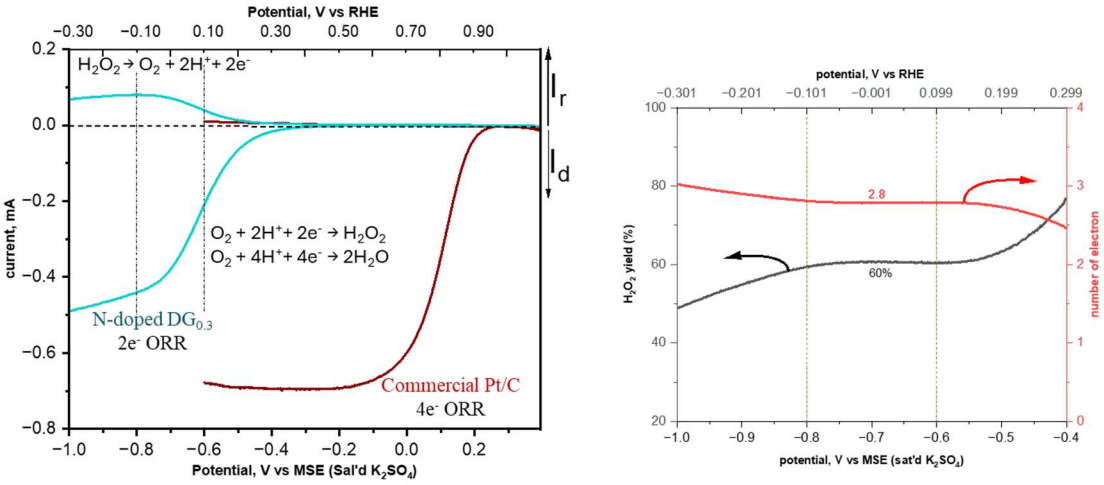

Figure 3-8: (a) LSV at 1600 *rpm with* RRDE *for N-doped* $DG_{0.3}$ and a commercial Pt/C catalyst, and (b) the calculated H_2O_2% yield and number of electrons n for N-doped $DG_{0.3}$.

3.9 Conclusion

In summary, we have demonstrated that, after N-doping by a post-growth process, the detonation graphene $DG_{0.3}$ showed substantial positive shifts in the onset potential and half-wave potential for ORR. This N-doped DG0.3 showed a 2e transfer ORR pathway, which has been confirmed by K-L plot analysis of LSV curves obtained with RDE and RRDE, respectively. From LSV with RRDE, the H_2O_2 yield was also derived to be 60%. The future work targeting enhancing N at% in the sample and co-doping with other non-metal atoms may further improve the $2e^-$ ORR pathway.

Chapter 4 - Conclusions and future outlook

Modifying carbon materials will undoubtedly continue to play a crucial role in clean technologies. This research work investigated two distinct approaches: surfactant-modified carbon for water desalination and N-doped graphitic carbon for H_2O_2 synthesis.

In Chapter 2, a quantifiable and controllable method of cationic and anionic surfactants modification to the AC powder and pre-coated AC electrodes was demonstrated. From this, The equilibrium CTAB adsorption capacity is 477.89 $\pm$ 2.98 (95%CI) mg_{CTAB}/g_{AC} and SDS adsorption capacity is 493.65 $\pm$ 1.34 (95% CI) mg_{SDS}/g_{AC}. The modified AC powder and pre-coated AC electrodes showed better stability and charge efficiency compared to non-modified AC, but the salt adsorption capacity is lower compared to the pristine AC electrodes due to the pore blocking by the surfactants. The mechanism of ion adsorption and the role of surfactants on AC during the CDI cycling were investigated. It can be concluded that the surfactant coatings on the AC can act as charge selective membrane. Future work needs to be done to enhance the salt adsorption capacity. A possible area of investigation could be understanding the effect of size of surfactant molecules and a mixture of ionic and nonionic surfactants for CDI.

In Chapter 3, a post-growth thermal treatment method was developed to introduce nitrogen doping into a special form of graphitic carbon produced by a scalable detonation process, i.e., $DG_{0.3}$. It showed that, after N-doing, the electrocatalytic performance of $DG_{0.3}$ for ORR was improved, with the onset and half wave potentials shift by ~+300 mV compared to $DG_{0.3}$. From the K-L plot analysis of the RDE LSV curves, the number of electron transfer was determined to be ~2, indicating a $2e^-$ ORR mechanism, which is consistent with the RRDE analysis. The H_2O_2 yield was determined to be 60% from RRDE measurements.

References

1. Mestre, A.S., et al., *Chapter 17 - Activated carbons in full-scale advanced wastewater treatment*, in *Advanced Materials for Sustainable Environmental Remediation*, D. Giannakoudakis, L. Meili, and I. Anastopoulos, Editors. 2022, Elsevier. p. 433-475.
2. Ayaz, M., et al., *Sustainable seawater desalination: Current status, environmental implications and future expectations.* Desalination, 2022. **540**: p. 116022.
3. Kothandam, G., et al., *Recent Advances in Carbon-Based Electrodes for Energy Storage and Conversion.* Advanced Science, 2023. **10**(18): p. 2301045.
4. Wang, N., et al., *Recent Progress of Electrochemical Production of Hydrogen Peroxide by Two-Electron Oxygen Reduction Reaction.* Advanced Science, 2021. **8**(15): p. 2100076.
5. Gao, Y., et al., *Doping strategy, properties and application of heteroatom-doped ordered mesoporous carbon.* RSC Advances, 2021. **11**(10): p. 5361-5383.
6. Sun, K., et al., *Electrocapacitive Deionization: Mechanisms, Electrodes, and Cell Designs.* Advanced Functional Materials, 2023. **33**(18): p. 2213578.
7. Helmholtz, H., *Studien über electrische Grenzschichten.* Annalen der Physik, 1879. **243**(7): p. 337-382.
8. Gouy, G., *Sur la constitution de la charge électrique à la surface d'un électrolyte J.* Phys. Radium (Paris)(9: 457-468), 1910.
9. Chapman, D.L., *LI. A contribution to the theory of electrocapillarity.* The London, Edinburgh, and Dublin philosophical magazine and journal of science, 1913. **25**(148): p. 475-481.
10. Liu, E., et al., *Treatment of industrial brine using capacitive deionization (CDI) towards zero liquid discharge – challenges and optimization.* Water Research, 2020. **183**: p. 116059.
11. Biesheuvel, P.M. and A. van der Wal, *Membrane capacitive deionization.* Journal of Membrane Science, 2010. **346**(2): p. 256-262.
12. Biesheuvel, P.M., et al., *Theory of membrane capacitive deionization including the effect of the electrode pore space.* Journal of Colloid and Interface Science, 2011. **360**(1): p. 239-248.
13. Nakamura, M., et al., *Outer Helmholtz Plane of the Electrical Double Layer Formed at the Solid Electrode–Liquid Interface.* ChemPhysChem, 2011. **12**(8): p. 1430-1434.
14. Zhao, R., P.M. Biesheuvel, and A. van der Wal, *Energy consumption and constant current operation in membrane capacitive deionization.* ENERGY & ENVIRONMENTAL SCIENCE, 2012. **5**(11): p. 9520-9527.
15. Porada, S., et al., *Direct prediction of the desalination performance of porous carbon electrodes for capacitive deionization.* Energy & Environmental Science, 2013. **6**(12): p. 3700.
16. Ntakirutimana, S., et al., *Editors' Choice—Review—Activated Carbon Electrode Design: Engineering Tradeoff with Respect to Capacitive Deionization Performance.* Journal of The Electrochemical Society, 2020. **167**(14): p. 143501.
17. Liu, P., et al., *Grafting sulfonic and amine functional groups on 3D graphene for improved capacitive deionization.* Journal of Materials Chemistry A, 2016. **4**(14): p. 5303-5313.

18. Andelman, M., *Ionic Group Derivitized Nano Porous Carbon Electrodes for Capacitive Deionization.* Journal of Materials Science and Chemical Engineering, 2014. **02**(03): p. 16-22.
19. Porada, S., et al., *Review on the science and technology of water desalination by capacitive deionization.* Progress in Materials Science, 2013. **58**(8): p. 1388-1442.
20. Ntakirutimana, S., et al., *Editors' Choice-Review-Activated Carbon Electrode Design: Engineering Tradeoff with Respect to Capacitive Deionization Performance.* Journal of the Electrochemical Society, 2020. **167**(14).
21. Biesheuvel, P.M., H.V.M. Hamelers, and M.E. Suss, *Theory of Water Desalination by Porous Electrodes with Immobile Chemical Charge.* Colloids and Interface Science Communications, 2015. **9**: p. 1-5.
22. Li, L., et al., *Metal–organic frameworks: a promising platform for constructing non-noble electrocatalysts for the oxygen-reduction reaction.* Journal of Materials Chemistry A, 2019. **7**(5): p. 1964-1988.
23. Gleick, I. and P. White, *Pacific Institute for Studies in Development, Environment, and Security., & Stockholm Environment Institute*. 1993, New York: Oxford University Press.
24. Eileen Poeter, Y.F., John Cherry, Warren Wood, Doug Mackay,, *Groundwater in our water cycle – getting to know Earth's most important fresh water source*. 2020, The Groundwater Project, Guelph, Ontario, Canada.
25. Krishan, G., et al. *Groundwater Salinity—Impacts and Possible Remedial Measures and Management Solutions*. in *Transforming Coastal Zone for Sustainable Food and Income Security*. 2022. Cham: Springer International Publishing.
26. Anderson, M.A., A.L. Cudero, and J. Palma, *Capacitive deionization as an electrochemical means of saving energy and delivering clean water. Comparison to present desalination practices: Will it compete?* Electrochimica Acta, 2010. **55**(12): p. 3845-3856.
27. Cheng, R., et al., *Effect of exerted magnetic field on the performance of non-aqueous iron-vanadium redox flow battery with deep eutectic solvent (DES) electrolyte.* Electrochimica Acta, 2021. **399**: p. 139404.
28. Hou, C.-H. and C.-Y. Huang, *A comparative study of electrosorption selectivity of ions by activated carbon electrodes in capacitive deionization.* Desalination, 2013. **314**: p. 124-129.
29. Frackowiak, E., et al., *Optimisation of supercapacitors using carbons with controlled nanotexture and nitrogen content.* Electrochimica Acta, 2006. **51**(11): p. 2209-2214.
30. Lal, M.S. and R. Sundara, *Multifunctional high entropy oxides incorporated functionalized biowaste derived activated carbon for electrochemical energy storage and desalination.* Electrochimica Acta, 2022. **405**: p. 139828.
31. Pal, A., et al., *A benchmark for CO2 uptake onto newly synthesized biomass-derived activated carbons.* Applied Energy, 2020. **264**: p. 114720.
32. Hassanvand, A., et al., *The Role of Ion Exchange Membranes in Membrane Capacitive Deionisation.* Membranes, 2017. **7**(3): p. 54.
33. Han, L., et al., *Mechanistic insights into the use of oxide nanoparticles coated asymmetric electrodes for capacitive deionization.* Electrochimica Acta, 2013. **90**: p. 573-581.
34. Lee, J.-B., et al., *Desalination of a thermal power plant wastewater by membrane capacitive deionization.* Desalination, 2006. **196**(1-3): p. 125-134.

35. Qiu, Q., et al., *Preparation of stable polyethylene membranes filled with crosslinked sulfonated polystyrene for membrane capacitive deionization by γ-irradiation.* Macromolecular Research, 2017. **25**(1): p. 92-95.
36. Lee, J.-Y., et al., *Preparation of ion exchanger layered electrodes for advanced membrane capacitive deionization (MCDI).* Water Research, 2011. **45**(17): p. 5375-5380.
37. Kim, J.S., et al., *Application of synthesized anion and cation exchange polymers to membrane capacitive deionization (MCDI).* Macromolecular Research, 2015. **23**(4): p. 360-366.
38. Gu, X., Y. Deng, and C. Wang, *Fabrication of Anion-Exchange Polymer Layered Graphene–Melamine Electrodes for Membrane Capacitive Deionization.* ACS Sustainable Chemistry & Engineering, 2017. **5**(1): p. 325-333.
39. Kim, J.S., Y.S. Jeon, and J.W. Rhim, *Application of poly(vinyl alcohol) and polysulfone based ionic exchange polymers to membrane capacitive deionization for the removal of mono- and divalent salts.* Separation and Purification Technology, 2016. **157**: p. 45-52.
40. Simón, M.M.B., A.D.E. Cózar, and L.M.P. Díez, *Spectrophotometric determination of cationic surfactants in frozen and fresh squid by ion-pair formation with Methyl Orange.* The Analyst, 1990. **115**(3): p. 337-339.
41. Wang, L. and D. Langley, *Determining Cationic Surfactant Concentration.* Product R&D, 1975. **14**(3): p. 210-212.
42. Hayashi, K., *A rapid determination of sodium dodecyl sulfate with methylene blue.* Analytical Biochemistry, 1975. **67**(2): p. 503-506.
43. Ntakirutimana, S. and W. Tan, *Synergistic effects of ionic and nonionic surfactants treatment on activated carbon electrodes for inverted capacitive deionization.* Separation and Purification Technology, 2021. **258**: p. 117987.
44. Baumann, A.E., et al., *Promoting sulfur adsorption using surface Cu sites in metal–organic frameworks for lithium sulfur batteries.* Journal of Materials Chemistry A, 2018. **6**(11): p. 4811-4821.
45. Yeh, C.-L., et al., *Improved performance in capacitive deionization of activated carbon electrodes with a tunable mesopore and micropore ratio.* Desalination, 2015. **367**: p. 60-68.
46. Zhao, S., et al., *High capacity and high rate capability of nitrogen-doped porous hollow carbon spheres for capacitive deionization.* Applied Surface Science, 2016. **369**: p. 460-469.
47. Liu, N.-L., S.-H. Sun, and C.-H. Hou, *Studying the electrosorption performance of activated carbon electrodes in batch-mode and single-pass capacitive deionization.* Separation and Purification Technology, 2019. **215**: p. 403-409.
48. Kim, T. and J. Yoon, *Relationship between capacitance of activated carbon composite electrodes measured at a low electrolyte concentration and their desalination performance in capacitive deionization.* Journal of Electroanalytical Chemistry, 2013. **704**: p. 169-174.
49. Al-Rajabi, M.M., et al., *Capacitive deionization for water desalination: Cost analysis, recent advances, and process optimization.* Journal of Water Process Engineering, 2024. **58**: p. 104816.
50. Ahmed, M.A. and S. Tewari, *Capacitive deionization: Processes, materials and state of the technology.* Journal of Electroanalytical Chemistry, 2018. **813**: p. 178-192.

51. Fritz, P.A., R.M. Boom, and K. Schroen, *Polyelectrolyte-activated carbon composite electrodes for inverted membrane capacitive deionization (iMCDI).* Separation and Purification Technology, 2019. **220**: p. 145-151.
52. Swaminathan, K., et al., *Decolorization and degradation of H-acid and other dyes using ferrous–hydrogen peroxide system.* Chemosphere, 2003. **50**(5): p. 619-625.
53. He, C., et al., *Reinvestigating FeBr₃-Catalyzed Alcohol Oxidation with H₂O₂: Is a High-Valent Iron Species (HIS) or a Reactive Brominating Species (RBS) Responsible for Alcohol Oxidation?* Organic Letters, 2022. **24**(19): p. 3499-3503.
54. Adeyinka, J.S. and A. Rim-Rukeh, Environmental Monitoring and Assessment, 1999. **59**(3): p. 249-256.
55. Siahrostami, S., *H2O2 electrosynthesis and emerging applications, challenges, and opportunities: A computational perspective.* Chem Catalysis, 2023. **3**(3): p. 100568.
56. Wright, J.P., et al., *Synthesis of turbostratic nanoscale graphene via chamber detonation of oxygen/acetylene mixtures.* Nano Select, 2022. **3**(6): p. 1054-1068.
57. Sekar, A., et al., *PtRu Catalysts on Nitrogen-Doped Carbon Nanotubes with Conformal Hydrogenated TiO2 Shells for Methanol Oxidation.* ACS Applied Nano Materials, 2022. **5**(3): p. 3275-3288.
58. Ra, E.J., et al., *Synthesis of nitrogen doped graphite oxide and its electrochemical properties.* Current Applied Physics, 2014. **14**(1): p. 82-86.
59. Dai, L., et al., *Metal-Free Catalysts for Oxygen Reduction Reaction.* Chemical Reviews, 2015. **115**(11): p. 4823-4892.
60. Ma, R., et al., *A review of oxygen reduction mechanisms for metal-free carbon-based electrocatalysts.* npj Computational Materials, 2019. **5**(1).
61. Lai, L., et al., *Exploration of the active center structure of nitrogen-doped graphene-based catalysts for oxygen reduction reaction.* Energy & Environmental Science, 2012. **5**(7): p. 7936-7942.
62. Kim, H., et al., *On the mechanism of enhanced oxygen reduction reaction in nitrogen-doped graphene nanoribbons.* Physical Chemistry Chemical Physics, 2011. **13**(39): p. 17505.

Appendix A - Supplementary Information for Chapter 2

A.1-Number of extraction determination to separate MO-CTAB complex from aqueous phase to organic phase

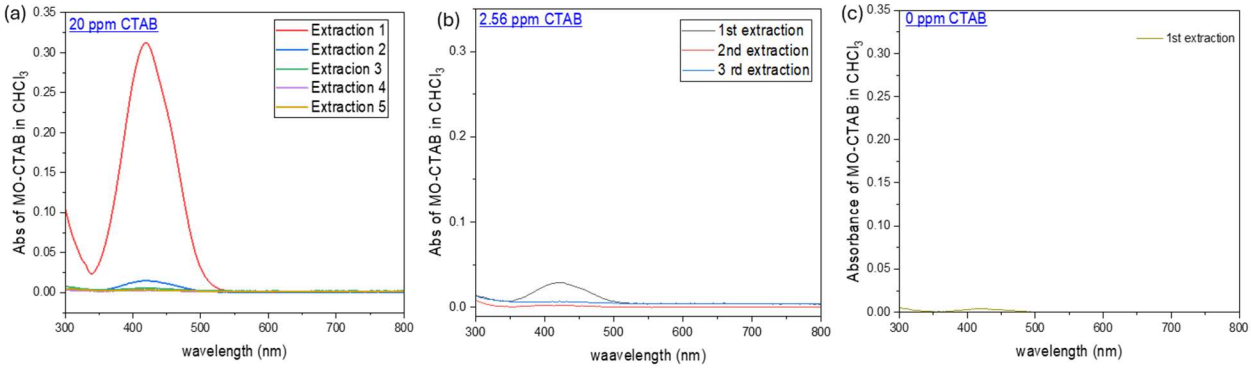

Figure A 1: UV-Vis's absorption of MO-CTAB after extraction (a) 20 ppm CTAB, (b) 2.6 ppm CTAB, and (c) 0 ppm CTAB.

It was found that a negligible amount of MO (methyl orange) gets extracted to organic phase. After subtracting the absorbance contribution from free MO, in single extraction more than 90% MO-CTAB complex ions are transferred from aqueous phase to organic phase. So, for further analysis only one extraction is used to separate MO-CTAB complex from aqueous phase to organic phase.

A.2-Absorbance of MO-CTAB in $CHCl_3$ vs standard CTAB solution concentration-Calibration graph

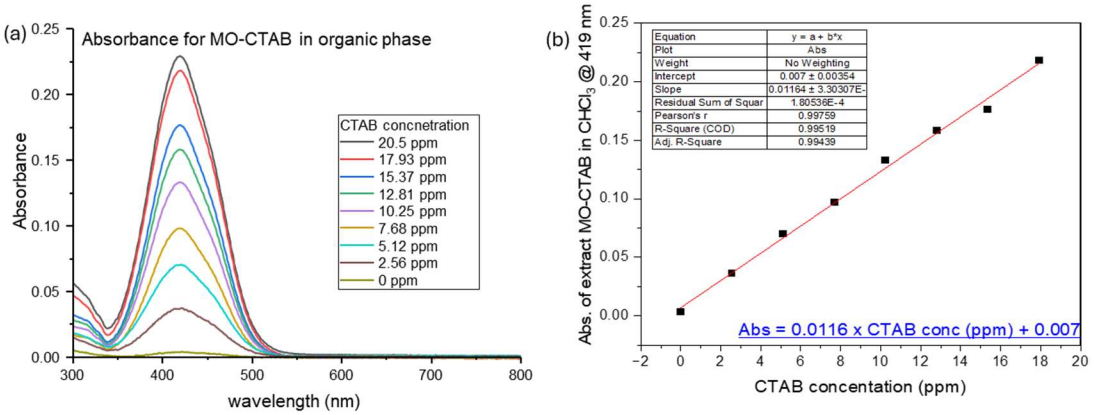

Figure A 2: (a) UV-Vis absorbance for standard CTAB solution, and (b) Calibration graph to determine free CTAB in solution.

A.3- Number of extraction determination to separate MB-SDS complex from aqueous phase to organic phase

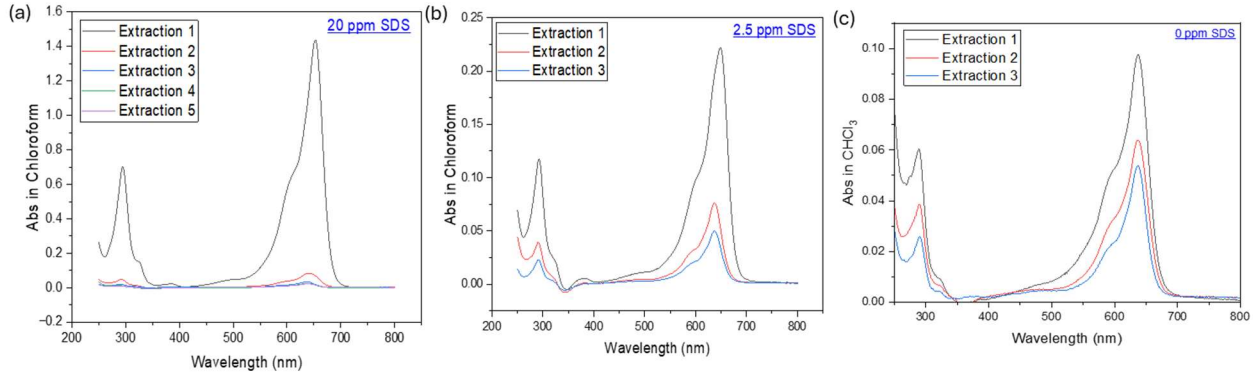

Figure A 3:UV-Vis's absorption of MB-SDS after extraction (a) 20 ppm SDS, (b) 2.5 ppm SDS, and (c) 0 ppm SDS

It was found that a small amount of MB (methylene blue) gets extracted to organic phase. After subtracting the absorbance contribution from free MB, in single extraction more than 90% MB-SDS complex ions are transferred from aqueous phase to organic phase. So, for further analysis only one extraction is used to separate MB-SDS complex from aqueous phase to organic phase.

A.4-Absorbance of MO-CTAB in $CHCl_3$ vs standard SDS solution concentration-Calibration graph

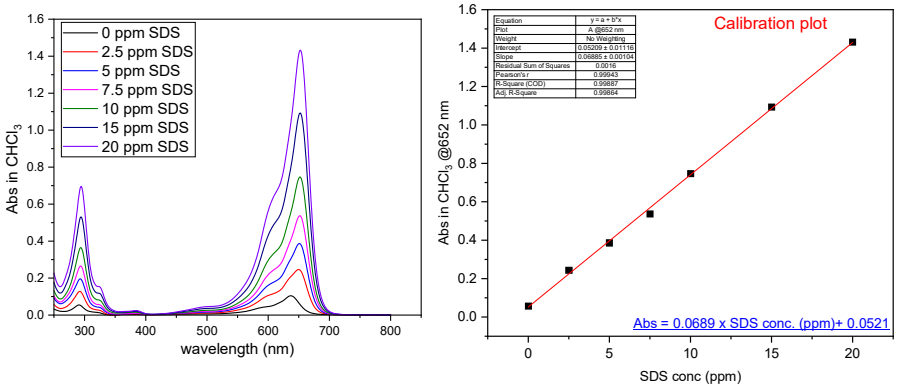

Figure A 4: (a) UV-Vis absorbance for standard SDS solution, and (b)Calibration graph to determine free SDS in solution.

A.5-Adsorption Kinetics of Surfactant on AC powder and precoated AC-electrode

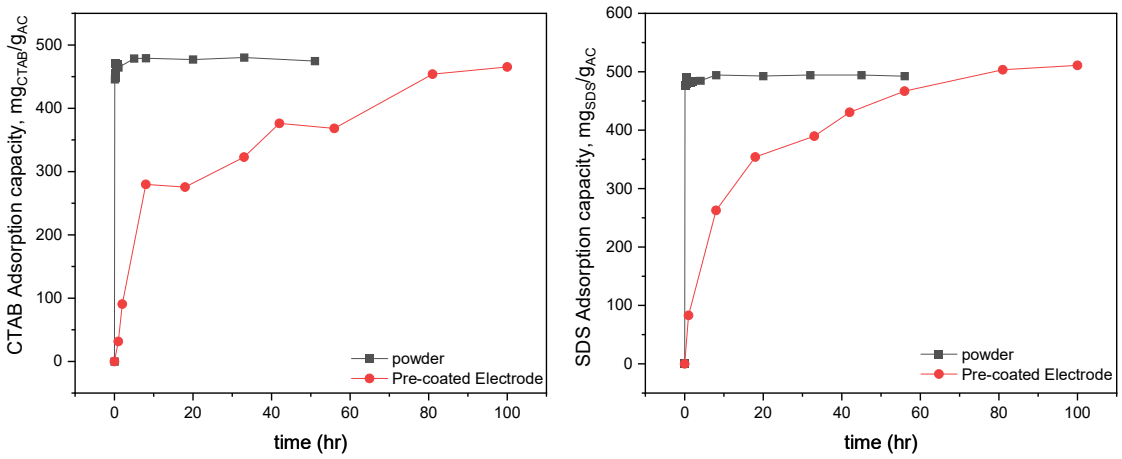

Figure A 5:Comparison of surfactant adsorption kinetics for powder AC and pre-coated AC (a) CTAB (b) SDS

A.6- Washing of surfactant modified AC:

Washing of CTAB modified AC: For washing of CTAB from CTAB/AC 250 mL ultrapure water was used each washing. Upto 11th washing the total CTAB leach out is 7.35 mg. That is 0.15% of total CTAB absorbed to the electrode.

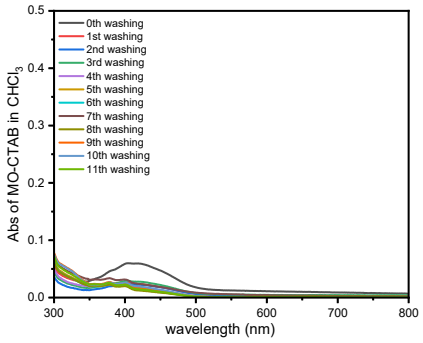

Figure A 6: washing of CTAB/AC

Washing of CTAB modified AC: For washing of weakly bonded SDS from SDS/AC 250 mL ultrapure water was used each washing. Up to 14th washing the total SDS leach out is 137.6 mg. That is 3.0% of total SDS absorbed to the electrode.

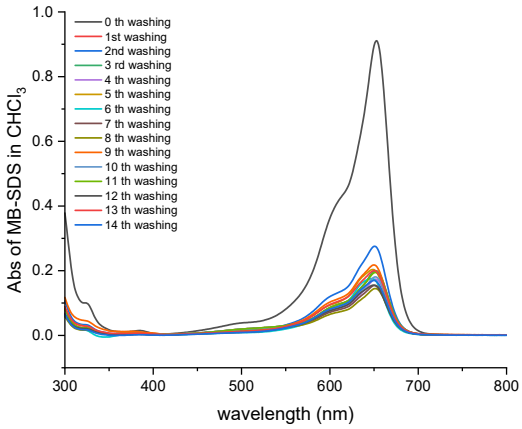

Figure A 7: washing of SDS/AC

A.7- TGA Characterization and Calculations:

Constituents of AC/SDS:

x = fraction of activated carbon (AC)

y = fraction of SDS

z = fraction of adsorbed moisture

x + y + z = 1……(B1)

Weight lost at 600 ºC = 0.00743x + 0.7427y + z = 0.2739……(B2)

Weight lost at 120 ºC = z = 0.0507……. (B3)

By Solving equations B1, B2, B3,

Wt % of AC = 65.53 %

Wt % of SDS = 29.39 %

Wt % of adsorbed moisture = 5.08 %

Constituents of AC/CTAB:

a = fraction of activated carbon (AC)

b = fraction of CTAB

c = fraction of adsorbed moisture

a + b + c = 1……. (B4)

Weight lost at 600 ºC = 0.00743a + b + c = 0.3371……. (B5)

Weight lost at 120 ºC = c = 0.0293……. (B6)

Solving equation B4, B5, B6,

Wt % of AC = 66.8 %

Wt % of CTAB = 30.3 %

Wt % of adsorbed moisture = 2.9 %

A.8- Effect of electrode thickness on electrode capacitance

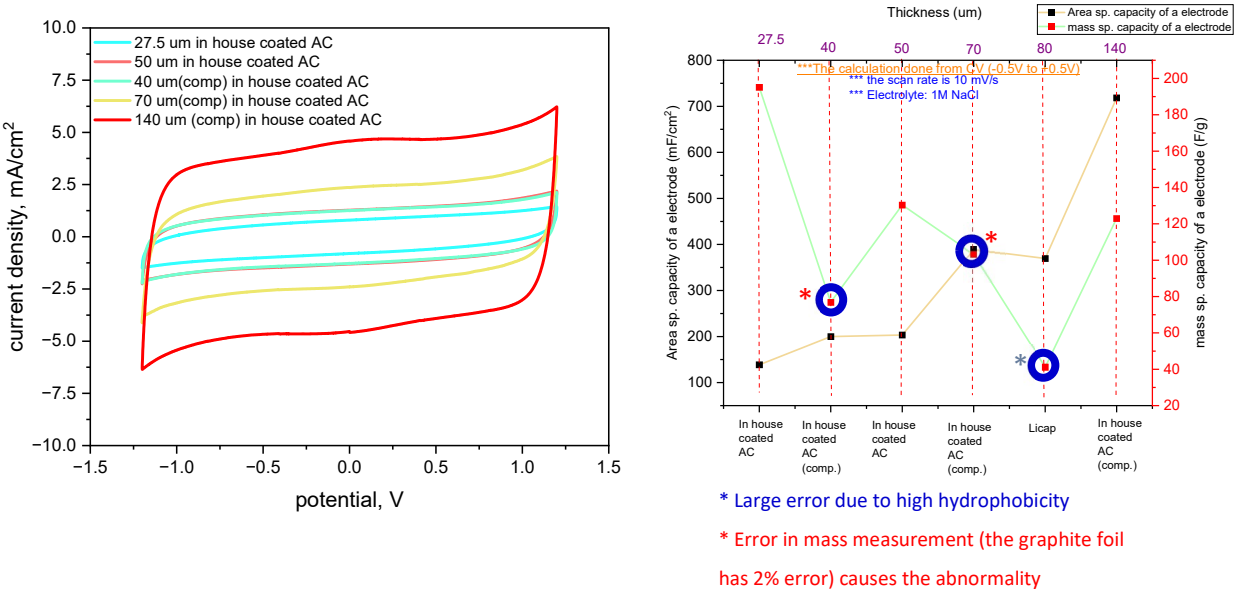

Figure A 8:Effect of electrode thickness on electrode mass specific and area specific capacitance.

From figure A6, it can be seen that the increase of electrode thicknesses the area specific capacity increases. With the increase of catalyst thickness the mass loading increases but due to thicker coating thickness the electrolyte cannot effectively use the whole active electrode for ion adsorption. That causes the mass specific capacity to decrease.

Appendix B - Supplementary Information for Chapter 3

The electrocatalytic ORR performance of $DG_{0.3}$, $ODG_{0.3}$, $NDDG_{0.3}$ presented in figure B7, B8 and B9.

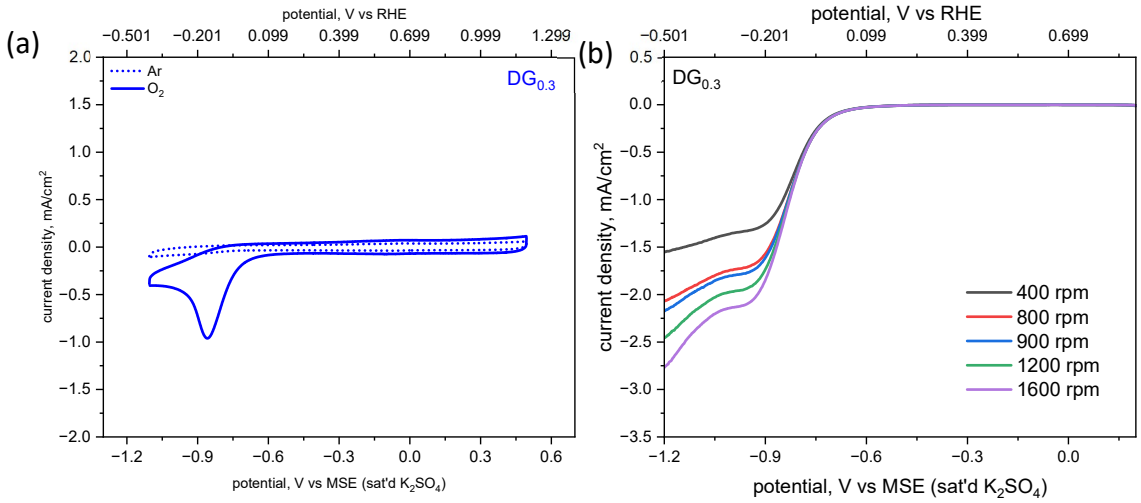

Figure B 1: (a) CV in Ar (dash line) and O_2 (solid line) (b) LSV at 400 rpm, 800 rpm, 900 rpm, 1200 rpm, 1600 rpm for $DG_{0.3}$

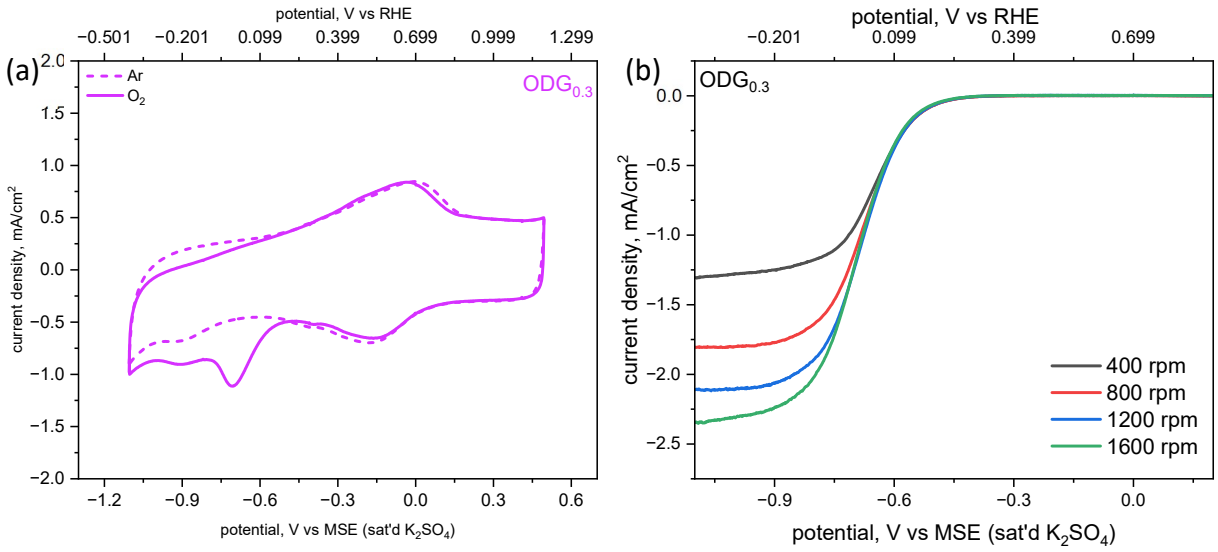

Figure B 2: (a) CV in Ar (dash line) and O_2 (solid line) (b) LSV at 400 rpm, 800 rpm, 1200 rpm, 1600 rpm for $ODG_{0.3}$

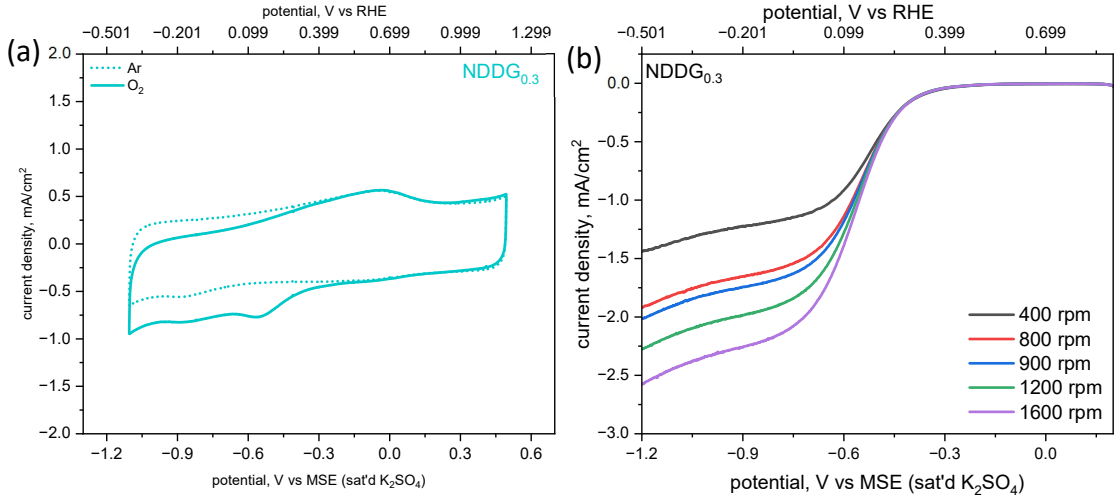

Figure B 3: (a) CV in Ar (dash line) and O_2 (solid line) (b) LSV at 400 rpm, 800 rpm, 1200 rpm, 1600 rpm for $ODG_{0.3}$